



Universitat Autònoma de Barcelona

Facultat de Ciències

**Nanocalorimetric studies of
size effects in magnetic oxides and
formation kinetics in silicides**

Doctoral Thesis submitted by

Manel Molina Ruiz

to apply for the degree of Doctor in Materials Science

Supervised by

Dr. Aitor Lopeandía Fernández

Nanomaterials and Microsystems Group

Physics Department

Bellaterra, September 2014

El Dr. Aitor Lopeandía Fernández, professor agregat interí del Departament de Física, a la Facultat de Ciències de la Universitat Autònoma de Barcelona,

CERTIFICA que en Manel Molina Ruiz, Llicenciat en Física i Enginyer de Materials per la Universitat Autònoma de Barcelona, i en posició del Màster Oficial en Ciència i Tecnologia de Materials, ha realitzat sota la seva direcció el treball que porta com a títol *Nanocalorimetric studies of size effects in magnetic oxides and formation kinetics in silicides*, el qual es recull en aquesta memòria per tal d'optar al Títol de Doctor en Ciència de Materials per la Universitat Autònoma de Barcelona.

Manel Molina Ruiz
Bellaterra, Setembre 2014

Dr. Aitor Lopeandía Fernández
Bellaterra, Setembre 2014

Nanocalorimetric studies of size effects in magnetic oxides and formation kinetics in silicides

Doctoral Thesis submitted by **Manel Molina Ruiz** to apply for
the degree of Doctor in Materials Science, with International Doctorate Mention

Supervised by

Dr. Aitor Lopeandía Fernández

Thesis committee

Dr. Josep Fontcuberta Griñó Materials Science Institut of Barcelona, CSIC	President
Dr. Lluís Mañosa Carrera University of Barcelona	Member
Dr. Jean-Luc Garden Institut Néel, CNRS	Member

International Doctorate Mention committee

Dr. Leslie H. Allen University of Illinois at Urbana-Champaign	External Assessor
Dr. Andreas Rydh Stockholm University	External Assessor

For it matters not how small the beginning may seem to be,
what is once done well is done forever.

Henry David Thoreau

Contents

Agraiments	xiii
Summary	xvii
1 Introduction	19
Overview of this Thesis	21
References	22
2 Experimental setup	25
2.1 The nanocalorimeter	25
2.1.1 Microfabrication	26
2.1.2 Nanocalorimeter calibration	30
2.2 Experimental setups	32
2.2.1 <i>In-situ</i> setup	32
2.2.2 Immersion cryostat setup	36
2.2.3 Specific XRD setup	40
2.3 Conclusions	42
References	42
3 Nanocalorimetry: optimizing the old, developing the new	45
3.1 Calorimetry and thermodynamics	45
3.2 Principle of operation	47
3.2.1 Quasi-adiabatic nanocalorimetry	49
3.2.2 Microsecond-pulsed heating nanocalorimetry	56
3.2.3 Power compensated nanocalorimetry	66
3.3 Heat capacity derivation	68
3.4 Conclusions	72

References	72
4 Antiferromagnetic interaction in CoO	75
4.1 Introduction	76
4.1.1 The cobalt oxide system	80
4.2 Experimental	82
4.2.1 Nanocalorimetric approach	84
4.3 Microstructural study	85
4.3.1 Thickness influence	87
4.3.2 Influence of growth temperature	92
4.4 Antiferromagnetic interaction	94
4.4.1 Thickness dependence	94
4.4.2 Dependence on growth temperature	97
4.4.3 Microstructure dependence	102
4.5 Conclusions	103
References	104
5 Silicide formation of Pd₂Si	109
5.1 Introduction	110
5.2 Experimental	112
5.2.1 Calorimetric approach	113
5.3 Pd ₂ Si formation on Si (1 0 0)	113
5.3.1 Preparation of Pd/c-Si samples	113
5.3.2 Results and Discussion	114
5.3.3 KJMAE kinetic model	118
5.4 Pd ₂ Si formation on amorphous Si	121
5.4.1 Preparation of Pd/a-Si samples	121
5.4.2 Results and Discussion	122
5.4.3 Calorimetric and structural analysis	126
5.4.4 KJMAE kinetic model	129
5.4.5 Simultaneous characterization by synchrotron radiation	133
5.5 Conclusions	138
References	138
6 General conclusions	145

CONTENTS

List of publications	147
Glossary	149

Agraïments

Vull agrair a totes les persones que m'heu ajudat, ensenyat i acompanyat durant tots aquests anys, estic orgullós de poder culminar tota la feina que hem fet amb la finalització d'aquest treball, la meva Tesi Doctoral.

En especial als companys del meu Grup de Recerca, el Grup de Nanomaterials i Microsistemes (GNaM) de la Universitat Autònoma de Barcelona, amb els que he conviscut i dels que he après moltes coses. A tots vosaltres i per tot el que m'heu aportat, els que ja heu marxat, Prof. Dra. Maria Teresa Mora, perquè sempre que em quedava sense respostes em sabies fer la pregunta adient, Dr. Joan Torrens, vaig poder aprendre a contagiar-me de la teva tranquil·litat, Dr. Roger Doménech, Dr. Edgar León, Dr. Alfonso Sepúlveda, estando a tu lado todo parecía más fácil, salvo ganarte jugando a squash, Dra. Iris Moder, siempre tenías un momento para ayudar a un compañero, i Antonio Pablo Pérez, lo bueno y breve, dos veces bueno. I els que encara hi sou, Dra. Gemma Garcia, per la capacitat que tens de ser una bona mestra, ahora que una fantàstica col·lega, Dra. Marta González, l'alegria i la teva simpatia fan els dies mes curts, Cristian Rodríguez, las cosas cambian, o no, pero las personas buenas no, o al menos la bolsa siempre subirá, Pablo Ferrando, és genial tenir-te com a company, la feina és més senzilla i el que no és feina és millor, i Joan Ràfols, no hem treballat ni hem passat gaire temps junts, però m'agradaria poder-ho fer algun dia, això sí, els divendres no ens els treu ningú. En particular a dos personas del Grupo, cuyas decisiones marcaron el futuro de un joven estudiante que estaba a punto de acabar la Licenciatura de Física. Gracias Prof. Dr. Javier Rodríguez, por confiar en mí y darme esta gran oportunidad, por tu gran dedicación y atención. Y gracias Dr. Aitor Lopeandía, por enseñarme a aprender juntos, por aceptar ser mi Director de Tesis, por recibirme como alumno años atras, y hoy, saludarme como amigo. Gracias a los dos por abrirme las puertas de un mundo fascinante.

Un agraïment especial mereix el Dr. Francesc Pi, per les hores que hem compartit al Laboratori de Capes Primes i per l'ús que ens has permès fer de l'equip d'evaporació. Per ser mestre i company.

Je tiens à remercier le Dr. Olivier Bourgeois de l'Institut Néel à Grenoble, pour l'hospitalité et le soutien reçu pendant mon séjour de 6 mois au sein de son Groupe - Thermodynamique des Petits Systèmes. Ce séjour m'a permis, entre autre, de me plonger dans le monde de la cryogénie et de la supraconductivité. Les nombreuses et stimulantes discussions sur le magnétisme en général et la nanocalorimétrie en particulier, ont été d'une utilité extraordinaire pour l'évolution de mon travail et ma formation comme chercheur. Mes remerciements vont également au Prof. Dominique Givord du Groupe Micro et Nanomagnétisme de l'Institut Néel pour tous ses conseils et les discussions scientifiques. Je remercie le reste des membres de l'Institut Néel avec qui j'ai eu le plaisir de travailler et de connaître pendant mon séjour pour leur chaleureux accueil et leur aide: Jean-Luc Garden, Pierre Brosse-Marron, Anne Gérardin, Gérard Barthelemy, Emmanuel André. . . et tous les membres de la plateforme Nanofab.

I am very grateful Theo Bijvoets from Rivac Technology, and Mildred van der Swaan of course, because from the first moment you helped me and taught me selflessly throughout all these years. Your great expertise in vacuum technology and cryogenics have been essential for this work. I cannot imagine this ending without your distant, but also close, company.

Al Dr. Francesc Xavier Muñoz, a la Dra. Llibertat Abad i al seu equip d'investigació de l'Institut de Microelectrònica de Barcelona (IMB-CNM), per la col·laboració en els processos tecnològics de microfabricació dels nanocalorímetres. Al Dr. José Santiso i a en Pablo García de l'Institut Català de Nanociència i Nanotecnologia (ICN2), per la gran quantitat de mesures que vam fer i el suport tècnic i científic que em van oferir. A en Bernat Bozzo del Laboratori de Baixes Temperatures i Magnetometria, i a l'Anna Crespi del Laboratori de Difracció de Raigs X, ambdós de l'Institut de Ciència de Materials de Barcelona (ICMAB), per la dedicació i l'afany d'obtenir mesures de qualitat. Al Dr. Josep Nogués de l'Institut Català de Nanociència i Nanotecnologia (ICN2), per les fructuoses xerrades sobre sistemes magnètics. Al Dr. Xavier Martí, de la Universitat de Califòrnia, Berkeley, per confiar en les possibilitats que ofereix la nostra tècnica i pels bons resultats que hem obtingut. A la Dra. Inma Peral del ALBA Synchrotron Light Facility, per involucrar-te con nuestra investigación y hacerla tuya, permitiéndonos adaptar perfectamente nuestro equipo a la línea.

I thank to the Dr. János L. Lábár from the Research Institute for Technical Physics and Materials Science of the Hungarian Academy of Sciences, for our fruitful collaboration during the study of the CoO thin films microstructure.

Per altra banda, també vull agrair als companys dels serveis científics i tècnics de Microscòpia Electrònica (SME), Difracció de Raigs X, Laboratori d'Ambient Controlat i del Departament de Física de la Universitat Autònoma de Barcelona per l'ajuda desinteressada que he rebut en la preparació de mostres i

AGRAÏMENTS

posterior anàlisi i en la solució de qualsevol problema amb el que em pogués trobar... Emma Rossinyol, Francisca Cardoso, Marcos Rosado, Pablo Castro, Javier Martínez, Maria Angeles Benítez, Raquel Palencia, Manel Garcia, Jordi Santos, Rafael Moraira i Ramón Violeta, gràcies a tots vosaltres.

Per acabar, a les persones que sou més lluny d'aquest petit món meu, però a tocar de la resta. Pares, sempre heu estat al meu costat, us heu esforçat per tal de que ho tingués tot i pogués arribar a on jo volgués, sense vosaltres no ho hagués aconseguit. Amics, no em puc imaginar aquest camí sense vosaltres, Espi, Sílvia, Meri, Lucho, Brass, Núria, Jose. . . tots. En especial Dra. Aïda Varea, per l'amistat, la companyia i l'ajuda que m'has ofert durant tots aquests anys, per tots els moments que hem viscut des que vam començar la Llicenciatura de Física.

I a tu Ana, ets la persona més important, per la paciència que has tingut, per acompanyar-me durant tot aquest temps, per les coses bones i les dolentes que hem viscut, per tot el temps que m'has concedit per a què ho pogués dur a bon terme.

A tots els que d'una manera o d'una altra hi heu participat,

gràcies !

Summary

The advances in Nanoscience and Nanotechnology have been paved, not only by the discovery of new technologies, but also by the continuous improvement of the existing ones, adapted to ultra-small samples. In that framework, calorimetry is a technique suitable to measure thermodynamic properties and energetic processes, such as phase transitions, through the heat absorbed or released by the system. Taking profit of advances in microfabrication techniques a new family of nanocalorimeters, based on ultra-light calorimetric cells and built up onto thin film dielectric membranes, has emerged demonstrating enhanced sensitivities compared with traditional calorimeters, reaching resolution levels better than $1 \text{ nJ K}^{-1} \text{ mm}^{-2}$.

The present research work presents the development and optimization of the nanocalorimetry. We expand the dynamic ranges of applicability from ultrafast heating rates to quasi-static ones. Furthermore, we demonstrate its applicability to the study of different phase transitions at the nanoscale.

In the first Chapter, a general introduction sets out the necessity of developing new thermal characterization techniques, to give service to the scientific community working in the fields of Nanoscience and Nanotechnology, and also provides an historical overview about the development and the miniaturization of calorimeters. Subsequently, Chapter 2 provides an overview about nanocalorimeters microfabrication processes, and about design and fabrication of specific experimental setups to carry on nanocalorimetric experiments from 80 to 1200 K in adiabatic conditions.

Chapter 3 presents the nanocalorimetric tools used during this work and the improvements that we have implemented. The two major advances achieved are:

- (i) The expansion of the operating heating rates, where the combination of pulsed and power compensated methods have permitted to cover heating ranges from 0.1 to 10^6 K/s. Moreover, a thorough study of the heat capacity calculation, and the analysis of signal noise led us to obtain a methodol-

ogy that improves qualitatively the results obtained from data processing.

- (ii) The development of a new quasi-static technique that combines huge signal enhancement of DC calorimetry, and averaging capabilities of AC calorimetry. This new technique has been named microsecond-pulsed heating nanocalorimetry, and it allows measuring second-order phase transitions with very high sensitivity (below $75 \text{ pJ K}^{-1} \text{ mm}^{-2} \text{ Hz}^{-1/2}$), with improved thermal maps in the sensing area (less than 1 K thermal gradient) than using pulsed methods.

Besides, nanocalorimetry developed here has been used to deeply study the effect of dimensionality in two different physical systems: the magnetic order-disorder transition in thin films of CoO, and the formation kinetics of thin films of Pd₂Si from Pd/Si bilayers.

In Chapter 4 we present how microstructure influences the antiferromagnetic interaction in CoO thin films. We study size effects in thin films from 1 to 20 nm thick, and the influence of grains and boundaries sizes from a thermodynamic perspective in 20 nm samples. We relate thermodynamic properties to magnetic ones by means of nanocalorimetric (by quasi-adiabatic nanocalorimetry), structural (by X-ray diffraction and transmission electron microscopy), and magnetic (by superconductor quantum interferometer device magnetometry) characterization.

In Chapter 5 the formation kinetics of Pd₂Si is analyzed over a wide range of heating rates spanning six orders of magnitude. To achieve this purpose, we combine conventional differential scanning calorimetry, saw-tooth nanocalorimetry and quasi-adiabatic nanocalorimetry. This study is complemented by the structural characterization of the samples using X-ray diffraction, micro-X-ray diffraction, and electron microscopy. We also use a kinetic model to obtain the most relevant kinetic parameters by fitting the calorimetric curves.

1. Introduction

The recognition that size has dramatic consequences on the physicochemical properties of nanomaterials has opened a new framework in the field of Materials Science. Most of these changes are essentially motivated by two reasons: the larger impact of surface atoms and the presence of quantum confinement effects at such small distances.

In a solid, the atoms at the surface have very different behavior than those inside the material: exhibiting a larger chemical reactivity and quite different inner energies, depending on the number of neighbors and type of bonds. In nanoscale, new crystalline phases (not existing in bulk) can be stabilized by the importance of surface energies and restructuring. Surface related phenomena becomes dominant only for materials with a large ratio surface to volume atoms (like nanoparticles, nanowires, thin films or porous materials) when the number of surface atoms (for spherical particles proportional to radius squared) becomes relevant compared to the number of volume atoms (for spherical particles proportional to radius cubic). Thus, in the scaling down process of matter, some physical properties are expected to change with size, and one of the first examples experimentally observed was the smooth size-dependence of the melting point of small particles of pore-confined matter, in 1871 by William Thomson (Lord Kelvin). Indeed, ancient civilizations had, without being conscious of it, already used size effects in cosmetics [1] or in decoration [2], such as paint, glass and pottery. The other reason is a quantum-size effect related with the wave-like behavior of electrons inside the matter. All physical phenomena where electron are involved, from energy and charge transport to optical interactions, exhibits a dependence when material size is reduced below the Fermi wavelength.

During 20th century, several milestones in research have promoted the strengthening of Nanoscience and consequently the development of the new field of Nanotechnology. Among them we would like to highlight the visionary lecture given by the theoretical physicist Richard Feynman entitled *There is plenty of room at the bottom – an invitation to enter a new field of physics*, which he addressed the American Physical Society in its annual meeting on 29th December 1959. He envisaged that the ability

to individually treat the matter (atom by atom) would let to enormous advances in technology, enabling the creation of smaller machines and multiplying orders of magnitude the storage information density. Unfortunately, the real revolution happened later than expected with the development of the scanning tunneling microscope in 1982 by Binnig and Rohrer [3], and somewhat later, in 1986 with the atomic force microscope [4]. These instruments permitted for the first time the observation and manipulation of single atoms. The multidisciplinary aspects of Nanoscience include diverse fields like condensed-matter physics, solid-state chemistry, materials science, electrical engineering, biology, and other disciplines. Nanoscience closes the gap between individual atoms and bulk materials.

In parallel to this revolution, existing characterization techniques have also being constantly improved to attain the specificities of nanomaterials. This is the case of calorimetry, a technique that measuring the heat released or absorbed by a sample during a thermal process, allows access to the thermodynamics and kinetics information of materials, like heat capacity, entropy changes, critical temperatures and enthalpies. The first calorimeter was developed and used by Antoine Lavoisier and Pierre-Simon Laplace, during the winter of 1782-83, to determine the heat evolved in various chemical changes. The calorimetric techniques suffered a great breakthrough with the arrival of electronics to research laboratories. Hence, Orso Mario Corbino developed the modulation calorimetry [5, 6], and few years later Archie Garfield Worthing did the same with the pulsed calorimetry [7]. From this moment, thermodynamic properties awakened a great interest as a mean of obtaining information about the lattice and electronic properties of matter. In 1963 Morin and Maita [8] developed a pulsed calorimeter for samples mass as small as 100 mg. With the development of lock-in-amplifier techniques the modulation calorimetry became attractive, and in 1968 the steady-state AC-temperature calorimetry of Sullivan and Seidel [9] was presented. In 1972 Bachmann et al. [10] reported a calorimeter that used a relaxation method to measure bulk samples as small as 1 mg. This was the starting point for the development of different techniques towards higher sensitivity and, as a consequence, nanosized samples. A constant in the design efforts towards enhancing sensitivities of calorimeters was the miniaturization of the calorimetric cells. Typically, the resolution of electronics limited the sensitivity to several orders of magnitude below the heat capacity addenda. With microfabrication techniques development arrived from Si technological industries at the beginning of the nineties, several groups started to build up calorimeters based on ultra-light dielectric membranes, effectively reducing the addenda of the calorimetric cell. In 1994, that Frances Hellman's Group at UC Berkley published the first silicon nitride membrane-based calorimeter, and using relaxation method calorimetry they determined the heat capacity of multilayer thin films, with masses as small as few micrograms [11, 12]. It was a real breakthrough (three orders of magnitude) compared to commercial devices available at that time. Nevertheless, the sensitivity level of this technique did not allow the direct measurement of singles thin films but on multilayered stacks, implying that

1. INTRODUCTION

physical properties might be altered by surface or confinement effects. A further improvement was done in 1995, when the Group of Leslie Allen at the University of Illinois at Urbana-Campaign, developing the fast scanning thin film calorimetric technique [13], that reached mass resolutions down to 1 ng [14]. The huge heating rates reached in this method, above 10^4 K/s, are the cause for the large improvement in sensitivity, which allows the direct measurement of heat capacity and phase transitions even in single thin films. In this method, the dynamic range of the scan prevents to measure the dependence of heat capacity, in quasi-isothermal conditions, respect to external variables (magnetic field, time, pressure. . .). Two years later, the Group of Jacques Chaussy at the Institut Néel of the CNRS in Grenoble, published their first work on membrane-based AC-nanocalorimetry measuring the superconducting transition of lead at different magnetic field values [15]. The major drawback of the AC techniques is the difficulty of determining accurately the real heat capacity during first order phase transitions, i.e. any process which involves a latent heat.

In 2001, the Group of Nanomaterials and Microsystems (GNaM) at the Universitat Autònoma de Barcelona started to develop their own nanocalorimetric technique, based on pulsed calorimetry, and in 2002 they obtained the first results on the melting of CdSe quantum dots [16]. Three years later, the group developed the power compensated nanocalorimetry and the first results on the melting of indium thin films were published [17]. In 2008, the technique was refined by the use of FPGA integrated circuits [18]. Nowadays membrane-based calorimetry is one of the main tools in GNaM research and the Group is widely recognized by its nanocalorimetric activities. The first part of this Thesis is framed in the continuous improvement of nanocalorimetric techniques, besides the development of a new proposed nanocalorimetric technique. The second part focuses on the application of these techniques to study the properties of matter at the nanoscale. Nanocalorimetry is complemented with other characterization techniques to allow discussion of thermal properties as a function of microstructure, as well as, to complement discussions with magnetic properties, when necessary.

Overview of this Thesis

This Thesis is divided into four main chapters, general conclusions and future perspectives as follows:

Chapter 2 We explain the design, fabrication and use of various specific experimental components, developed during this PhD Thesis, which habilitate the implementation of nanocalorimetric techniques.

Chapter 3 In this Chapter we present the nanocalorimetric techniques used during this work to obtain results reported later. We also introduce the development, operation and implementation of a new nanocalorimetric technique, the microsecond-pulsed heating nanocalorimetry (μ -PHnC). Finally, we study the heat capacity derivation from experimental data, and we reformulate the heat capacity analysis.

Chapter 4 An introduction about magnetism and antiferromagnetic oxides is done with the aim to clarify subsequent findings. Then, the results on the study of the magnetic interaction in CoO samples are presented and discussed. We deeply characterize the samples microstructure and we try to establish how it affects the antiferromagnetic interaction.

Chapter 5 The silicide formation of Pd₂Si system is discussed through the study of the ultrathin films microstructure and calorimetric signal. The results are complemented by a kinetic modelling of the calorimetric curves, reporting the most relevant kinetic parameters of the Pd₂Si formation.

Chapter 6 The main conclusions of this work are presented clearly and concisely.

References

- [1] P. Walter, E. Welcomme, P. Hallégot, N. J. Zaluzec, C. Deeb, J. Castaing, P. Veyssi re, R. Br niaux, J-L L v que, and G. Tsoucaris. Early use of PbS nanotechnology for an ancient hair dyeing formula. *Nano letters*, 6(10):2215–9, October 2006.
- [2] M. Jose-Yacaman, L. Rendon, J. Arenas, and M. C. Serra Puche. Maya Blue Paint: An Ancient Nanostructured Material. *Science*, 273(5272):223–225, July 1996.
- [3] G. Binnig and H. Rohrer. Scanning tunneling microscopy. *Helvetica Physica Acta*, 55:726–735, 1982.
- [4] G. Binnig, C. F. Quate, and Ch. Gerber. Atomic Force Microscope. *Physical Review Letters*, 56(9):930–933, 1986.
- [5] O. M. Corbino. Temperaturschwankungen in Lampen von d nnen Fasern mit einem Wechselstrom durchflossen und die resultierende Wirkung auf den Gleichrichter als Ergebnis der Anwesenheit von geradzahligen Harmonischen. *Physikalische Zeitschrift*, 11:413–417, 1910.

References

- [6] O. M. Corbino. Periodische Widerstandsänderungen feiner Metallfäden, die durch Wechselströme zum Glühen gebracht werden, sowie Ableitung ihrer thermischen Eigenschaften bei hoher Temperatur. *Physikalische Zeitschrift*, 12:292–295, 1911.
- [7] A. G. Worthing. Atomic heats of tungsten and of carbon at incandescent temperatures. *Physical Review*, 12(3):199–225, 1918.
- [8] F. J. Morin and J. P. Maita. Specific Heats of Transition Metal Superconductors. *Physical Review*, 129(3):1115–1120, 1963.
- [9] P. F. Sullivan and G. Seidel. Steady-State, ac-Temperature Calorimetry. *Physical*, 173(3):679–685, 1968.
- [10] R. Bachmann. Heat Capacity Measurements on Small Samples at Low Temperatures. *Review of Scientific Instruments*, 43(2):205, 1972.
- [11] D. W. Denlinger, E. N. Abarra, K. Allen, P. W. Rooney, M. T. Messer, S. K. Watson, and F. Hellman. Thin film microcalorimeter for heat capacity measurements. *Review of Scientific Instruments*, 65(4):946–959, 1994.
- [12] E. N. Abarra, K. Takano, F. Hellman, and A. E. Berkowitz. Thermodynamic measurements of magnetic ordering in antiferromagnetic superlattices. *Physical Review Letters*, 77(16):3451–3454, October 1996.
- [13] S. L. Lai, G. Ramanath, and L. H. Allen. High speed (10^4 °C/s) scanning microcalorimetry with monolayer sensitivity (J/m^2). *Applied Physics Letters*, 67(9):1229–1231, 1995.
- [14] S. L. Lai, G. Ramanath, L. H. Allen, and P. Infante. Heat capacity measurements of Sn nanostructures using a thin-film differential scanning calorimeter with 0.2 nJ sensitivity. *Applied Physics Letters*, 70(January):43–45, 1997.
- [15] F. Fominaya, T. Fournier, P. Gandit, and J. Chaussy. Nanocalorimeter for high resolution measurements of low temperature heat capacities of thin films and single crystals. *Review of Scientific Instruments*, 68(11):4191, 1997.
- [16] J. Rodriguez-Viejo, M. Chacon, A. F. Lopeandia, M. T. Clavaguera-Mora, L. R. Arana, and K. F. Jensen. Microreactors for Thin-Film Calorimetry. *MRS Proceedings*, 741:J2.4, February 2002.

- [17] A. F. Lopeandia, L. L. Cerdo, M. T. Clavaguera-Mora, L. R. Arana, K. F. Jensen, F. J. Munoz, and J. Rodriguez-Viejo. Sensitive power compensated scanning calorimeter for analysis of phase transformations in small samples. *Review of Scientific Instruments*, 76(6):065104, 2005.
- [18] A. F. Lopeandia, J. Valenzuela, and J. Rodríguez-Viejo. Power compensated thin film calorimetry at fast heating rates. *Sensors and Actuators A*, 143(2):256–264, 2008.

2. Experimental setup

In this Chapter, we describe from the technical point of view, the experimental setups specially developed that, combined with different nanocalorimetric techniques (presented in Chapter 3), allow to carry out the studies presented in this Thesis. We start describing the details concerning the nanocalorimeters: the design and fabrication of the membrane-based devices, the self-aligning shadow masks for sample deposition, and the required temperature calibration procedures (Section 2.1 *The nanocalorimeter*). Most of the calorimetric techniques employed or developed during the Thesis require vacuum environments. To fulfill the especial requirements of each experiment, we have built-up or readapted several vacuum chambers and cryostats: (i) an special setup of moving shutters mounted inside an e-beam evaporator to perform *in-situ* measurements at low temperature (Subsection 2.2.1 *In-situ setup*), (ii) a vacuum chamber to be immersed into a liquid helium cryostat, equipped with a superconducting coil to generate magnetic fields, and a thermostatic probe to perform nanocalorimetric experiments from 4 to 400 K (Subsection 2.2.2 *Immersion cryostat setup*), and (iii) a setup to perform nanocalorimetry and simultaneously characterize the thin film sample by XRD in a synchrotron facility (Subsection 2.2.3 *Specific XRD setup*).

2.1 The nanocalorimeter

The design of the nanocalorimeters was previously carried out by GNaM [1]. As explained in the introduction, the evolution of calorimetric device towards an enhanced mass or energy resolutions has been marked by the heat capacity addenda reduction of the calorimetric cells [2–4]. In that sense, our Group decided to design and microfabricate an ultralight calorimeter based on thin film dielectric membranes. The membrane served as mechanical substrate both to define in one of the sides the actuators and transducers, required for a calorimetric experiment, and in the other side the sample under study. In general, any calorimetric cell requires both a heat source or heat drain (depending on the operational method) and

the presence of a thermometer to follow up the temperature evolution. Using a single metallic thin film element as heater and thermometer, the heat capacity addenda per unit area could be reduced down to $500 \text{ nJ K}^{-1} \text{ mm}^{-2}$ at room temperature. The planar geometry guarantees an excellent vertical heat diffusion and thus vertical temperature homogeneity between metallic actuator and sample, even for faster heating dynamics (up to 10^6 K/s). Motivated by the reduced thickness of the membrane, the lateral heat diffusion is limited providing a very effective thermal isolation between the sensing part of the calorimetric cell and the surroundings, especially when working in high vacuum conditions. Also, due to the reduced lateral diffusion, it is the difficulty to obtain a flat temperature map in the sensing area during the experiments, which is the major drawback of this type of devices. To counteract that difficulty, a special effort was devoted during the design process of the metallic element. The final meander shape design has been found as the best to obtain an optimal behavior both in stationary and when applying fast heating ramps.

2.1.1 Microfabrication

The nanocalorimeters used during this work were fabricated in the clean rooms at IMB-CNM and LAC-UAB, and in the Thin Films Laboratory-UAB by using standard microfabrication technologies [5], schematically shown in Figure 2.1. The fabrication process starts with a double-sided polished p-silicon wafer (4 inches diameter, $520 \text{ }\mu\text{m}$ thick, $40 \text{ }\Omega\text{cm}$ resistivity). The wafer is thermally oxidized at 1273 K to grow a 50 nm thick silicon oxide film [Figure 2.1(a)]. This electrical insulating layer is introduced to avoid electrical shunting problems that may appear in this type of devices at high temperatures [6]. As a second step, a 180 nm thick low-stress Si_3N_4 is grown by low pressure chemical vapor deposition [Figure 2.1(b)]. The nitride deposition on the front side of the wafer will eventually form the free-standing membrane of the final nanocalorimeter. Using standard photolithography combined with a SF_6 reactive ion etching, squared windows are opened in the backside Si_3N_4 exposing the underlying silicon [Figure 2.1(c)]. The windows will define the area where silicon is removed during the final bulk etching, using the Si_3N_4 as stopping mask. In the front side, the metallic elements with meander shape are defined by photolithography and subsequent lift-off process of the evaporated metal [Figure 2.1(d)]. The window alignment with the bottom Si_3N_4 is achieved using infrared light and guarantees the correct position of the metallic elements in the resulting membrane, after the bulk etching.

The composition and thicknesses of the evaporated metal depends on the final application. To be used as heater and sensor, the chosen metal must exhibit a monotonic behavior in all its physical properties along the full range of measure, without the presence of any phase transition, and a reduced reactivity to

2. EXPERIMENTAL SETUP

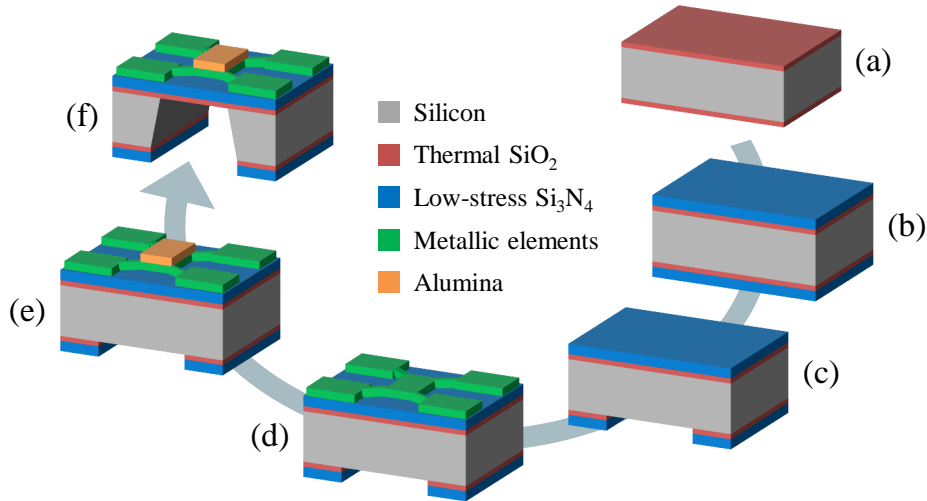


FIG. 2.1 Microfabrication process schematics.

enhance its stability over time. Precious metals are good candidates. Among them, platinum exhibits the large temperature range with almost linear physical properties dependence, and it results a good choice to measure the temperature through its resistance [7, 8]. Although ideally the thinner the layer of metal, the smaller would be the heat capacity addenda, it should be noted that metal morphology influences negatively the resistivity and therefore the final sensitivity. Typically, the thickness of the evaporated metal layer determines its microstructure obtaining smaller average grain sizes for smaller thicknesses. The smaller is the average grain size in the metal layer, the larger is the grain boundaries contribution to the residual resistivity and therefore the smaller the temperature coefficient of resistance (TCR). A cost-efficient agreement should also account for the temperature stability: the thicker the metal layer, the better the temperature stability and the lower the electrical impedance of the final device. Platinum layers with thicknesses from 40 to 100 nm were measured obtaining TCR values from 0.0007 to 0.0027 K⁻¹, and a maximum temperature of operation around 1200 K. To improve the adhesion of platinum we routinely grow previously a thin layer of titanium or chromium with thicknesses around 1/10 of the nominal thickness of platinum used. Additionally, nanocalorimeters fabricated for high temperature applications (above 800 K), are submitted to a second photolithographic process in the front side of the heater/sensor element, capping it with a 150 nm thick layer of aluminum (III) oxide (Al₂O₃), also called alumina, which is deposited also by e-beam evaporation [Figure 2.1(e)]. The next step consists on annealing the wafer in a furnace for several hours at high temperatures (from 925 to 975 K), in order to thermally stabilize the metallic elements. The annealing temperature depends on the metallic heater; being smaller for thinner layers of Pt. Using a special wax and a Teflon custom-built chamber to protect the metallic elements in the front side, the wafer is dipped in the KOH solution (30% by weight in water at 353 K). The KOH etches Si anisotropically from the Si₃N₄ opened window in the backside. The etching rate along the [1 1 1] planes is slower and, thus, the dug out cavity has a trapezoidal cross section

finishing the attack on the SiO_2 layer [Figure 2.1(f)]. SiO_2 , with a much lower etching rate is used as stopping layer. To increase the survival rate of the membranes the wafer is controlled and removed from the etching bath when still remains a 5 to 10 μm Si layer below the membrane. Afterwards, the wafer is diced to obtain every individual nanocalorimeter. The protective wax is maintained during the dicing process to improve its mechanical resistance and to prevent the adhesion of pollution of the free-standing membrane. Treating the nanocalorimeters individually, the Si layer below the membrane is removed in a later process applying the same KOH solution but at room temperature. The evolution of the final attack is shown in the series of images of Figure 2.2, where every image was taken every 2 hours. Once the membrane is completely free of Si rests, the protective wax is removed. The cleaning procedure includes a sequential dip of the calorimeters into acetone, ethanol, isopropyl alcohol and deionized water. Finally, the nanocalorimeters are dried with a nitrogen flow at low angles to avoid the breaking of the membrane and are ready for their calibration and experiments.

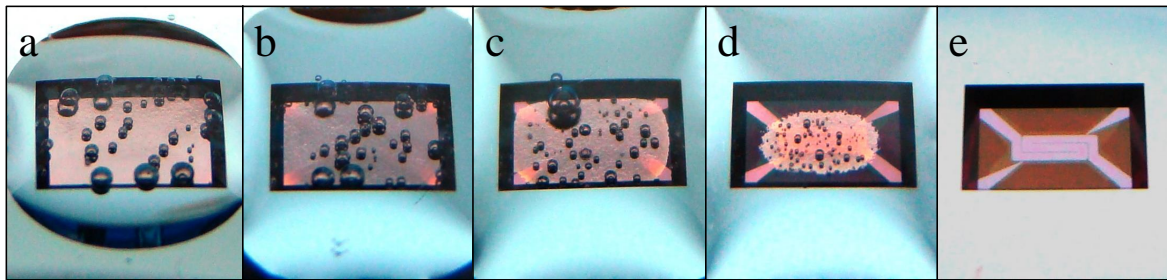


FIG. 2.2 Series of images reporting the final Si etch onto the membrane.

Figure 2.3 shows the schematic layout of the nanocalorimeter with a free standing membrane of 12 mm^2 , with the meander type design for the metallic element at the center. The meander is connected via 4 probes, to measure locally temperature and power released at the center of the meander. The two wide strips are used to inject the current and the two thinner connections are used to locally probe the voltage dropped. This central part of the meander of 1.085 mm^2 , also called sensing part or calorimetric cell (CC), is the area of the device where sample should be placed and is expected to have a flat temperature map during the heating ramps.

To preserve temperature maps and properly sense a sample it should be selectively deposited beneath the sensing area of the calorimeter. For that reason, a shadow mask was microfabricated in silicon. As it is shown in Figure 2.4, the design uses the wall defined by Si plane (1 1 1) in both nanocalorimeter window and mask to self-align one to each other. Misalignments smaller than 50 μm are routinely achieved. Shadow masks are perfect to delimit the area for samples evaporated by physical methods. Nevertheless, this type of nanocalorimeters also permits deposit samples by other methods like spin coating or using micromanipulators.

2. EXPERIMENTAL SETUP

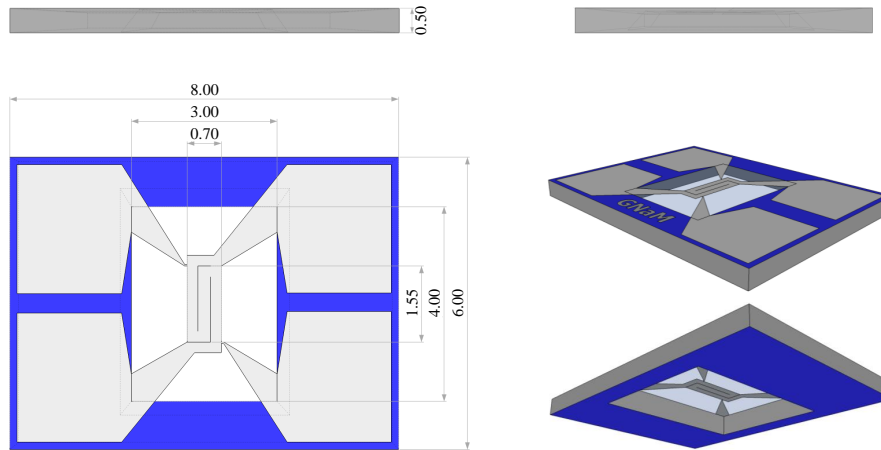


FIG. 2.3 Scheme showing the top, front and right views of the nanocalorimeter, and its 3D representation viewed from top and bottom. Units are in millimeters.

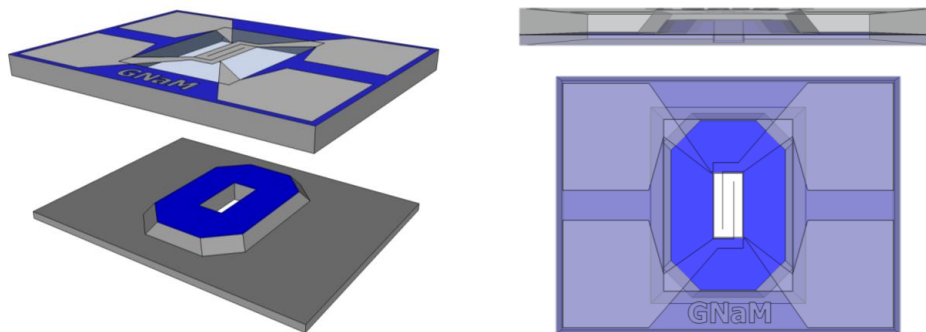


FIG. 2.4 (Left) 3D schematic of a shadow mask together with a nanocalorimeter. (Right) In-plane and cross sectional views showing how the shadow mask fits within the nanocalorimeter.

In most of the experiments, a twin couple of calorimeters are used simultaneously to work in differential configuration, one loaded with sample and the other to subtract the background contribution. This configuration permits to obtain enhanced sensitivity. In some cases, it is required to deposit a material (like a buffer layer) also in the reference calorimetric cell. Using a single vapor source, it is necessary to place spatially close both nanocalorimeters to preserve the functionality of the shadow masks and the amount of material deposited. For that reason, a double membrane nanocalorimeter was also designed, see Figure 2.5. With identical layout design for the CCs, this design also permits to reduce the common background noise (due to common temperature fluctuations of the Si frame). Besides, the spatial proximity in the wafer also guarantees the similarity of the two metallic elements in terms of impedance (essentially determined by thickness and shape), and the similarity in heat capacity addenda of both cells since membrane finishing attack should be very similar. These devices have been used to measure phase transitions [9–11] in a wide range of heating rates [12, 13].

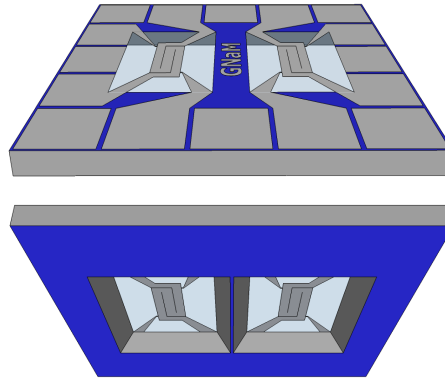


FIG. 2.5 3D schematic of a double nanocalorimeter showing its components side (top) and its windows side (bottom).

2.1.2 Nanocalorimeter calibration

The platinum thin film meander acts both as heater and thermometer, for this reason it is crucial to determine with accuracy its resistance versus temperature $R(T)$ dependence. In general for any metal, at very low temperatures the resistivity presents a residual value at zero Kelvin. At such temperature the non-null resistivity is motivated by the scattering of electron flowing through the metallic net with the impurities and with net imperfection (like grain boundaries). Increasing temperature, the interactions with phonons (crystalline net vibration) start playing a dominant role and the resistivity starts growing monotonically. For platinum thin films used in this work, the initial plateau finishes around 30 K, and high order polynomials are required to adjust the dependence with temperature. Below 30 K the TCR is too low and the resistivity cannot be used to measure temperature. Between 30 and 100 K, we use a 4th order polynomial, while above 100 K the resistivity can be easily adjusted by a 2nd order polynomial up to room temperature; where with a simple linear dependence suffices to describe the resistivity behavior. It is at high temperatures, above 500 K, that considering a 2nd order polynomial is again required. Therefore, depending on the temperature range of the experiment, the strategy is to locally calibrate the $R(T)$ dependence. We distinguish two different procedures to calibrate the $R(T)$ of the devices: the steady-state and the dynamic methods.

With the steady-state method, the device resistance is measured in isothermal conditions loading the devices in the thermostatic probe of a cryostat, where the temperature of the complete device can be fixed from 30 to 400K. Performing current/voltage curves, the resistance value can be extrapolated for zero current (without self-heating) for each temperature. The $R(T)$ curve is obtained by measuring at several temperatures. In this method the complete device should be heated up, and unfortunately the stress induced in the membrane, when the Si frame expands, promotes the crash of the membrane when

2. EXPERIMENTAL SETUP

TABLE 2.1 Typical calibration materials, indicating their critical temperatures, the occurring phenomena, and the thickness deposited. The thickness corresponds to the minimal amount of mass without the emergence of size effects.

Material	Temperature (K)	Phenomena	Thickness (nm)
Indium	429.75	Melting	40
Tin	505.08	Melting	60
Nickel	628.15	Magnetic (FM to PM)	50
Aluminum	933.47	Melting	60

the whole nanocalorimeter is heated above 750 K. Therefore, this calibration method is not useful if we need to carry on experiments at higher temperatures. Our results have shown that in a 4 inches wafer the homogeneity of the metal layer is very large, and temperature coefficient of resistance is constant within 2%.

With the dynamic method, the calibration curve is obtained by using the self-functionality of the device. Different standard materials with well characterized phase transitions are measured with a set of nanocalorimeters. The transition temperature determined with the nanocalorimeter is used as a reference point. Table 2.1 summarizes the main characteristics of materials used for nanocalorimeters calibration, metals easy to evaporate with a low vapor pressure and different transition temperatures. These materials are usually irremovable once deposited, and they must be isolated by means of an inert film with the aim to avoid any intermetallic formation. In this work we used 30 nm SiO₂ as inert layer. Every calibration point means around 100 nm of deposited material, which implies three points as maximum, since higher amounts of mass would alter the nanocalorimeter thermal profile. To define the second order polynomial we also use the resistance measured at room temperature.

The nanocalorimeters temperature profile depends strongly on the heating rate (see Section 3.2 *Principle of operation*), thus the temperature calibration must be done under the similar conditions (vacuum level, current feeding, initial temperature. . .) than those used in the experiment. Subsequently, the steady-state method is especially suitable for the micro-pulsed heating nanocalorimetry, while the dynamic method works very well for the quasi-adiabatic or scanning nanocalorimetry. These techniques and further details are described in Chapter 3. An example of both calibration modes is shown in Figure 2.6.

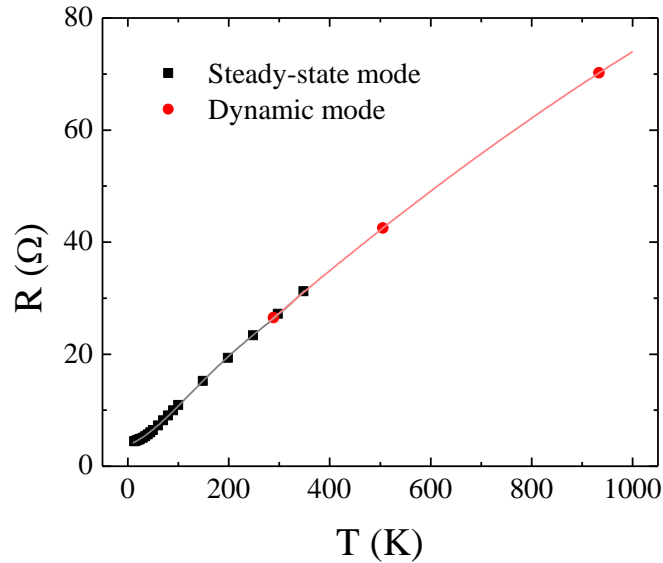


FIG. 2.6 Resistance versus temperature for a given nanocalorimeter using both steady state and dynamic calibration modes. Solid lines are the corresponding 4th and 2nd polynomial fittings for the low and the high temperature regimes, respectively.

2.2 Experimental setups

In this Section, we present the development of three different experimental setups, which have been especially designed and/or adapted to overcome specific challenges in the different experiments presented along the Thesis. They are presented below.

2.2.1 *In-situ* setup

In *in-situ* experiments, we must combine deposition, temperature control and measure capabilities in the same chamber. These kinds of experiments are required when sample must not be exposed to air to avoid oxidation, damage, or contamination. A typical solution to overcome these limitations is the use of capping layers to avoid the contact between sample and air. Nevertheless, the effect of this protective layer on the sample itself might be troublesome, especially in magnetic systems [14–16], precluding the *ex-situ* experiment solution. *In-situ* experiments are also a must when samples are grown at low temperatures and present phase changes at room temperature, particularly when irreversible changes occur, or when sample microstructure might suffer undesired modifications [17, 18].

The samples studied in this Thesis were grown by electron-beam physical vapor deposition (EB-PVD) in the Leybold UNIVEX 450 vacuum chamber shown in Figure 2.7. The equipment permits to evaporate up

2. EXPERIMENTAL SETUP

to 4 different materials controlling the flux rate down to tens of picometers per second, either under high vacuum (below 10^{-5} mbar) or in the presence of reactive atmosphere. The vacuum chamber is equipped with a set of vacuum gauges and gas inlet with mass flow controller, permitting to fix partial pressure of reactive gases atmospheres during growth process.



FIG. 2.7 The *in-situ* experimental setup consisting on a Leybold UNIVEX 450 equipped with the necessary elements to perform nanocalorimetric measurements.

A custom-built thermostatic holder was design and fabricated to control the temperature of the substrate where samples are deposited (in case of nanocalorimeter it fixed the temperature of the Si frame). The holder is built onto a high thermal diffusive substrate, called direct bonded copper (DBC) or insulated metal substrates (IMS) [19]. These types of substrates consist on three layer stack composed by a thick metal covered by a thin dielectric layer (usually an epoxy-based or ceramic layer) and on top a thin layer of copper (typically 35 μm thick). These substrates can be used as printed circuit board (PCB) installing both heater and thermometer and threaded to accommodate the nanocalorimeters with clamps, assuring a perfect thermal cross-link between all the elements.

The fabrication procedure is similar to those employed with PCBs: (1) the circuit is designed and printed in a transparency to be used as a shadow mask, (2) a piece substrate is cut with the mask dimensions, (3) the photoresist is applied by spin coating or spray, (4) using the shadow mask, the non-protected areas of photoresist become monomerized (with positive photoresist) when are irradiated with an ultraviolet

source of light, (5) using a developer the insulated photoresist is removed, (6) the metallic backside of the substrate is protected before the etching, (7) the exposed copper is etched in a solution of $8 \text{ H}_2\text{O} + \text{H}_2\text{O}_2 + \text{HCl}$ (in volume), (8) using deionized water all chemical residues are cleaned and the rest of photoresist are removed with an organic solvent as ethanol, (9) the holder is mechanized with the corresponding holes or threaded holes, (10) the contact pads for the wiring are pre-weld with soldering alloy requiring the use of a high power welder due to the high thermal diffusivity of the substrate, (11) then all the components needed (thermometers, heaters and cables) are welded, and (12) to thermally contact the thermometer to the substrate using cryogenic GE Varnish C5-101 or EpoteK H77 ceramic epoxy. As a thermometer we use a light cryogenic Pt100 that permits to measure temperature with accuracy in the range between 77 and 800 K and as a heater, a thick film power resistor with 22Ω able to dissipate up to 20 W. For the wiring, we use fluxing polyurethane coated copper wire of 0.25 mm diameter. The soldering material used is an alloy with composition 62% Sn, 36% Pb and 2% Ag with activated halogen flux at 3.5%. This material shows a low melting point, around 460 K, which limits the operational working temperatures of the holder. Additionally, the copper layer can be covered with a protective gold layer grown by physical vapor deposition, during the step (2) or by electroplating during the step (9). The purpose of this layer is to prevent the copper oxidation when oxygen liquefies below 90.18 K [8], because of liquid oxygen is a very powerful oxidizing agent [20, 21]. Figure 2.8 shows a photograph of the holder after the entire fabrication procedure.



FIG. 2.8 Image of a thermal holder, for double nanocalorimeters, finished after entire fabrication process.

Inside the vacuum chamber, the thermostatic holder is attached to a thermal reservoir refrigerated by a flux of liquid nitrogen. All electrical contacts arrive from the electrical feedthrough in a shielded wire are thermally grounded into the thermal reservoir at the cryogenic temperature to prevent floating thermoelectric noises. To locally achieve the electrical contacts in the nanocalorimeter, we use wire bonding connecting the platinum pads in the chip to the closer copper (or gold plated) pad strategically placed in the holder.

2. EXPERIMENTAL SETUP

During low temperature experiments and when samples remain long times under high vacuum, as during *in-situ* experiments, water condensation onto samples may be problematic. To avoid this troublesome we made a specific shutter for the calorimetric cells, which blocks the path between water molecules and the cold sample. This shutter is copper made and thermalized by direct contact with the thermal holder backside. In Figure 2.9 we present a scheme of the vacuum chamber inner side with the *in-situ* experimental setup main components.

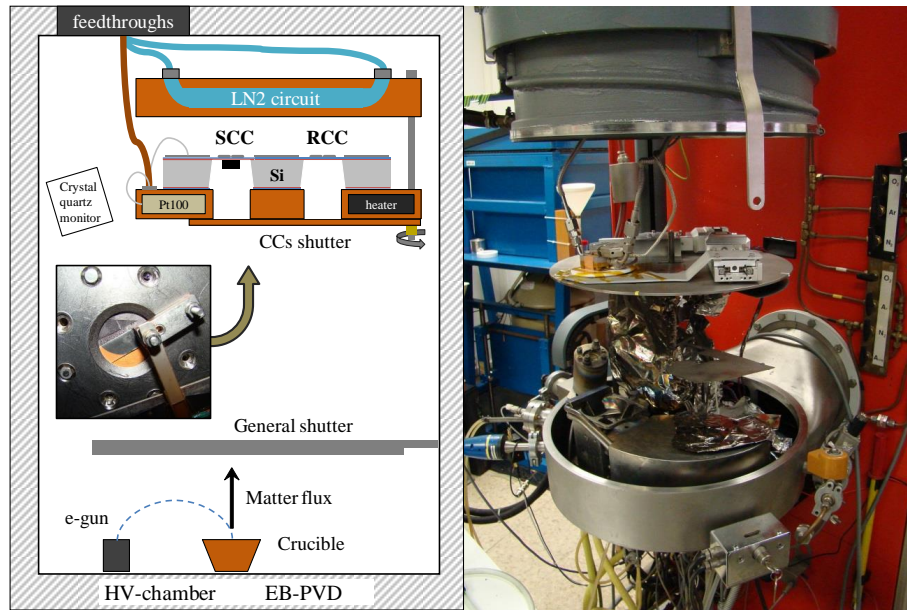


FIG. 2.9 Scheme of the chamber inner part showing its main parts: e-beam gun, general shutter, crystal quartz monitor, dedicated shutter for the calorimetric cells, thermal holder, thermal bath, and electrical and LN2 feedthroughs.

The temperature control of the thermostatic holder is achieved feeding the heater with a high precision current source, typically a Keithley 2400, and the temperature is determined measuring in 4-wire configuration the resistance of the Pt100 with a 6.5 digits high precision digital multimeter (DM). The instruments communicate via GPIB protocol, with a digital PID controller (PC-based) developed in Lab-view that calculates the amount of power released from the evolution of the measured temperature. This custom-built controller permits to fix the holder temperatures with fluctuation smaller than 1% of the value in absolute temperature scale.

We employed two different solutions when sample required substrate temperatures above 400 K during growth. For samples that required *ex-situ* characterizations, we fabricated a high temperature (HT) thermal holder to be heated up to 800 K even in atmospheric pressures. The HT holder is a solid block made of stainless steel with a copper plate on top acting as diffusive layer. In the core of the main block, three holes host the heater cartridges from Watlow (model E2A55-L12) able to debit up to 100 W every one

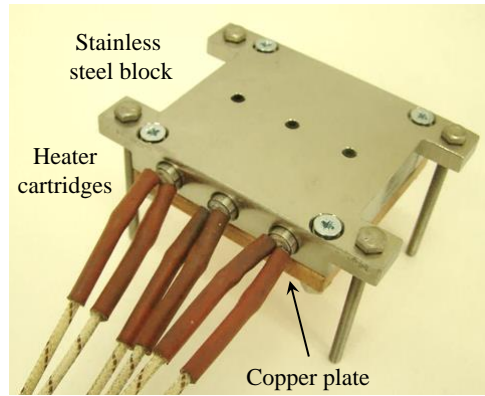


FIG. 2.10 High temperature thermal holder.

(Figure 2.10). The temperature is measured with a Pt100 sensor that is connected in 4-wire configuration and mechanically fixed by a copper clamp. For *in-situ* calorimetric characterizations, the sample can also be grown directly on the devices heating up directly the calorimetric cell in steady state condition up to the required temperature, and 800 K maximum.

2.2.2 Immersion cryostat setup

The analysis of magnetic materials requires an enormous effort from the experimental point of view. With the aim to expand the capabilities of our Group in this research field, we envisioned a liquid helium (LHe) immersion cryostat (Figure 2.11) with the capabilities of applying to the sample relatively high magnetic fields,¹ and to perform an accurate temperature control, which is a requirement of the high sensitive microsecond-pulsed heating nanocalorimetric technique (see Subsection 3.2.2 *Microsecond-pulsed heating nanocalorimetry*). However, the results obtained by nanocalorimetry and presented in this Thesis were obtained without applying magnetic fields. This Section presents the development of a nanocalorimetric setup, containing thermostatic probe, vacuum chamber, and immersion cryostat.

In immersion cryostats the sample is placed at the cryostat bottom. We fulfill the setup requirements by designing and fabricating a cryogenic cane made of non-magnetic stainless steel (see Figure 2.12). At the top of the cane we installed vacuum, cryogenic liquid and electrical feedthroughs. At the bottom side we fabricated the vacuum chamber, which contains the cane header. We placed copper disks along the cane with the aim to avoid thermoacoustic oscillations effect [22, 23].

It is needed to install liquid-level detectors in immersion cryostats to avoid the lack of cryogenic liquid.

¹The immersion cryostat is a ceded equipment by the Institut Néel to our Group, in the framework of our scientific collaboration. This collaboration also included the fabrication of a superconducting coil at the Institut Néel workshops.

2. EXPERIMENTAL SETUP



FIG. 2.11 Immersion cryostat experimental setup with the electronics dedicated to nanocalorimetry, temperature control and magnetic fields generation.

This point is critical when superconducting coils are used for the possibility that the coil may flash. Since an immersion cryostat can be filled in the inner cavity with both LN₂ and LHe, a wide temperature range liquid-level detector has been made and placed in the cryogenic cane (Figure 2.13). Niobium (Nb) has been chosen as the sensor material. The reason is that Nb has a quite high TCR between 77.35 K and room temperature, and also it becomes superconductor below 9.13 K. The sensor was connected in 4-wire configuration and we used a 100 k Ω electrolytic resistance as a heat sink. The sensor was calibrated using three temperature points (Table 2.2), since the resistance value varies linearly with liquid level. Feeding current values are typically in the order of 1 mA for LN₂, with a power dissipation of 100 mW, whereas with LHe 10 μ A are used to dissipate 10 μ W.

The cane header consists on a copper made quasi-static thermal probe, which is attached to a copper block by means of a stainless steel rod (Figure 2.14). At low temperatures, the stainless steel rod ensures low heat transfer between the two linking elements. Hence, under high vacuum conditions the quasi-static probe is thermally isolated from surroundings, which ensures a fine temperature control provided

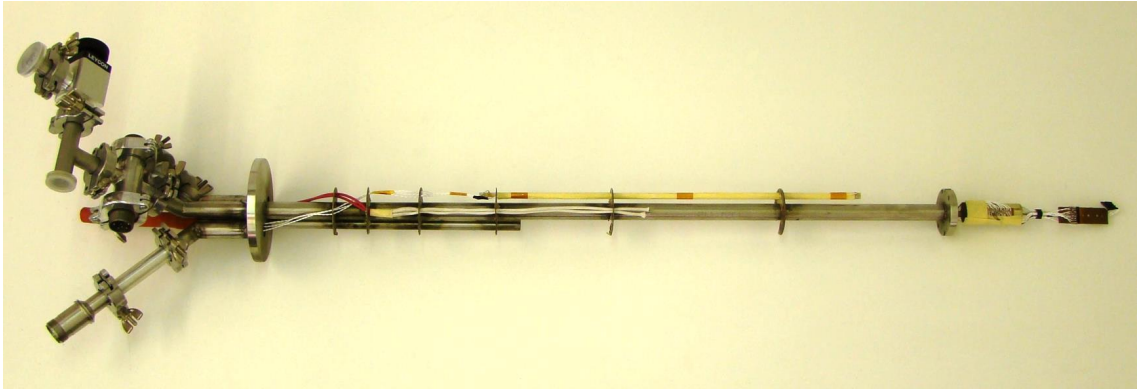


FIG. 2.12 Cryogenic cane feedthroughs side (left), and chamber side (right).

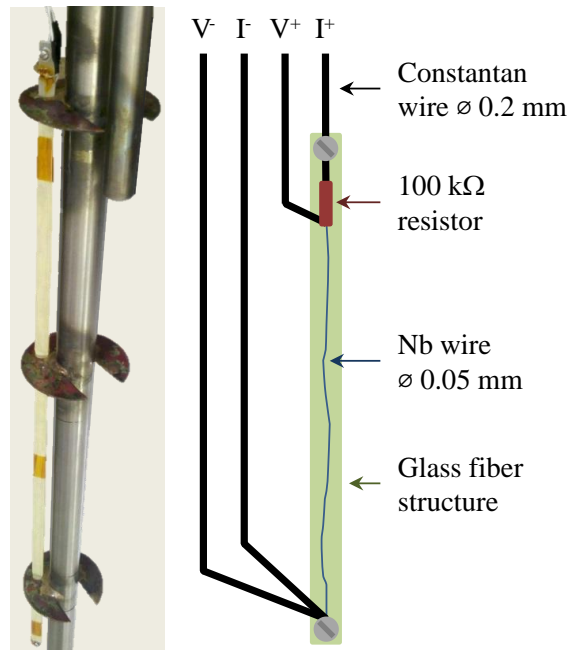


FIG. 2.13 Image of the liquid-level detector installed in the cryogenic cane (left), and a scheme (right).

by the heater and thermometers installed on its backside [Figure 2.14(b) inset]. The front side fits with specially fabricated thermal holders, where the nanocalorimeters are placed [Figure 2.14(a) inset]. During experiments, the quasi-static probe front side is covered with a copper shield to reduce heat transfer by radiation [24]. The copper block is an essential element, especially at low temperature experiments, when it acts as thermal bath and thermalizes the wiring from the welding down. This fact avoids the presence of thermoelectric potentials due to Seebeck effect in the quasi-static probe. For the welding we used a low temperature Sn-Pb-Ag-based flux-free alloy, which melting temperature is around 450 K. For the wiring, from feedthroughs down to the quasi-static probe, we used as a regular wire constantan ($\text{Cu}_{55}\text{Ni}_{45}$ alloy) cables, 0.2 mm diameter and white PTFE coating, while for the heater feeding we used copper cables, 0.2 mm diameter and brown PTFE coating. The quasi-static probe is equipped with a resistive heater, which is thermally controlled with the same instrumentation than presented for the thermal

2. EXPERIMENTAL SETUP

TABLE 2.2 Resistance values of the Nb liquid-level detector at different temperatures, when the whole detector is at the indicated temperature.

Temperature (K)	Resistance (Ω)
~ 295	~ 48
77.35	13.5
< 9.13	0

holders used in the *in-situ* experimental setup. The use of high precision DMs, together with suitable performance between heat transfer and thermal link, permits to reach reduced temperature peak-to-peak noises (below 1 mK) in the whole range of operation temperatures from 80 to 400 K.

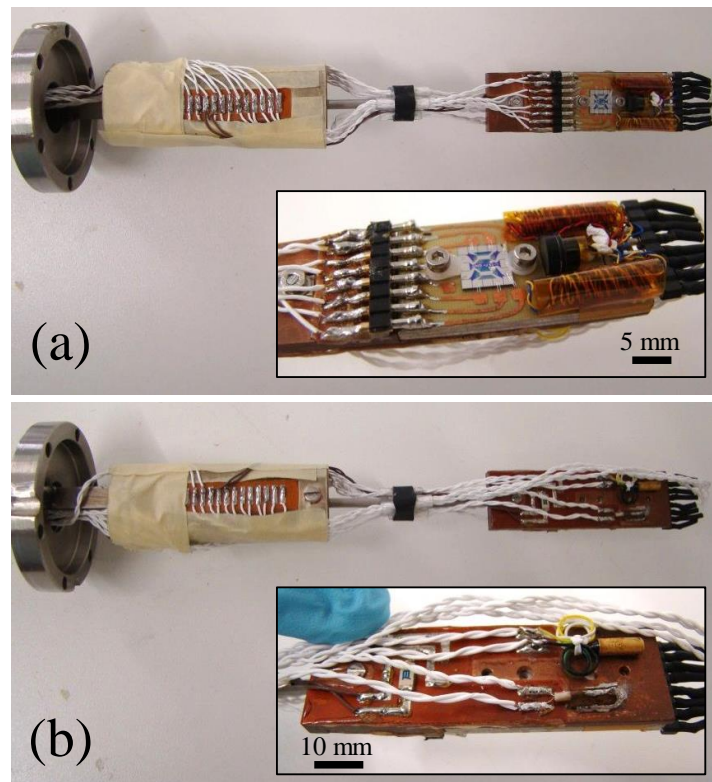


FIG. 2.14 Cane header images. (a) Header front side view, with an IMS probe installed on the quasi-static probe at right, and the copper thermalizing block at left. The inset shows a nanocalorimeter (a double one) bonded to the thermal holder and a Hall cryogenic probe. (b) Header back side view. The inset shows in detail the temperature control elements installed: the heater (left), the GeRT (top right) and the Pt100 (bottom right).

2.2.3 Specific XRD setup

Simultaneous XRD and nanocalorimetry measurements monitoring the solid state phase formation of palladium silicide, Pd₂Si, during the thermal processing of palladium/amorphous silicon bilayers were performed at the MSPD beamline of the ALBA synchrotron (Barcelona, Spain). In this section we describe the experimental developments required for that purpose.

A vacuum chamber was specially designed to simultaneously perform the nanocalorimetric measurements and the X-ray diffraction experiments in the MSPD beamline (Figure 2.15). The chamber is equipped with two Kapton view ports of 5 cm diameter with a reduced thickness of 25 μm to minimize X-ray absorption. Inside the chamber the calorimeters are loaded into a mount-holder that geometrically places the nanocalorimeters at the centre of the goniometer, which is tilted 15° with respect to the incident X-ray beam [Figure 2.16(a)]. The holder is also used to bring the electrical contacts from the electrical feed-through close to the chip and locally wire-bond the heater/sensor elements and to fix the base temperature using a fluid bath while measuring it with a Pt100 sensor. A schematic view and the photographic detail of the chamber are shown in Figure 2.16.

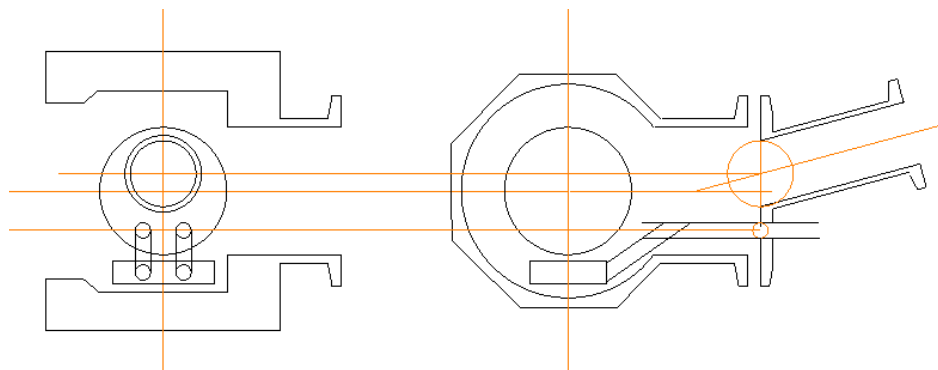


FIG. 2.15 Schematics of the vacuum chamber corresponding to the in-situ synchrotron XRD setup. From the point of view of the incident beam, the left projection corresponds to the lateral view, while right projection corresponds to the head-on view.

The beam energy is fixed to 15 keV. The detector is a Mythen [Figure 2.16(b)], which is a very fast and sensitive 1D detector, covering an angular range 2θ from 19° to 59°, which permits to take a high number of counts per unit time [25, 26]. The obtained Pd₂Si thin film samples have a mass below 1 μg, which is enough for the sensitivity of both the power compensated nanocalorimetric technique (see Subsection 3.2.3 *Power compensated nanocalorimetry*) and the fast-XRD acquisition. Even so, the very small amount of sample imposes a minimum time to acquire a reasonable signal-to-noise signal, around 1 s. As a consequence the maximum heating rate of the experiments is set to 10 K/s. With these parameters one X-ray spectra is taken every 10 K at the fastest heating rate.

2. EXPERIMENTAL SETUP

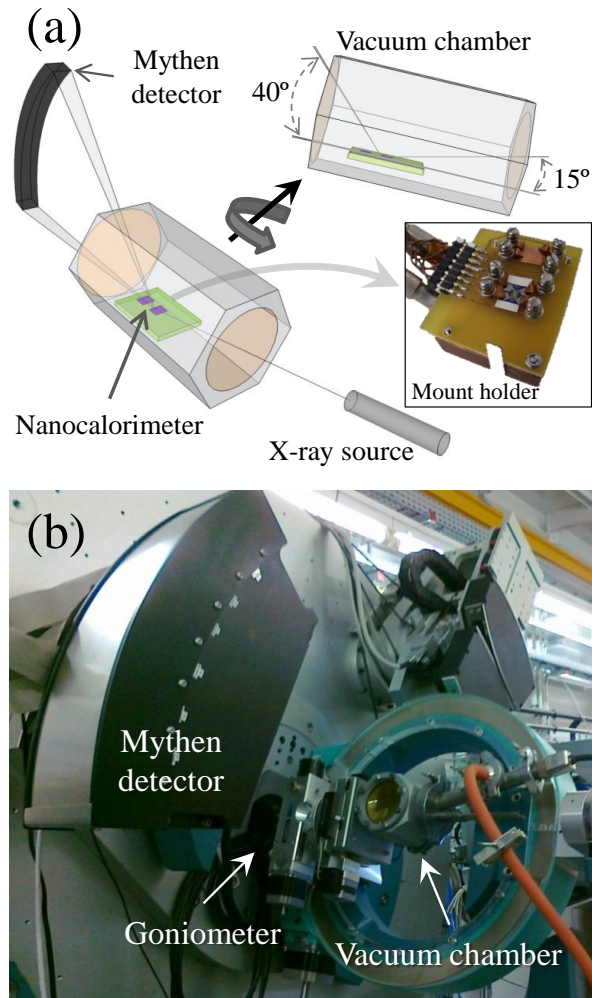


FIG. 2.16 (a) Schematics of the experimental setup with the nanocalorimeters inside the vacuum chamber. (b) Experimental setup image with the vacuum chamber in the center and Mythen detector on the left.

A cumbersome task when both techniques are used simultaneously is beam alignment. In fact, the visible sensing area for the beam is the 15° vertical projection of the real sample area ($\sim 1 \text{ mm}^2$), so that, the beam dimensions are fixed to 700 μm wide by 300 μm high. The alignment procedure was realized in three steps: (i) localizing and centering the beam onto the nanocalorimeter with the help of fluorescent paper placed on its edges, (ii) finding the sensing area using the PI controller as a thermal detector. The use of membrane-based structures allows monitoring the X-ray induced heating by locally measuring the temperature increase of the sensing area of the device. This temperature rise has been used here to fine tune the position of the beam with respect to the sample which is exactly located beneath the Pt heater/sensor, and finally (iii) since the heater is made of Pt, we search the position that maximizes the Pt X-ray signal in the diffraction pattern. The alignment methodology, which takes full advantage of the membrane-based geometry of the calorimetric chips, allowed a highly time-effective process and was routinely applied to all thin film samples analyzed in this work. The results are presented in Subsection 5.4.5 *Simultaneous characterization by synchrotron radiation*.

2.3 Conclusions

We have prepared series of nanocalorimeters, describing its microfabrication and the main aspects related to its operation. In this sense, adequate heating rates and working temperature ranges have been determined using a proper temperatures calibration, which has been achieved for low or high temperatures following two different methodologies.

We have designed and fabricated three different experimental setups allowing the use of nanocalorimetry in divers environments and conditions: (i) a setup adapted to a vacuum deposition chamber to perform *in-situ* measurements at low temperature on fresh deposited films, (ii) an immersion cryostat setup to realize experiments at low temperature with an accurate temperature control, and with the possibility to apply magnetic fields, and finally, (iii) a specific XRD setup to observe simultaneously phase transitions by nanocalorimetry and samples structure by diffraction.

References

- [1] A. F. Lopeandia. *Development of Membrane-based Calorimeters to Measure Phase Transitions at the Nanoscale*. PhD thesis, Universitat Autònoma de Barcelona, February 2007.
- [2] D. W. Denlinger, E. N. Abarra, K. Allen, P. W. Rooney, M. T. Messer, S. K. Watson, and F. Hellman. Thin film microcalorimeter for heat capacity measurements. *Review of Scientific Instruments*, 65(4):946–959, 1994.
- [3] S. L. Lai, G. Ramanath, and L. H. Allen. High speed (10^4 °C/s) scanning microcalorimetry with monolayer sensitivity (J/m^2). *Applied Physics Letters*, 67(9):1229–1231, 1995.
- [4] F. Fominaya, T. Fournier, P. Gandit, and J. Chaussy. Nanocalorimeter for high resolution measurements of low temperature heat capacities of thin films and single crystals. *Review of Scientific Instruments*, 68(11):4191, 1997.
- [5] M. J. Madou. *Fundamentals of Microfabrication: The Science of Miniaturization*. CRC Press, 2 ed. edition, 2002.
- [6] M. Y. Efremov, E. A. Olson, M. Zhang, S. L. Lai, F. Schiettekatte, Z. S. Zhang, and L. H. Allen. Thin-film differential scanning nanocalorimetry: heat capacity analysis. *Thermochimica Acta*,

References

- 412:13–23, 2004.
- [7] T. J. Quinn. *Temperature*. Monographs in Physical Measurement. Academic Press, 1983.
- [8] H. Preston-Thomas. The International Temperature Scale of 1990 (ITS-90). *Metrologia*, 27(1):3–10, 1990.
- [9] A. F. Lopeandia, F. Pi, and J. Rodríguez-Viejo. Nanocalorimetric analysis of the ferromagnetic transition in ultrathin films of nickel. *Applied Physics Letters*, 92(12):122503, 2008.
- [10] E. Leon-Gutierrez, G. Garcia, A. F. Lopeandia, M. T. Clavaguera-Mora, and J. Rodríguez-Viejo. Size Effects and Extraordinary Stability of Ultrathin Vapor Deposited Glassy Films of Toluene. *The Journal of Physical Chemistry Letters*, 1(1):341–345, January 2010.
- [11] M. Molina-Ruiz, A. F. Lopeandia, F. Pi, D. Givord, O. Bourgeois, and J. Rodríguez-Viejo. Evidence of finite-size effect on the Néel temperature in ultrathin layers of CoO nanograins. *Physical Review B*, 83(14):140407, April 2011.
- [12] A. F. Lopeandia, J. Valenzuela, and J. Rodríguez-Viejo. Power compensated thin film calorimetry at fast heating rates. *Sensors and Actuators A*, 143(2):256–264, 2008.
- [13] Manel Molina-Ruiz, Aitor F. Lopeandía, Marta Gonzalez-Silveira, Gemma Garcia, Inma Peral, Maria T. Clavaguera-Mora, and Javier Rodríguez-Viejo. Kinetics of silicide formation over a wide range of heating rates spanning six orders of magnitude. *Applied Physics Letters*, 105(1):013113, July 2014.
- [14] J-H Ku, C-S Kim, C-J Choi, K. Fujihara, H-K Kang, M-Y Lee, J-H Chung, E-J Lee, J-E Lee, and K-H Ko. New effect of Ti-capping layer in Co silicide process promising for deep sub-quarter micron technology. In *International Interconnect Technology Conference*, pages 256–258. IEEE, 1999.
- [15] J. Arbiol, F. Peiro, A. Cornet, C. Clavero, A. Cebollada, G. Armelles, and Y. Huttel. Capping layer effects in the structure and composition of Co nanoparticle ultrathin films. *Applied Physics Letters*, 86(3):032510, January 2005.
- [16] N. L. Chung, M. B. A. Jalil, and S. G. Tan. Effects of capping layer on the spin accumulation and spin torque in magnetic multilayers. *Journal of Physics D: Applied Physics*, 42(19):195502,

October 2009.

- [17] A. Sepúlveda, E. Leon-Gutierrez, M. Gonzalez-Silveira, C. Rodríguez-Tinoco, M. T. Clavaguera-Mora, and J. Rodríguez-Viejo. Accelerated Aging in Ultrathin Films of a Molecular Glass Former. *Physical Review Letters*, 107(2):025901, July 2011.
- [18] A. Sepúlveda, E. Leon-Gutierrez, M. Gonzalez-Silveira, C. Rodríguez-Tinoco, M. T. Clavaguera-Mora, and J. Rodríguez-Viejo. Glass transition in ultrathin films of amorphous solid water. *The Journal of Chemical Physics*, 137(24):244506, December 2012.
- [19] C. V. Godbold, V. A. Sankaran, and J. L. Hudgins. Thermal Analysis of High-Power Modules. *IEEE Transactions on Power Electronics*, 12(1):3–11, 1997.
- [20] L. Crocco and S-I Cheng. *Theory of combustion instability in liquid propellant rocket motors*. Butterworths Scientific Publications, New York, 1956.
- [21] W. Mayer and H. Tamura. Propellant injection in a liquid oxygen/gaseous hydrogen rocket engine. *Journal of Propulsion and Power*, 12(6):1137–1147, November 1996.
- [22] K. W. Taconis, J. J. M. Beenakker, A. O. C. Nier, and L. T. Aldrich. Measurements concerning the vapour-liquid equilibrium of solutions of He^3 in He^4 below 2.19°K. *Physica*, 15(8-9):733–739, 1949.
- [23] H. A. Kramers. Vibrations of a gas column. *Physica*, 15(11-12):971–984, 1949.
- [24] G. K. White and P. J. Meeson. *Experimental Techniques in Low-Temperature Physics*. Oxford University Press, New York, 4th edition, 2002.
- [25] M. Knapp, I. Peral, L. Nikitina, M. Quispe, and S. Ferrer. Technical concept of the materials science beamline at ALBA. *Zeitschrift für Kristallographie Proc.*, 1:137–142, 2011.
- [26] F. Fauth, I. Peral, C. Popescu, and M. Knapp. The new Material Science Powder Diffraction beamline at ALBA Synchrotron. *Powder Diffraction*, 28(S2):S360–S370, November 2013.

3. Nanocalorimetry: optimizing the old, developing the new

Nanocalorimetry is a characterization technique suitable to determine the small amounts of energy involved in thermal process of nano-sized samples. Nanocalorimetric measurements gives access to basic thermodynamic and kinetic information like sample heat capacity, entropy changes, transition temperature and enthalpies. To obtain enhanced sensitivities compared with commercial devices the miniaturization of calorimetric cells has resulted crucial. With the advances in microfabrication techniques a new family of devices has appeared into scientific scenario, and several nanocalorimetric methods have been implemented.

In this Chapter we state some fundamentals about thermodynamic potentials, properties, and experimental parameters. Likewise, we present the different operational methods that we have implemented and employed during this work. Among them, we highlight a new nanocalorimetric technique, the microsecond-pulsed heating nanocalorimetry (μ -PHnC). This technique, that combines the best features of AC and DC calorimetries, has been completely developed during the realization of this Thesis. Finally, we present the methodology used to date to calculate the heat capacity from data processing, and a new methodology that we have developed, which increases accuracy and sensitivity on obtained results. We explain the sensitivity improvement through a noise analysis of the most relevant terms within both methodologies.

3.1 Calorimetry and thermodynamics

As scientists, our primary interface with nature is through the properties of macroscopic matter. The existence of underlying relationships between these properties has far reaching implications. For example, the energy of every atom in matter is related to their macroscopic average, the temperature, or

the magnetic interaction between electrons that belong to different atoms is macroscopically observed as a particular magnetic behavior. The challenge is to find tools that help us to relate these properties together. Calorimetry is one of them; it is the science that measures heat transfer in a body with the purpose to associate observed variations with state variables. With the establishment of the mechanical equivalence of heat by Joule, in the second half of the 19th century, the concept of conservation of energy was clearly formulated. Then, the laws of thermodynamics state some fundamentals: closed system, exchange, reversibility, heat, work. . . These concepts contributed to the development of the first calorimeter by Antoine Lavoisier and Pierre-Simone Laplace, during the winter of 1782-83. From that moment, calorimetric techniques experienced a continuous evolution, and they can be classified as direct or indirect calorimetry. For the former, the heat is calculated directly from the sample, while for the later, the heat is calculated measuring secondary reactions. Another classification criteria is taking into account their operation principle, here we can distinguish between adiabatic calorimetry, where there is no heat exchange with the surroundings, and isoperibol calorimetry, where the temperature of the surroundings is kept constant. Today, the most used calorimeters are based on the isoperibol principle, as differential scanning calorimetry. However, nanomaterials force the continuous size reduction of samples, which are easily measurable by adiabatic calorimetry.

In spite of the recent technological advances, it is not possible to make a perfectly adiabatic calorimeter, whose unique requirement is that power losses lead to zero. Equation 3.1 describes the adiabatic calorimeter dynamics, where the total heat capacity multiplied by the heating rate is equal to the total power, represented as a sum of the power released by the heater and the power lost by heat transfer.

$$(C_{CC} + C_{sample}) \frac{dT}{dt} = P_{in} - K(T - T_0) + \frac{dH_{sample}}{dt} \quad (3.1)$$

where C_{CC} is the calorimetric cell heat capacity, C_{sample} is the sample heat capacity, P_{in} is the power supplied, K is the thermal link, and H_{sample} is the sample enthalpy variation with time. Figure 3.1 represents the adiabatic calorimeter dynamics where for the ideal case $K = 0$.

In samples that undergo a first-order phase transition, that involves a latent heat, the enthalpy variation contributes to the heat capacity measured by the calorimeter. While for second-order phase transitions, as magnetic transitions, the dH/dt term is zero. However, materials that suffer a second-order phase transition present a discontinuity on heat capacity due to a divergence on their susceptibility. Under that heat capacity signal, there is a great quantity of information about the lattice, electronic, and magnetic properties of such materials. By using the Debye model [1], which estimates the phonon contribution to the heat capacity in a solid, it is possible to separate both contributions, lattice and magnetic.

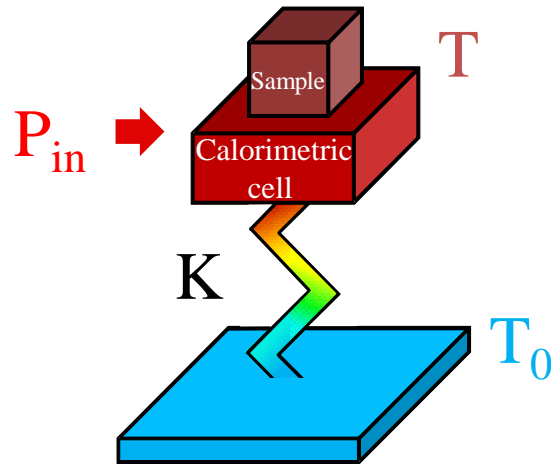


FIG. 3.1 Adiabatic calorimeter dynamics.

3.2 Principle of operation

Quantitative calorimetric measurements, in any type of calorimetric cell, require the simultaneous monitoring of the temperature evolution, the power injected and (if non-adiabatic) the amount of heat lost to the surroundings. In the nanoscale counterpart device, to operate the thin film calorimetric cell, the metallic meander should be electrically polarized. With the pass of electrons the metallic element releases heat by Joule effect, promoting the rise in temperature of the complete CC including the thin dielectric membrane beneath it. Playing with the width of the strip lines, the power density dissipated can be tuned. Following this idea the metallic layout design includes two wide strips to feed the meander with a known current $I(t)$. To locally measure the instantaneous voltage drop in the meander, $V(t)$, the design includes two extra electrical lines. The 4-wire configuration [Figure 3.2(a)] permits to measure only the amount of power released in that central area (also refereed as sensing area), $P_{in}(t) = V(t)I(t)$, and to determine the resistance of the meander zone, $R(t) = V(t)/I(t)$.

Figure 3.2(c) shows the cross-section schematics of a calorimetric cell with ~ 100 nm metallic thin film heater/thermometer on top of the 180 nm Si_3N_4 membrane. At room temperature, the characteristic resistance of this metallic element is around 30Ω with a temperature coefficient of resistance (TCR) around 0.0026 K^{-1} , and the total heat capacity addenda of the sensing area is as low as $0.6 \mu\text{J/K}$. Working under high vacuum conditions, the pathway for heat losses from the calorimetric cell towards the surroundings is limited to the heat conduction through the membrane and radiation, and values of effective thermal conductance around $4 \mu\text{W/K}$, at room temperature, are systematically obtained. Therefore, the CCs thermal dynamics are very fast with characteristic times ($\tau \sim 150$ ms). For example, when we actuate the heater with short current pulses (50 mA during few ms), the heat is released by Joule effect

(~ 75 mW) promoting high heating rates on the CC ($\beta \sim 10^5$ K/s). If current feeding the device is kept in time (DC case) the device reaches steady-state conditions after times much longer than τ , as can be appreciated in Figure 3.2(b). Along this Chapter, we will present how injecting different current signal in the heater the temperature evolution can be forced to follow different heating rates.

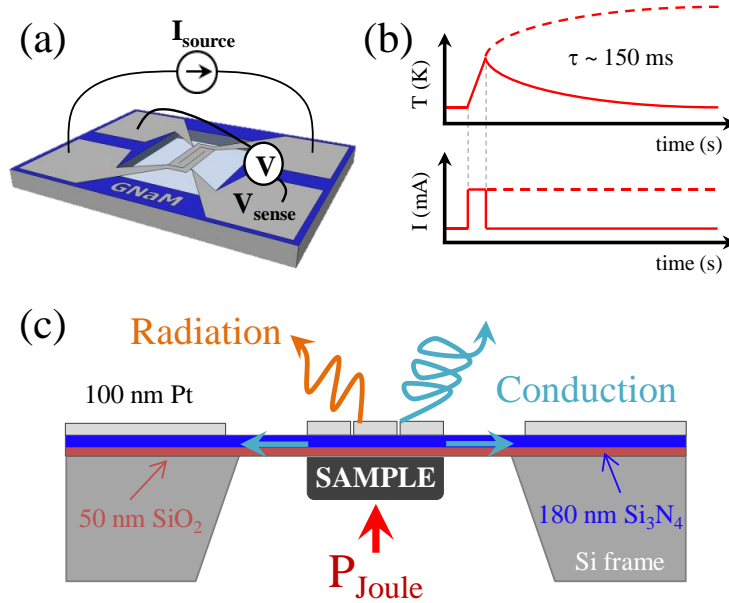


FIG. 3.2 Nanocalorimeter principle of operation. (a) Connections scheme with current feeding and voltage sense. (b) Nanocalorimeter temperature dynamics when working in pulsed mode (continuous line), or steady-state (dashed line). (c) Scheme of a nanocalorimeter cross section, showing metallic elements, membrane, sample, silicon frame, and power input and energy dissipation mechanisms.

This type of calorimeters are especially suited to measure evaporated or spin coated [2] samples with reduced thicknesses. For evaporated samples, the use of the self-aligning microfabricated shadow mask permits to delimit the sample deposition to the sensing area. The planar geometry guarantees an excellent thermal contact between metallic element and sample (when it has a reduced out of plane dimension) opening the possibility to reach huge heating dynamics (up to 10^6 K/s) and enhancing the calorimetric sensitivity. Even measuring low thermal conductive samples, if the out-of-plane dimension is kept in the nanoscale range, the vertical temperature gradients in the CCs can be neglected and, therefore, the 2D temperature map of the sample follows the one described by the metallic element.

A general drawback of this type of thin film cells concerns the homogeneity of the in-plane 2D temperature map. When heating the device to a given temperature in steady-state conditions, the temperature map is parabolic, promoting large differences during the analysis. To use the devices at low heating rates one solution is to evaporate a thick thermal diffusion layer in the sensing area. Nevertheless, the reduced thickness of the cell limits the lateral diffusivity of heat, and for very fast heating rates in the short time scale of the experiment, the power dissipated locally heats the cell and quite flat temperature maps can

be found. For $\beta > 5 \times 10^5$ K/s the major difference in temperatures inside the sensing area is around 15 K. Figure 3.3, shows a finite element modeling of the heat transfer in the CC done under the platform COM-SOL Multiphysics. All the data for the material (heat capacity, densities, resistivity, thermal conductivity, and emissivity) can be found elsewhere [3]. The surface plot of Figure 3.3(a) shows the temperature map in steady-state conditions with the characteristic parabolic profile. Figure 3.3(b) shows the image for 10 ms temperature map starting a heating ramp at 8×10^4 K/s. The inclusion of thermal diffusive layers, permits in some experiments (especially those done at slow heating rates) mitigate this difficulty. The non-homogeneities in the temperature maps also impose a restriction on the characteristic of sensor used. Only materials with a linear dependence on their $R(T)$ function (at least in the temperature range larger than the one defined by the inhomogeneities) can be used to determine the average temperature in the sensing area from a single resistance value. Materials with non-linearities require deconvolution knowing the expected temperature maps.

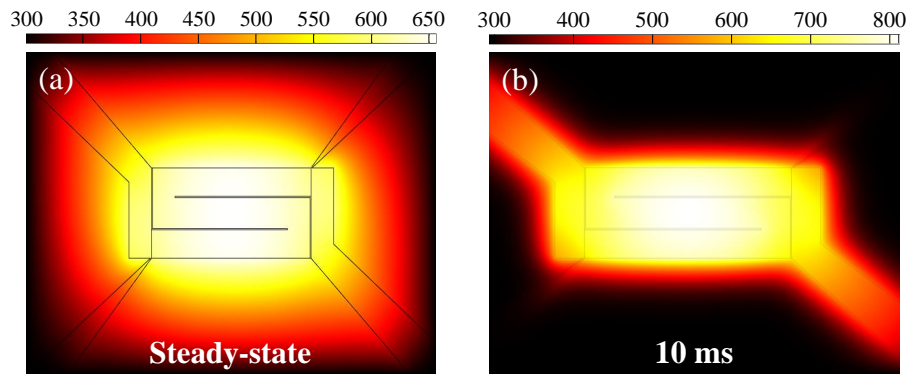


FIG. 3.3 Images of the Comsol Multiphysics finite element modeling for heat transfer in the calorimetric cell for (a) steady-state, and (b) 10 ms feeding at 8×10^4 K/s.

3.2.1 Quasi-adiabatic nanocalorimetry

Quasi-adiabatic nanocalorimetry is an adaptation of the pulsed heating traditional method [4], where the calorimetric cell is heated by Joule effect at high heating rates to approximate adiabatic conditions. Being developed by the Group of Leslie Allen at the University of Illinois it is now used by different research groups worldwide. As described above, when introducing a current pulse in the range of few tens of mA the calorimetric cell becomes heated at rates around 10^5 K/s. Comparing this heating values with characteristic cooling rates (lower than 5% of the heating rate) of the cells it is possible to conclude that the cell behaves quasi-adiabatically. Figure 3.4 shows the electrical diagram used to measure the heat capacity of a single nanocalorimeter. A computer (NI PXI-8187) controls via GPIB a high resolution (16 bits) current source Keithley 2400 able to generate different width pulses depending on requirements

(the minimum width is 0.5 ms due to the initial transient and it may be incremented in steps 0.1 ms), and amplitude that can be fixed in the range required (20-100 mA) with large precision (down to 5 μ A). Synchronized with the current pulse, the signal acquisition required in the nanocalorimetric experiment is achieved using a data acquisition card (DAQ) from National Instruments (NI). The NI PXI 6123 is a DAQ able to measure simultaneously up to 8 channels with a resolution of 16 bits at velocities up to 5×10^5 samples per second. Figure 3.4 shows the schematic view of the setup used to make nanocalorimetric measurements in a single device; usually referred as a *non-differential setup*. Between the device connection and DAQ there is a pre-amplification stage that serves to accommodate the signal to the card range (amplifying), and also to isolate electrically the nanocalorimeter and prevent any current leakage from the calorimeter towards the rest of the instruments. For that reason we have used as amplifier the INA111, a high speed (only 4 μ s settling time) FET-input (only 20 pA as max.) instrumentation amplifier, with a very low noise (10 nV $\text{Hz}^{-1/2}$ at 1 kHz) and a high common mode rejection ratio (106 dB). As shown in Figure 3.4, a high precision load resistance (R_i) is connected in series to be used as reference for measuring current flowing through. The two voltages measured in the non-differential method ($V_S(t)$ and $V_i(t)$) permit to calculate the rest of the required variables as follows: the current flowing ($I(t) = V_i(t)/R_i$), the resistance of the meander ($R_S(t) = R_i V_S(t)/V_i(t)$), the CC temperature ($T_S(t) = T(R_S(t))$ from the $R(T)$ calibration function) and the heating rate ($\beta_S(t) = dT_S(t)/dt$).

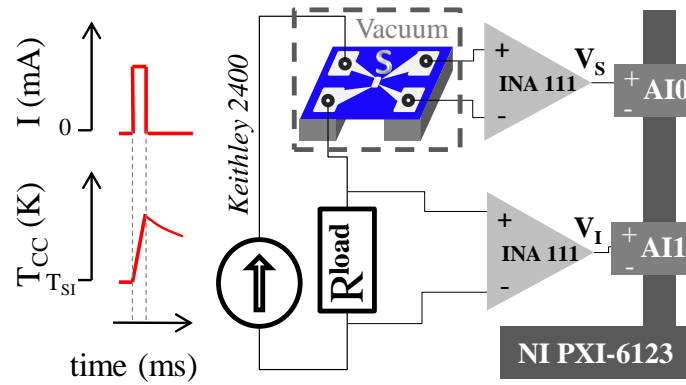


FIG. 3.4 Non-differential setup for quasi-adiabatic nanocalorimetry.

If quasi-adiabatic requirements are accomplished (vacuum environment), in a first approximation, we can consider that most of the heat released in the calorimetric cell $P_{in}(t) = V_S(t)V_i(t)/R_i$ contributes to the inner energy of the complete cell. In this scenario P_{in} is much larger than the coexisting heat losses term (P_{losses}). In a general expression, the direct measurement resembles the real heat capacity with an additional term which includes the losses weighted by the heating rate. For a measurement done at a heating rate β the apparent heat capacity for the single calorimetric cell can be expressed as

$$C_{P_\beta}^{CC}(t) = \frac{P_{in}(t)}{\beta(t)} = C_{P_{real}}^{CC}(t) + \frac{P_{losses}(t)}{\beta(t)} \quad (3.2)$$

3. NANOCALORIMETRY: OPTIMIZING THE OLD, DEVELOPING THE NEW

$P_{losses}(t)$ term accounts for the amount of energy lost per unit time at a given moment during the scan. This term depends on the temperature 2D map of the cell at the evaluated time and includes conduction through the membrane and heat radiation. For ultrafast heating ramps, it is expected to have very flat profile (non-diffusive situation) in the calorimetric cell, and then it is possible to assign a given power lost for each temperature $P_{losses}(T)$. At low temperature, P_{losses} should be dominated by conduction showing a linear dependence with temperature, while at high temperature, higher order dependences are expected to appear when emission starts playing a bigger role. In a first approximation P_{losses} term can be evaluated by measuring the calorimetric cell apparent heat capacity ($C_{P\beta}^{CC}$) at different rates [Figure 3.5(a)], always applying a heating rate large enough to preserve the temperature profile [5,6]. As can be seen in Figure 3.5(b), when plotting the values of $C_{P\beta}^{CC}(T)$ respect to the inverse of the heating rate $1/\beta$ for a given temperature, the real heat capacity of the cell, $C_{P_{real}}^{CC}(T)$, can be estimated as the intercept with the coordinate axis, C_P when $\beta = \infty$, and the $P_{losses}(T)$ term as the slope of the curve obtained from every temperature.

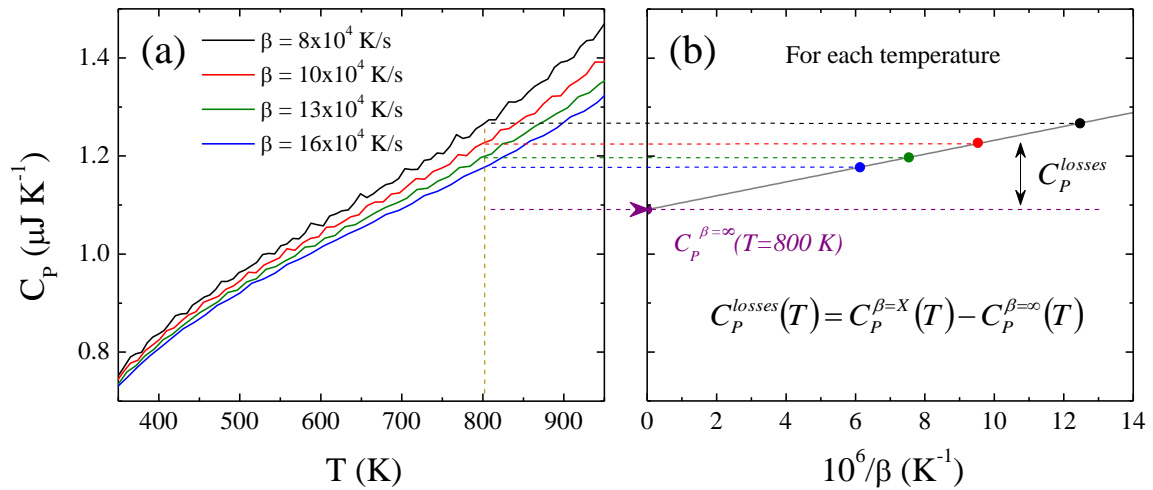


FIG. 3.5 (a) Heat capacity measured at different heating rates. (b) Heat capacity values for a given temperature plotted respect to the inverse of the heating rate.

With the incorporation of a sample, the $P_{losses}(T)$ term may be slightly influenced. Nevertheless, we minimize this perturbation if the sample is perfectly placed only in the sensing area (with the shadow mask) preventing to modify the link through conduction. Only for thick samples, the emissivity may substantially influence P_{losses} , but for very thin samples the effect is negligible. That fact permits to measure with accuracy the heat capacity of a thin film sample deposited in a nanocalorimeter $C_P^{\text{sample}}(T)$. Using the non-differential configuration, we can compare two consecutive scans of the same calorimetric cell: the scan when the sample has been evaporated in the calorimetric cell (denoted with superscript 1) and, the previous one, when calorimetric cell was initially idle (denoted with superscript 0). If samples are very small both scans would achieve similar heating rates and heat losses term becomes cancelled,

then the sample heat capacity $C_P^{sample}(T)$ can be estimated from the subtraction of the apparent heat capacities

$$C_P^{sample}(T) = C_{P_{real}}^{CC,1}(T) - C_{P_{real}}^{CC,0}(T) \approx C_{P_\beta}^{CC,1}(T) - C_{P_\beta}^{CC,0}(T) \quad (3.3)$$

If the amount of sample deposited is large, the heating rate will drastically decrease in the later scan and corrections considering the influence of the power losses will be required. In this case, it is needed to measure in advance the P_{losses} term for the CC following the strategy explained above.

$$C_P^{sample}(T) = C_{P_{\beta_1}}^{CC,1}(T) - \frac{P_{losses}(T)}{\beta_1(T)} - C_{P_{\beta_0}}^{CC,0}(T) - \frac{P_{losses}(T)}{\beta_0(T)} \quad (3.4)$$

When the introduction of a sample influences $P_{losses}(T)$, last analysis should consider the measurement of $P_{losses}(T)$ after sample inclusion. This non-differential method, is similar to that presented by Allen and coworkers [5], and reports very accurate values of heat capacity but with a large dispersion. Major source of noise arise from the differentiation process of the digitized data. Regarding our electronics setup, in the best scenario, with a perfect signal conditioning taking profit of the full acquisition range, raw data is acquired with a maximum signal-to-noise ratio (SNR) of 2×10^4 , since a minimum background digital noise corresponding to 3 LSB (least significant bit) is always present. This value is far over the Johnson-Nyquist noise level. The propagation of this noise in the differentiation process of the digitized voltage data is essentially what degrades the SNR of the final heat capacity signature. For single shot experiments, the better ΔC_P precision is over few tens of nJ/K.

In the literature it is possible to find a complete analysis of noise propagation [7]. Here we present a short analysis to clarify some limitations of the quasi-adiabatic technique. The analysis is centered in the generation of noise during the digitalization and how it propagates in the expression of the apparent heat capacity. The apparent heat capacity is obtained measuring V_S and V_i , both acquired by a 16 bits DAQ at a given frequency (f). The signal-to-noise ratio is $SNR = V/\eta_V$, where η_V is the RMS value of a given parameter, the voltage in this case. Considering a measurement performed with the non-differential configuration (see Figure 3.4), the expression for the apparent heat capacity is:

$$C_{P_\beta}^{CC}(t) = \frac{P_{in}(t)}{\beta(t)} \quad (3.5)$$

The power input can be shown as a function of the variables measured, first substituting the power input term

$$P_{in}(t) = V_S(t)I(t) = V_S(t)\frac{V_i(t)}{R_{load}} \quad (3.6)$$

And subsequently, the heating rate can be rewritten considering the linear dependence of the resistance

3. NANOCALORIMETRY: OPTIMIZING THE OLD, DEVELOPING THE NEW

with temperature, $(dR_S/dT)_{T_0} = \alpha R_S$, then

$$\begin{aligned}\beta(t) &= \frac{dT(t)}{dt} = \frac{dT}{dR_S} \frac{dR_S(t)}{dt} = \frac{1}{\alpha R_S} \frac{dR_S(t)}{dt} = \\ &= \frac{1}{\alpha R_S} \frac{d}{dt} \left(V_S(t) \frac{R_{load}}{V_i(t)} \right) = \frac{1}{\alpha V_S} \frac{dV_i(t)}{dt} - \frac{1}{\alpha V_i} \frac{dV_S(t)}{dt}\end{aligned}\quad (3.7)$$

Typically the R_{load} is selected to obtain $V_i \sim V_S$, for that reason we can simplify the expression and analyze the noise propagation of voltage (η_{V_S} and η_{V_i}) into the power input expression, $\eta_{P_{in}} \cong \eta_V V/R_{load}$, and for the heating rate, $\eta_\beta \cong 2\eta_V f/(\alpha V)$, where we use that $\eta_{(dV/dt)} = \sqrt{2}\eta_V f$. Evaluating the noise propagation into the apparent heat capacity expression, we take into account the different magnitude of both noises ($\eta_\beta \gg \eta_{P_{in}}$), and we obtain

$$\eta_{C_P} \cong \frac{2\eta_V f C_P}{\alpha V \beta} \quad (3.8)$$

This expression can be rewritten introducing the signal to noise ratio ($SNR = V/\eta_V$) and the concept of temperature resolution of the measure ($\theta = \beta/f$), which depends on the combination of heating rate and acquisition frequency

$$\eta_{C_P} \cong \frac{2C_P}{\alpha(SNR)\theta} \quad (3.9)$$

In a single scan preserving a temperature resolution of 1 K (acquiring in average one experimental point every 1 K), with a standard calorimeter ($\alpha \sim 0.0026 \text{ K}^{-1}$ and $C_P \sim 0.6 \text{ } \mu\text{J/K}$ at RT), the normal noise in the heat capacity signature may range from 500 nJ/k down to 25 nJ/K for better SNRs (from 1000 to 20000). Nevertheless, most of the noise limiting the measurement is random and normally distributed, fact that opens the possibility to perform multiple scans when measuring systems with non-irreversible transitions. In this case, the SNR increases by a factor \sqrt{N} , where N is the number of consecutive measurements. Noise can be also reduced at expense of temperature resolution, θ , using data box averaging procedures [5, 8].

It has been evidenced that digital noise is the factor that ballasts the precision of the method. A traditional strategy used in instrumentation to overcome this lack of precision is to consider differential measurements. Using a couple of twin calorimetric cells working simultaneously, differential signature can be widely amplified while fitting the range of the ADC card. There is an upper bound for the improvement following this strategy, which is related with the intrinsic thermal noise of the metallic elements used as thermometer and with the pre-amplification stage. For these resistors, the spectral density of thermal noise (or Johnson-Nyquist noise) is very low and maximum values are around $2 \text{ nV Hz}^{-1/2}$, at the maximum operation temperatures. More limiting is noise produced by the electronics. The instrumentation amplifier INA111 presents a noise density at the input voltage of around $10 \text{ nV Hz}^{-1/2}$. After amplification ($\sim \times 200$) and considering the bandwidth of the measurement (500 kS/s), this noise reaches

values (~ 1 mV) over the digital noise what inevitably limits this strategy. Nevertheless, differential measurements provide an improvement in the order of the amplification factor.

Among the different implementations of the differential measurements, two main architectures can be highlighted: (i) with the nanocalorimeters feed in parallel, the Wheatstone bridge configuration (we use it for microsecond-pulsed heating nanocalorimetry), and (ii) with the nanocalorimeters feed in series achieving the differentiation with instrumentation amplifiers. Although first configuration may reach lower noise levels, it requires a more complex setup and do not guarantees that same current passes through both devices. Figure 3.6 shows a scheme of the differential setup in series used for most of the experiments along this Thesis. With this setup the differential voltage drop between two calorimetric cells $\Delta V = V_S - V_R$, one named S because host the sample and a second named R because it is used as reference, can be acquired with a large magnification ($\times 10 - \times 1000$) using the INA111 instrumentation amplifier. The difference in apparent heat capacity between both cells can be recalculated introducing the differential voltage ΔV

$$\Delta C_P^0(T(t)) = \frac{V_S^0(t)I^0(t)}{\beta_S^0(t)} - \frac{V_R^0(t)I^0(t)}{\beta_R^0(t)} = \frac{V_R^0(t)I^0(t)}{\beta_R^0(t)} \left[\frac{\beta_R^0(t)}{\beta_S^0(t)} \left(\frac{\Delta V(t)}{V_R^0(t)} + 1 \right) - 1 \right] \quad (3.10)$$

Note that for simplicity the current $V_i(t)/R_{load}$ is denoted as $I(t)$. As for non-differential analysis, the superscript 0 denotes that the measurement is done before sample deposition. Although calorimetric cell can be pre-selected, the impossibility of finding two identical cells requires always the realization of a previous measurement determining initial $\Delta C_P^0(T(t))$. This correction is also called baseline correction.

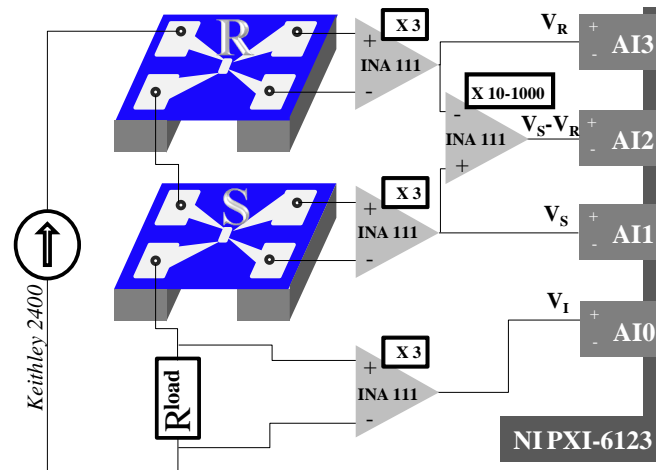


FIG. 3.6 Differential setup for quasi-adiabatic nanocalorimetry connected in series.

This expression, which was firstly derived by Allen et al. [5], is part of what they called method I for the derivation of the heat capacity. This method requires a second measurement after the inclusion of the sample on the sample calorimetric cell (SCC). Between the first and second measurement, the heating rate of the SCC may be substantially reduced due to the increment in heat capacity. Therefore for a given

temperature of the SCC, the subtraction in heat capacity is always larger in the second experiment. The heat capacity of the reference calorimetric cell (RCC), $C_{P_R}(T)$, can be determined with large precision (applying the statistics required) using the non-differential method. Knowing the relative temperature evolution between cells in both experiments, we can determine for each temperature of the SCC which was the respective temperature on the RCC, and therefore the amount of heat capacity subtracted in excess. This correction is called heating rate correction. The final expression derived from the method I, results as

$$C_{P_{A-I}}^{sample}(T_S) = \Delta C_P^1(T_S) - \Delta C_P^0(T_S) + [C_{P_R}^1(T_S) - C_{P_R}^0(T_S)] \quad (3.11)$$

Method I do not improve the precision of the non-differential method although introduces ΔV , an amplified signature. As explained in Section 3.3 *Heat capacity derivation*, the main source of noise is the heating rates ratio term. Allen and coworkers derived an approximation (called method III) [5], where assuming that ΔV is always very small, the amount of mass is almost negligible, and the nanocalorimeters are identical, the difference in heat capacity between cells can be written as

$$\Delta C_{P_{A-III}}(T(t)) = -\frac{V_R(t)}{\beta_R^2(t)(dR/dT)_t} \frac{d\Delta V}{dt} \quad (3.12)$$

From the experience, we have evidenced that this approximation provides calorimetric signatures with a very low noise, but lacks of accuracy. Figure 3.7 shows the melting of 40 nm an indium thin film, and how method I reports correct values, but with high noise levels, while method III loses accuracy. It has been probed in different systems that systematically the enthalpy is underestimated and the determination of real heat capacity depends on the equality of the heat capacity addenda and metallic element resistances. We have applied, when needed, the corrections described by Ref. [5], namely different addenda (baseline), different heat capacity of blank sample cell at different temperatures (heating rate), and heat loss. However the method III does not reproduce correctly the real heat capacity shape, even including all possible corrections.

To check it, we used a 0D model using Matlab with dumped parameters to calculate the voltage signals that would ideally generate different samples of indium (with a first order phase transition), with different thicknesses ranging from 1 to 100 nm, and we have recalculated the heat capacity with methods I and III, see Figure 3.8. With method I, the final solution reports correct values, even when heat capacity, resistance, and mass differences between CCs have been tested. Unfortunately, although method I is very accurate it is very sensitive to the voltage signatures noise. We observe the great accuracy achieved by Allen method I, while the accuracy for Allen III worsens as sample thickness increases. Note that the simulation does not include signal noise. In Section 3.3 *Heat capacity derivation*, we present a different strategy to reach same accuracy of method I and reporting the noise level of method III.

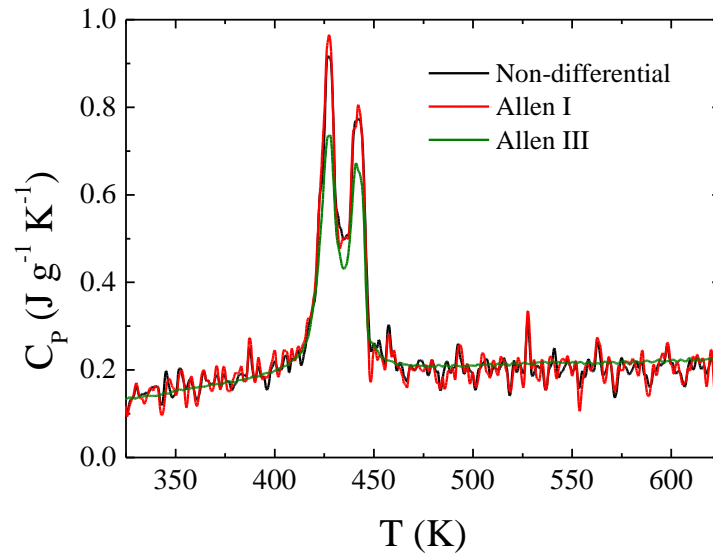


FIG. 3.7 Heat capacity of 40 nm In thin film sample. The data set is processed by three different methodologies: non-differential (black), Allen method I (red), and Allen method III (green).

The two peaks anomaly observed on experimental data, instead of one predicted by the simulation, correspond to a binomial distribution of indium spheres which has been previously reported [9, 10].

3.2.2 Microsecond-pulsed heating nanocalorimetry

Among the different calorimetric methods implemented for chip calorimetry, quasi-adiabatic nanocalorimetry reports the better sensitivity per unit area, but do not offers the possibility of measuring heat capacity at constant temperatures as a function of other variables (time, magnetic field, pressure. . .). To determine the heat capacity in quasi-static conditions there are calorimetric methods like relaxation [11] or AC-calorimetry better suited [12, 13]. Notwithstanding, the use of our nanocalorimeters in AC mode is somehow troublesome because they are equipped with a single metallic element, acting both as heater and thermometer. With this configuration, it is required to access the third harmonic component of the voltage to be able to monitor the temperature evolution during the excitation with an oscillating current. The expected signal attenuation for high order harmonics implies a lost in sensitivity that invalidates this approach. On the contrary, these calorimetric cells have been especially designed to be rapidly heated with DC currents, promoting an extraordinary enhancement of the calorimetric signature and consequently boosting the resolution of the method. Unlikely, even for more traditional designs of AC-calorimeters (with independent heater and thermometer), this enhancement of the signature linked to the fast dynamics cannot be achieved because of the necessity to preserve diffusive limits in the cell. The designs of calorimetric cells for AC-method should consider the compromise between heating and

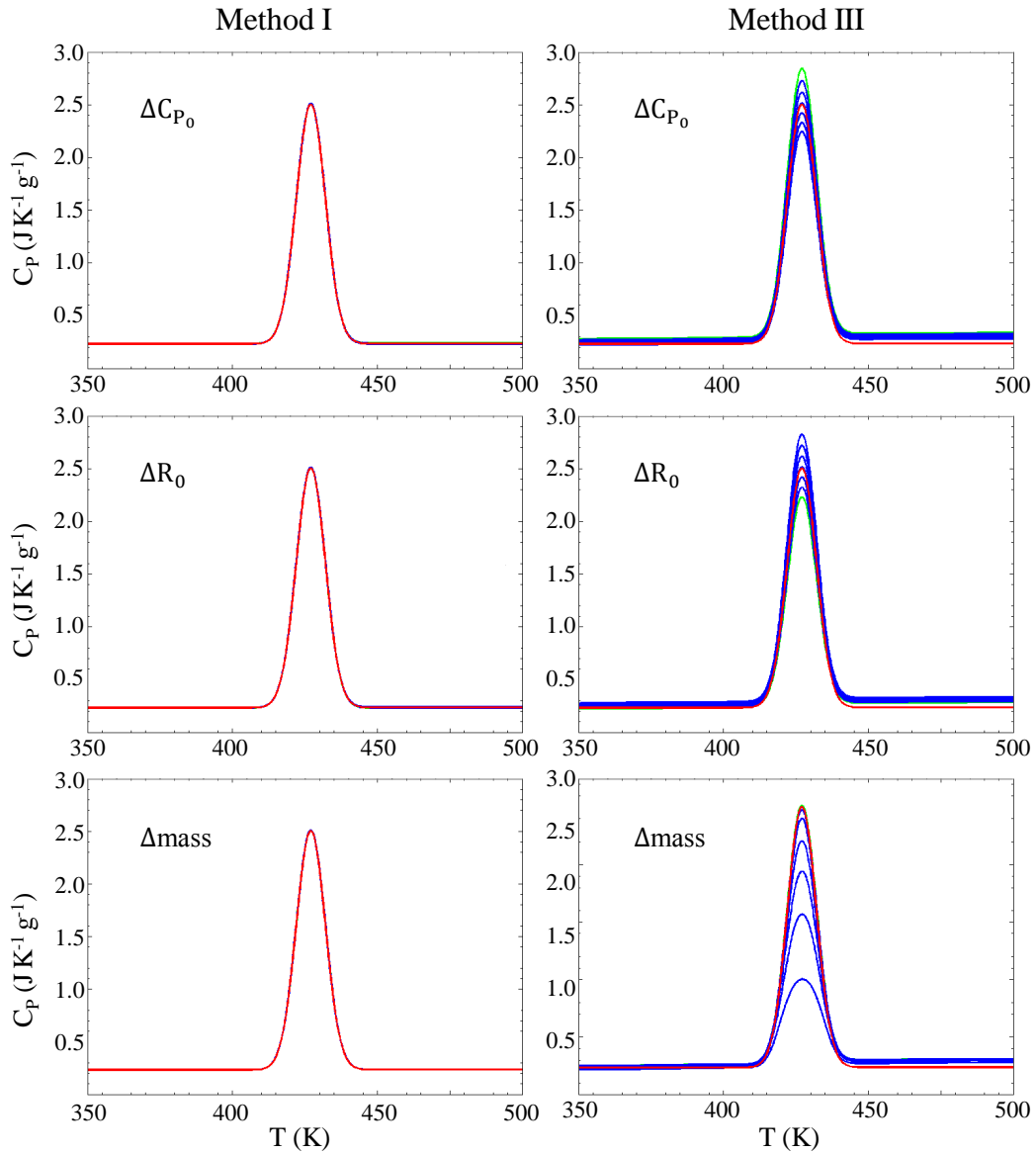


FIG. 3.8 Specific heat capacity simulation by a 0D model realized with Matlab for thin films of In heated from RT up to 500 K. Graphs on the left present the results obtained with method I, while graphs on the right present the results for method III. The different rows present the results obtained modifying initial differences on heat capacity, resistance, and mass between CCs. The differences on heat capacity and resistance for the SCC are 0.94, 0.96, 0.98, 1.00, 1.02, 1.04 and 1.06 of the RCC values ($1 \mu\text{J K}^{-1}$ and 30Ω at room temperature, respectively). In both cases sample thickness is 1 nm. The differences on mass between SCC and RCC are achieved simulating indium samples with 1, 2, 4, 10, 20, 40, and 100 nm thick (in this case, there are no differences in heat capacity or resistance between CCs). Curves show the non-differential signal (red line), and simulation results for both methods (green line corresponds to the first simulation, 0.94 and 1 nm, while blue lines shows subsequent simulations in increasing order). The 0D model does not contain noise parameters.

cooling processes.

In this Section, we present a variant of the quasi-adiabatic scanning technique where reducing the current pulse duration to μs range, the heating is promoted locally (few K) around the base temperature (temperature of the Si frame) and heat capacity can be evaluated in quasi-static conditions like in AC-calorimetry. Moreover, we demonstrate how using trains of current pulses with selected duty cycles to preserve the device base temperature (few μs on - several ms off) opens the possibility to perform multiple pulse averaging. The combination of the huge heating rates with large averaging strategies permits to reach unprecedented heat capacity resolutions below $100 \text{ pJ K}^{-1} \text{ mm}^{-2} \text{ Hz}^{-1/2}$.

Figure 3.9 shows the standard train of pulses used to operate the nanocalorimeters. Working in vacuum conditions the nanocalorimeter dynamics is marked by the low thermal mass and high CC thermal isolation. When feeding the device with current in the range of few mA, the cell rapidly heat up following very fast rates, in the kK/s range. To limit the span of the heating to temperatures of few K, the pulse width should limit to the microsecond range. Nevertheless, a train of pulses should permit the cell cooling down to frame temperature between pulses ($\tau = 150 \text{ ms}$).

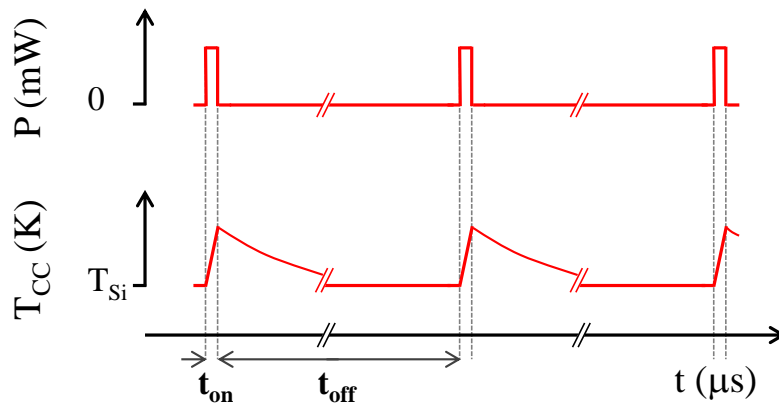


FIG. 3.9 Train of current pulses feeding the calorimeters. The timing duty-cycle between the pulses is adjusted (% time on) to guarantee the cooling down of the calorimetric cell.

The heat capacity can be obtained following the same procedure explained for quasi-adiabatic nanocalorimetry (Equation 3.12). However, evaluating the heat capacity during the early stages of the pulses presents several advantages:

- (i) The heat losses can be neglected (even working at ambient pressure). Local heating reduces extraordinarily the power released from the cells by conduction. Moreover, if the nanocalorimeter is loaded into a cryostat or a chamber where the thermostatic holder is equipped with a thermalized radiation shield, the radiation term can be also neglected. As a consequence, the total P_{losses} term

3. NANOCALORIMETRY: OPTIMIZING THE OLD, DEVELOPING THE NEW

is negligible compared with the P_{in} term required to promote the huge heating rates employed. Therefore the calculus of apparent heat capacity directly reports the real heat capacity of the cell.

- (ii) In the initial stages, the 2D temperature maps are much flatter than those presented in QAnC, where lateral diffusion degrades the temperature homogeneity in the borders of the calorimetric cells. Figure 3.10 shows the temperature 2D maps of the calorimetric cell obtained with COMSOL Multiphysics finite element modeling. For scans 10 ms long (QAnC experiments) the dispersion in temperature distribution is greater than 15 K, while for scans lasting 10 μ s (μ -PHnC experiments) the temperature distribution is below 1 K.

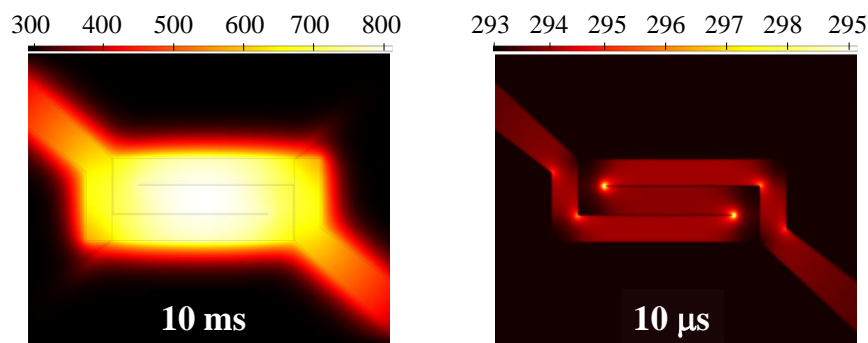


FIG. 3.10 Comparison between temperature profiles in quasi-adiabatic timings (10 ms) and μ s-pulsed timings (10 μ s).

- (iii) The small lateral diffusion achieved during short pulses minimizes the positioning requirements of the sample. During the few μ s pulse length, only the area beneath the metallic element and few microns around the perimeter is tested, as schematically shown in Figure 3.11(a). A 3D finite element model of the nanocalorimeter has permitted to test in a blank calorimeter the sensed area. For this experiment, we have removed the heat capacity temperature dependence for all materials forming the nanocalorimeter, and subsequently, we have simulated an experiment injecting a current through the metallic element. The simulation permits to measure the heat capacity sensed during the pulse as a function of time (using quasi-adiabatic approximation). The results give an idea of the amount of area detected at each time. In Figure 3.11(b), the heat capacity data has been normalized by the value of the heat capacity addenda C_{P_0} (or the sensing area heat capacity). As it can be deduced, the area sensed only grows around 2% after 10 μ s. As a consequence, we conclude that this technique is less restrictive for the positioning of the sample, and in some cases (when measuring low conductive materials) the use of the shadow mask may be omitted.
- (iv) After every pulse, the CC temperature is always reset to the base temperature. For this reason, there is no extra correction needed considering the relative change of heating rates between twin

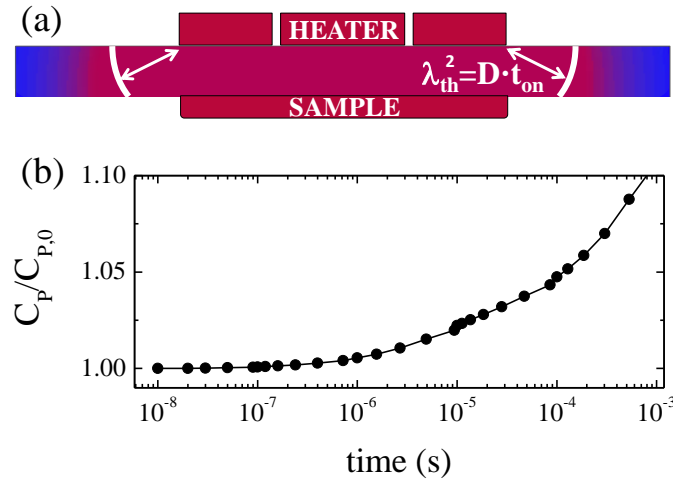


FIG. 3.11 (a) Cross section representation of the heat diffusion length in the device. (b) We can see the result of a finite element modeling of the calorimeter.

CCs when introducing the sample.

- (v) As a direct consequence of the previous point and the short span of the heating ramps, the amplification factors used in differential measurements can be extremely large.

Instrumentation and electronics

The fast dynamics of the measurements requires the development of a complete electronic setup. The setup is based in a differential Wheatstone bridge where each branch reproduces the non-differential setup used in QAnC, where a nanocalorimeter connected in series with a load resistance. The source-measure actions are achieved using a PXIe-6124, a card able to generate and acquire signals (± 10 V) at rates of 4×10^6 samples per second. Synchronization is achieved using Labview software to control all the instruments and compute the raw data acquired. The train of pulses is generated controlling the amplitude (V_{AO0}), the width (t_{on}) and the duty cycle by modifying the time between pulses (t_{off}). To debit the correct current into the bridge, the signal generated by the PXIe-6124 is boosted using an INA103 as driver amplifier (able to debit up to 65 mA). As shown in Figure 3.12, different voltage signatures are pre-amplified using also the INA103 as instrumentation amplifier, prior to the acquisition. The election of the INA103 (a bipolar instrumentation amplifier typically used for acoustic applications) is justified due to its very fast settling time (3 μ s), ultra-low input noise (1 nV $\text{Hz}^{-1/2}$ at 1 kHz), and good CMRR for large amplification factors required in the experiment. In this circuit the load resistors are selected to accommodate the output current range. Current flowing through each branch is measured by the voltage drop in the load resistors (V_{I_S} and V_{I_R}), with a 3x amplification factor. The voltages dropped in the

3. NANOCALORIMETRY: OPTIMIZING THE OLD, DEVELOPING THE NEW

reference calorimetric cell (V_R), and the differential voltage ($\Delta V = V_S - V_R$), are measured in 4-wire configuration. In order to preserve the Johnson-Nyquist noise level during the differential measurement, the first amplification stage uses a 100-fold factor (INA103 presents a minimum output noise of $65 \text{ nV Hz}^{-1/2}$).

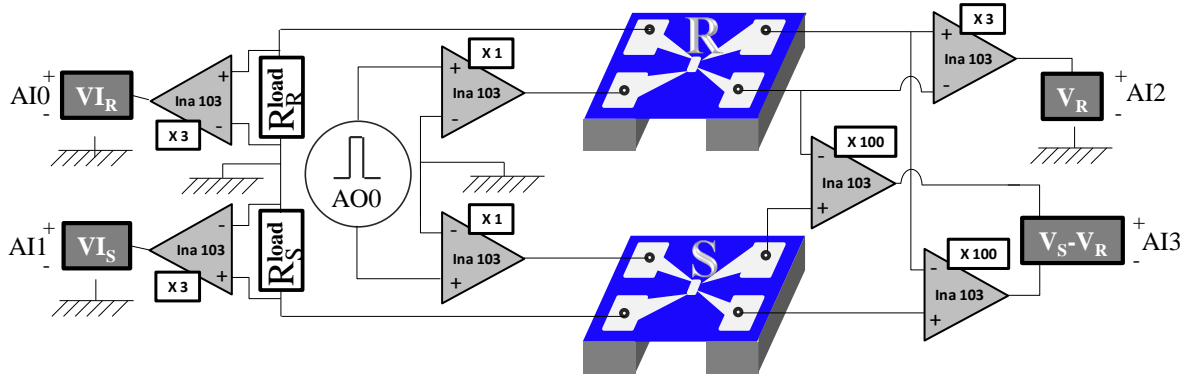


FIG. 3.12 Electronic step scheme. Bridge configuration used for low noise differential measurements. Each branch is feed by a common pulse generator (0 to 10 V) using driver amplifier for each branch (up to 65 mA). Load resistors are selected to accommodate the output current range. Current flowing through each branch is measured through the voltage drop in the load resistors (V_{I_S} and V_{I_R}) with a 3x amplification factor. The voltage dropped in sensing part of the reference calorimetric cell (V_R) and the differential voltage with the sample calorimetric cell ($V_S - V_R$) are also measured in 4-wire configuration. A 100-fold amplification factor guarantees to work in the Johnson-Nyquist noise.

To perform the experiments, the nanocalorimeters are loaded in the cryostat described in Subsection 2.2.2 *Immersion cryostat setup*. When mounted in the thermostatic probe, the temperature of the nanocalorimeters Si frame oscillates less than 1 mK around the prefixed base temperature. This temperature is also controlled by Labview software, permitting to perform either isothermal or ramp experiments. Figure 3.13(a) shows the raw data for the 4 signatures (V_{I_R} , V_{I_S} , V_R and ΔV) acquired from a single pulse experiment. The acquisition is programmed to take data before and after the pulsed experiment, allowing the offset correction for each signature. This step is crucial for the latter averaging between data arriving from different pulses. Figure 3.13(b) shows the data already transformed into temperature, and in the graph two regions are highlighted. At the beginning of the pulse, the first $5 \mu\text{s}$ are dominated by a non-linear behavior mainly motivated by the transient response of INA103 ($\sim 3 \mu\text{s}$). After the initial region, the response of the device is quite linear, and we can take profit evaluating the different variables, as the value average or the slope along this region. In this case, for the temperature, we conclude that the calorimeters have increased in average 3.185 and 3.035 K their temperature after $20 \mu\text{s}$.

One of the concerns is the temperature shift between the base temperature of the mounting holder (T_{MH}) and the starting temperature of the calorimetric cell (T_{Si}). If the nanocalorimeter is correctly attached

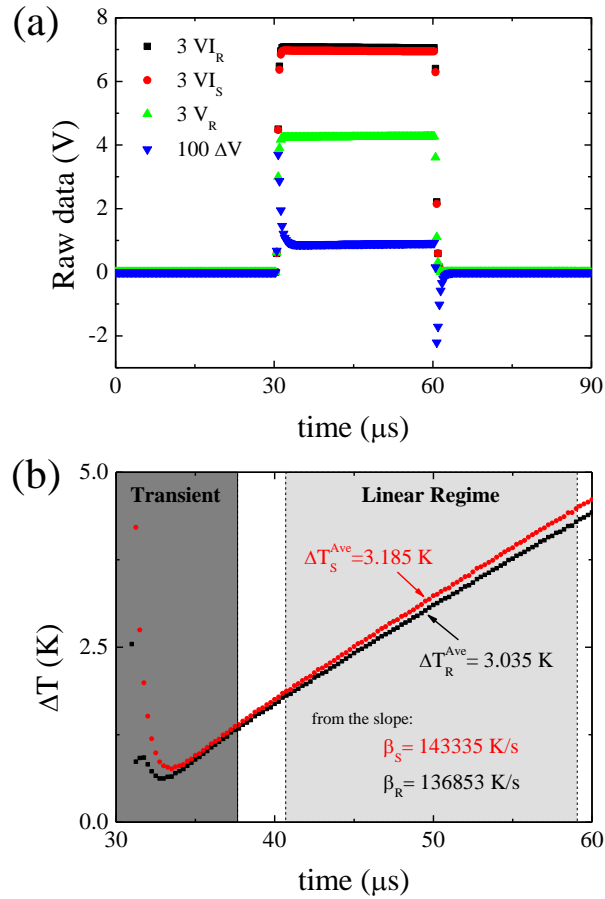


FIG. 3.13 (a) Raw data voltages acquired for a single pulse. (b) Temperature evolution of a couple of nanocalorimeters, showing transient zone and linear zone used to perform the evaluation of the variables.

to the mounting holder using a thermal paste and mechanical clamps, the temperature of the Si frame follows perfectly the one prefixed by the mounting holder. On the contrary, as shown in Figure 3.14, the calorimetric cell will experience a local heating of few K, from the starting temperature (initially the one of the Si frame). If the duty cycle is short, with cooling times much shorter than 150 ms, the average starting temperature will increase tending to a stationary shift. Figure 3.14 shows the evolution of the steady-state temperature difference between the calorimetric cell and the Si frame ($T_{CC} - T_{Si}$) as a function of the duty cycle reduction. The train of pulses had fixed amplitude of 40 mA, 30 μs of time on (t_{on}) and a variable time off (t_{off}). The measurements have been performed at different base temperatures obtaining similar behavior, which indicates that membrane thermal conductance in the measured range does not change substantially. Note that depending on the experiment, it could be interesting to reduce the duty cycle at expenses of increasing the temperature shift. The shorter the duty cycle, the higher the averaging of points per unit time, and therefore, the shorter the time of measurement.

When the feeding current amplitude is increased, the heating rate also increases, and therefore the SNR of the measure. Of course, the temperature scan is larger and the temperature map may slightly de-

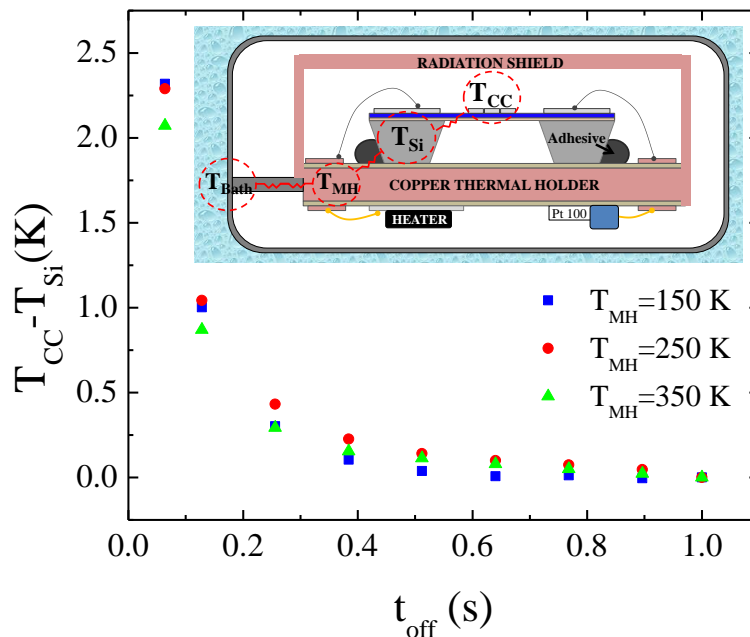


FIG. 3.14 Evolution of the steady state temperature difference between the calorimetric cell and the Si frame ($T_{\text{CC}}-T_{\text{Si}}$) as function of the duty cycle reduction, and for different mount holder temperatures. The train of pulses had fixed amplitude of 40 mA and 30 ms of time on (t_{on}) and a variable time off (t_{off}).

grade. To determine the technique limits in resolution for different currents, the heat capacity of a single calorimetric cell and the difference between a couple nanocalorimeters was carefully measured using non-differential and differential approximations. In Figure 3.15(a), we summarize the values of heat capacity noise density and the measured heating rates for both methods. To evaluate each noise density the heat capacity has been measured along periods of 50 s, and the values reported corresponds to the dispersion of this values as illustrated in Figure 3.15(b). As a meritorious number, the technique achieve a noise density of $75 \text{ pJ K}^{-1} \text{ mm}^{-2} \text{ Hz}^{-1/2}$.

To demonstrate the potentiality of the method, the so called μs -pulsed heating nanocalorimetry, we measure the order-disorder transitions in CoO thin film samples of 5 and 20 nm thick. In this Section we use these samples as case study to test the technique, the deposition method used to grow the samples and physics underlying this type of materials can be found in Chapter 4. These types of continuous phase transitions, without enthalpy release, are the ideal case where the technique can be employed. Prior to the sample deposition, like in the case of quasi-adiabatic nanocalorimetry, the initial heat capacity difference between cells was measured using both the non-differential and the differential approximations. The heat capacity was measured every 0.5 K from 150 to 380 K, averaging 1 s per temperature point. Figure 3.16 shows the heat capacity for each calorimetric cell obtained from the non-differential analysis of the raw data. From this data we can evidence the reproducibility of the results. One of the main drawbacks of this technique, when compared with QAnC, is the experiment time consumption. The large time required for

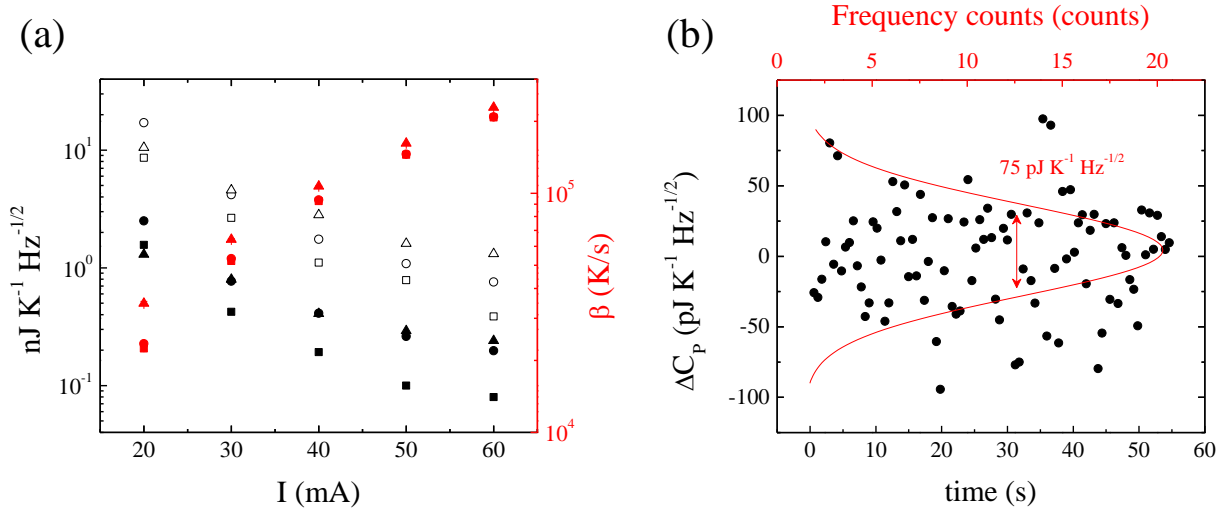


FIG. 3.15 (a) Evolution of the noise density in heat capacity data as function of current supplying the nanocalorimeters, for three different temperatures: 150 K (squares), 250 K (circles), and 350 K (triangles). Empty and solid symbols correspond to non-differential and differential methods, respectively. (b) Fluctuations around the mean value of the difference in heat capacity between twin nanocalorimeters measured at 150 K, as a function of time. The dispersion of the data determines the noise of the measurement.

μ s-pulsed heating nanocalorimetry make it very sensitive to the deposition of water or other contaminants during the experiment. In this sense, the presence of water justifies the small difference observed at high temperatures in the heat capacity of the RCCs (red and blue lines). Of course, the solution relies in the quality of the vacuum chamber used as a cryostat and the level of base pressure reached.

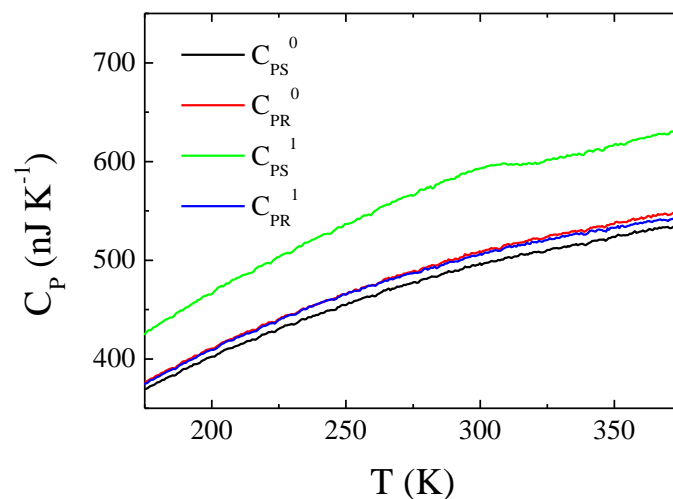


FIG. 3.16 Non-differential measurement of heat capacity data showing sample (S) and reference (R) calorimetric cells, before (0) and after (1) of 20 nm CoO thin film.

The extraordinary resolution of the technique is better appreciated in Figure 3.17, where the heat capacity of a couple of CoO thin film samples with 5 and 20 nm thick is shown using the differential

expression. Comparing the heat capacity signature obtained from this method with the quasi-adiabatic measurements presented in Chapter 4, we conclude that the rounding of the transition is smaller since the temperature homogeneity is better (Figure 3.18). With this technique we can separate the rounding effect present in the lambda transition due to the samples finite size effect, and the rounding promoted by the temperatures gradient in the 2D map of the calorimetric cell. The improvement in temperature homogeneity also induces an improvement in resolution that permits to appreciate calorimetric features non-detected previously. Besides, the transition peak appearing at 260 and 295 K, for the 5 and 20 nm samples respectively, a previous transition peak appears at 180 K. The later may be due to the water sublimation that in vacuum occurs around these temperatures.

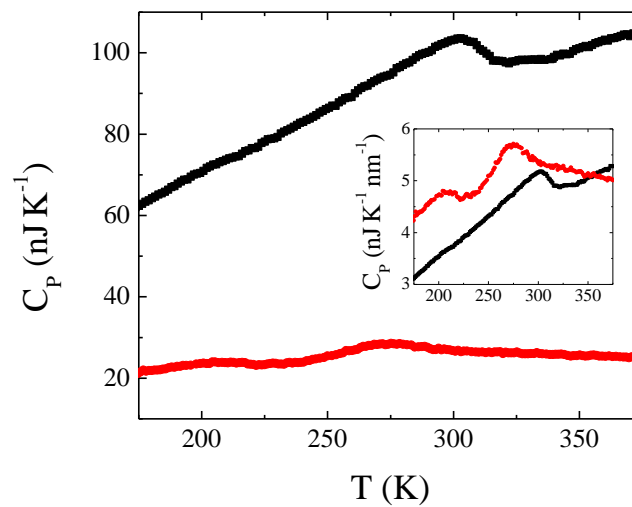


FIG. 3.17 Differential measurement after baseline correction of heat capacity data for 20 nm CoO thin film (black squares), and for 5 nm CoO thin film (red circles). The inset shows the heat capacity as function of temperature normalized by thickness.

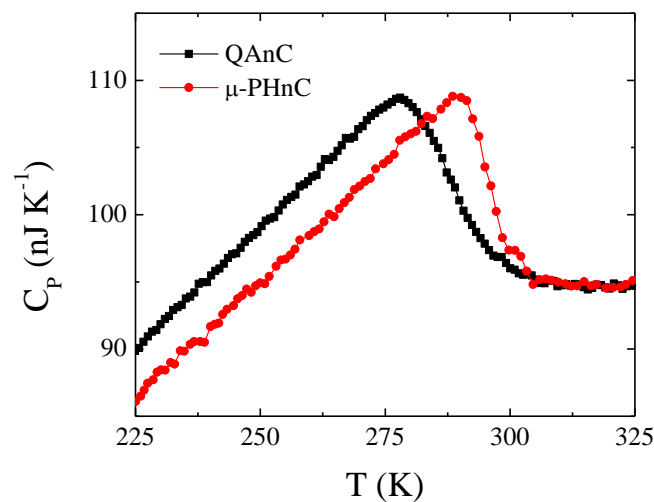


FIG. 3.18 Heat capacity of the same sample, 20 nm CoO, measured by QAnC (black squares), and μ -PHnC (red circles).

3.2.3 Power compensated nanocalorimetry

For heating rates in the range from 0.1 to 1000 K/s, the best technique is the so called power compensated scanning nanocalorimetry (PCnC), and has been already tested in several systems [6, 14]. While the fastest heating rate is limited by the Mythen detector due to the low amount of mass available for X-ray scattering, the lowest heating rate is determined by the sensitivity of the nanocalorimetric technique. It is important to note that, the lower the heating rate is, the lower the resolution of the calorimetric signal. Power compensation scanning nanocalorimetry consists on feeding a device with a DC current which value is recalculated by means of a proportional and integral (PI) controller to follow a prefixed heating ramp.

The implementation of the PI temperature controller combines a high resolution sourcemeter (Keithley 2400 source/measure unit), used to generate the current and to measure the voltage drop in the calorimetric cell, and the PC-based program (developed in Labview) with the PI algorithm to govern the source actions via GPIB communication protocol. The algorithm includes a feed forward stage in parallel to the feed-back loop. The schematic of the power compensation controller algorithm is shown in Figure 3.19. The feed forward stage evaluates a priori the gross action based on a simple model of the nanocalorimeter. Since the characteristic thermal response of the calorimeter is very fast, thus, we use a steady-state model with lumped parameters which considers a calorimetric cell, at a temperature T , linked through the silicon nitride membrane (working in high vacuum), with a thermal conductance K_L , to the silicon frame, at a temperature T_0 . Measuring the temperature rise for different input powers with empty devices, K_L can be evaluated as the slope of the plot, obtaining linear behaviours while temperature differences are kept small. In general, K_L is considered as a polynomial function of temperature, permitting to account also for radiation losses. In the experiments presented here, the set point temperatures are fixed to evolve linearly defining ramps of constant heating rates. As most of the action is taken in advance by the feed forward stage, the feedback controller only corrects small deviations from the set point values (what is called error, ϵ) promoted by the presence of the sample. A selection of the feedback control action proportional to the error ($K_P \epsilon(t)$), called P term from proportional, added to a term proportional to the accumulated error ($K_I \int \epsilon(t) dt$), called I term from integral, suffices to correct this small deviations.

For calorimetric measurements the subtraction of the background power results mandatory. It can be done either acquiring reference signature from a previous calibration measurement, or in case of analysing non-reversible transformations, using subsequent scans as reference measurement. The GPIB bus communication limits the minimum loop time to 150 ms. Every loop time; we can evaluate the power injected and temperature of the calorimetric cell from the measurements of current sourced and voltage measured.

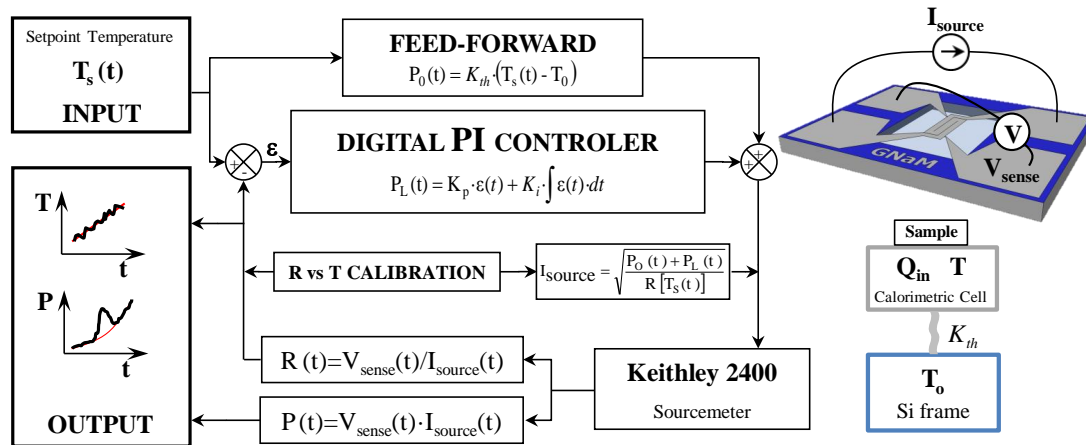


FIG. 3.19 Schematic of the power compensation controller algorithm.

Working in the better resolution range of the source, we have a noise floor of $25 \text{ nW Hz}^{-1/2}$ (peak-to-peak). In steady-state conditions, like those used for the measurements presented here (see Chapter 5), a careful estimation of power losses is required to obtain accurate heat capacity data. Nevertheless, the silicide formation has a great impact on the thermal resistance of the CCs and hence, heat loss corrections by subtraction of the second scan are not straightforward. For this reason we only provide an apparent value of the heat capacity.

Saw-tooth scanning nanocalorimetry

During this work, it has been necessary to realize measurements in the intermediate heating rate regime, from 10 to 10^4 K/s , like those employed in Chapter 5 to measure the silicide formation of Pd_2Si system. In some situations, when the amount of sample is small, the continuous corrections of the control may hide the transformation. For this reason, to measure the silicides formation (on the thinnest samples), we suppress the power control to work on the SMU noise limit. The heating is achieved by means of previously calculated current-time profiles [Figure 3.20 grey curve], instead of constant current pulses as in the case of QAnC. Then the quasi-linear increase in temperature [Figure 3.20 red curve] is achieved using saw-tooth nanocalorimetry (STnC), a simplification of the power compensated scanning nanocalorimetry [6]. In this range, heat losses are important, and we only access an apparent heat capacity.

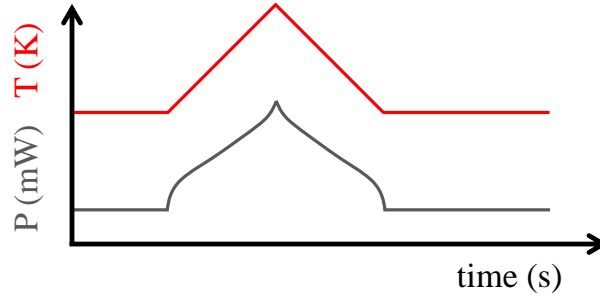


FIG. 3.20 Representation of power (grey) and temperature (red) profiles for STnC.

3.3 Heat capacity derivation

In this Section we analyze the expression for the heat capacity in differential configuration (Equation 3.13) with the aim to identify which terms cause accuracy loose and noise reduction. If we recover Equation 3.5 and we write it using a differential configuration, supposing adiabatic conditions we obtain

$$\Delta C_P(T_S(t)) = \frac{P_S}{\beta_S} - \frac{P_R}{\beta_R} \quad (3.13)$$

The subscript S denotes the sample device, and the subscript R denotes the device that is used as reference. It is important to note that the differential heat capacity between both devices, $\Delta C_P(T_S(t))$, is a sample temperature function, which in turn is a time function. For convenience this dependence is not shown explicitly. We operate the Equation 3.13 using the relation $P_i = V_i I_i$, then we can write

$$\Delta C_P = \frac{V_S I_S}{\beta_S} - \frac{V_R I_R}{\beta_R} = \frac{I_R V_R}{\beta_R} \left(\frac{V_S I_S \beta_R}{V_R I_R \beta_S} - 1 \right) \quad (3.14)$$

We use the differential configuration relation, $V_S = \Delta V + V_R$, to obtain

$$\Delta C_P = \frac{I_R V_R}{\beta_R} \left[\frac{(\Delta V + V_R) I_S \beta_R}{V_R I_R \beta_S} - 1 \right] = \frac{I_S \Delta V}{\beta_S} + \frac{V_R I_S}{\beta_S} \left(1 - \frac{I_R \beta_S}{I_S \beta_R} \right) \quad (3.15)$$

In Equation 3.15, the noisiest term is the heating rates ratio (β_S/β_R). Both signatures are calculated as the derivative of a digitized data in time, and noise of original data (η_V) is extraordinarily enhanced by the large acquisition frequency ($\eta_\beta \sim \sqrt{2}\eta_V f$). When evaluating through noise propagation the contribution of each term to the final noise, we evidenced that the denominator only contributes as η_β/β^2 , which is negligible compared with the numerator contribution η_β . Therefore, our purpose is to remove the heating rate from the numerator. As in the development of Efremov et al. [5], we spread the expression for $d\Delta V/dt$.

$$\Delta V = V_S - V_R \rightarrow \frac{d\Delta V}{dt} = \frac{dV_S}{dt} - \frac{dV_R}{dt} = \frac{dV_S}{dT_S} \frac{dT_S}{dt} - \frac{dV_R}{dT_R} \frac{dT_R}{dt} \quad (3.16)$$

3. NANOCALORIMETRY: OPTIMIZING THE OLD, DEVELOPING THE NEW

If functions $V_i(t)$ and $T_i(t)$ are derivative and continuous, then $\frac{dV}{dt} = \frac{dV}{dT} \frac{dT}{dt}$. Using this relation on Equation 3.16 and by reordering we can write

$$\frac{dV}{dt} = \frac{dV_S}{dT_S} \beta_S - \frac{dV_R}{dT_S} \beta_R \rightarrow \frac{\beta_S}{\beta_R} = \frac{(d\Delta V/dt)_t}{\beta_R (dV_S/dT_S)_t} + \frac{(dV_R/dT_R)_t}{(dV_S/dT_S)_t} \quad (3.17)$$

We used the data obtained from measuring indium thin films, since it is a well-known system, to test the signal noise obtained in both sides of Equation 3.17, the direct calculation of β_S/β_R term, and its algebraic manipulation as function of $d\Delta V/dt$ (Figure 3.21).

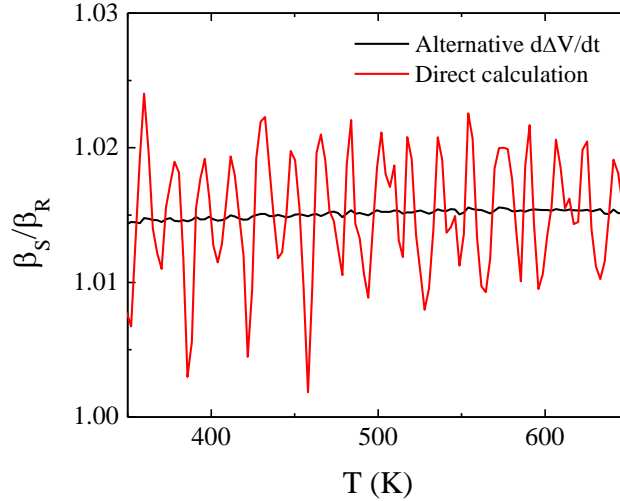


FIG. 3.21 Plot of β_S/β_R term respect to temperature, directly evaluated from the heating rates ratio (red), and evaluated from the alternative form as a $d\Delta V/dt$ function (black).

By substituting the result obtained in 3.17 in Equation 3.15, we obtain

$$\Delta C_P(T_S(t)) = \frac{I_S \Delta V}{\beta_S} + \frac{V_R I_S}{\beta_S} \left[1 - \frac{I_R}{I_S} \left(\frac{(d\Delta V/dt)_t}{\beta_R (dV_S/dT_S)_t} + \frac{(dV_R/dT_R)_t}{(dV_S/dT_S)_t} \right) \right] \quad (3.18)$$

Equation 3.18 is the general expression for $\Delta C_P(T_S(t))$ on differential configuration, and it can be expressed as the sum of three terms

$$\Delta C_P(T_S(t)) = P_1 \Delta V - P_2 \left(\frac{d\Delta V}{dt} \right)_t + P_3 \left[1 - \frac{I_R}{I_S} \left(\frac{(dV_R/dT_R)_t}{(dV_S/dT_S)_t} \right) \right] \quad (3.19)$$

where $P_1 = I_S/\beta_S$, $P_2 = V_R I_R / [\beta_S \beta_R (dV_S/dT_S)_t]$, and $P_3 = V_R I_S / \beta_S$. These P_i factors can be replaced by polynomial fittings with the aim to reduce even more the signal noise. It is possible when these factors are low frequency signals or behave monotonically. This procedure is very powerful especially when low amounts of mass, or energy variations, are measured. Figure 3.22 shows the contribution of the three different terms to the heat capacity for the 40 nm indium sample previously presented. In fact, term 2 is quite similar to the expression obtained by Allen and coworkers on his method III. The accuracy loose in this method, especially when the mass difference increases, is due to the lack of terms 1 and 3.

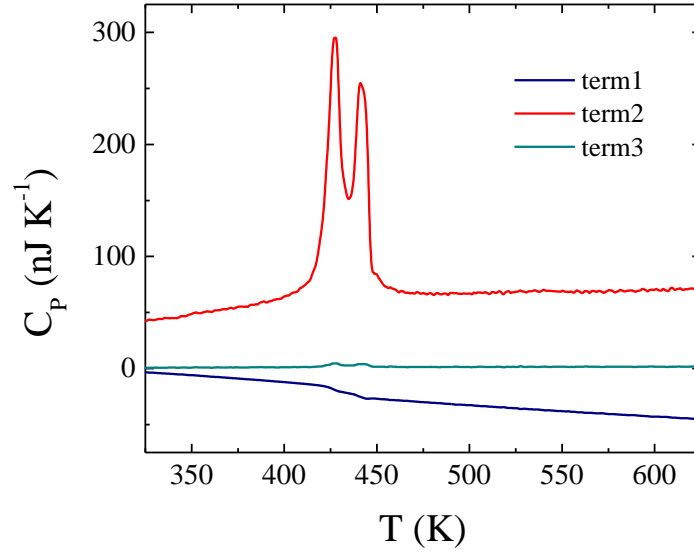


FIG. 3.22 Heat capacity of 40 nm of indium, decomposed in the three terms obtained from GNaM methodology.

Some simplifications may be applied to the heat capacity general expression:

1. If currents I_i are time independent, then $V_i = I_i R_i \rightarrow d(V_i) = d(I_i R_i) = I_i d(R_i)$ and Equation 3.18 can be written as

$$\Delta C_P(T_S(t)) = \frac{I_S \Delta V}{\beta_S} - \frac{V_R}{\beta_S \beta_R} \frac{I_R}{I_S} \frac{(d\Delta V/dt)_t}{(dR_S/dT_S)_t} + \frac{V_R I_S}{\beta_S} \left[1 - \left(\frac{I_R}{I_S} \right)^2 \frac{(dR_R/dT_R)_t}{(dR_S/dT_S)_t} \right] \quad (3.20)$$

2. If devices are fed with the same (and time independent) current, we can write $I_S = I_R = I$, then Equation 3.20 is reduced to

$$\Delta C_P(T_S(t)) = \frac{I \Delta V}{\beta_S} - \frac{V_R}{\beta_S \beta_R} \frac{(d\Delta V/dt)_t}{(dR_S/dT_S)_t} + \frac{V_R I}{\beta_S} \left[1 - \frac{(dR_R/dT_R)_t}{(dR_S/dT_S)_t} \right] \quad (3.21)$$

Regarding Figure 3.7, we used the same data set and applied the Equation 3.20 to derivate the heat capacity (Figure 3.23). In this case we observe that our methodology reproduces the heat capacity real value given by the non-differential and Allen I calculations, and interestingly, signal noise has been reduced to the same level than given by Allen III expression.

We have tested our methodology, using the necessary corrections, to measure and study the melting of indium thin films through their heat capacity (Figure 3.24). The methodology development, removing the noisiest terms with no algebraic approximation, allows us to measure thick films with high accuracy and with very low noise on the obtained results. The two peaks observed correspond to a shape distribution of nanoparticles, which form due to dewetting during indium melting (Figure 3.24 inset). We observe that once the dewetting occurs, from 2 nm thick, the thin film does not form completely until it reaches

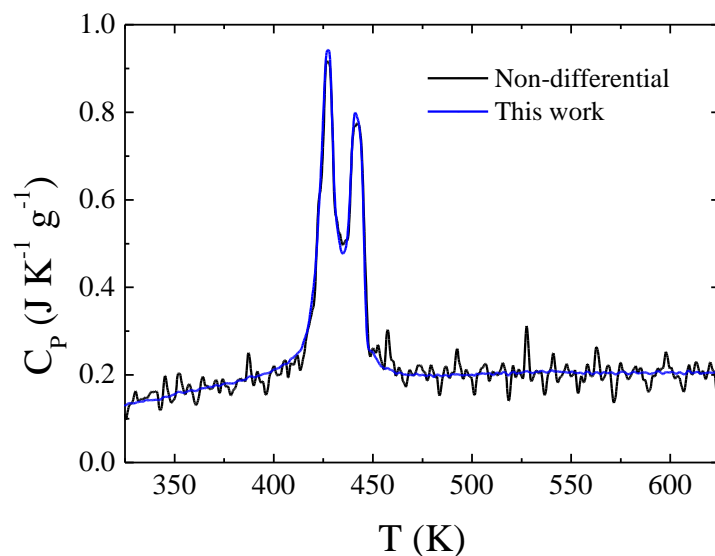


FIG. 3.23 Heat capacity curves, for 40 nm indium sample, derived using two different methodologies: non-differential (black line - Equation 3.4) and the derived in this work (blue line - Equation 3.21).

100 nm thick.

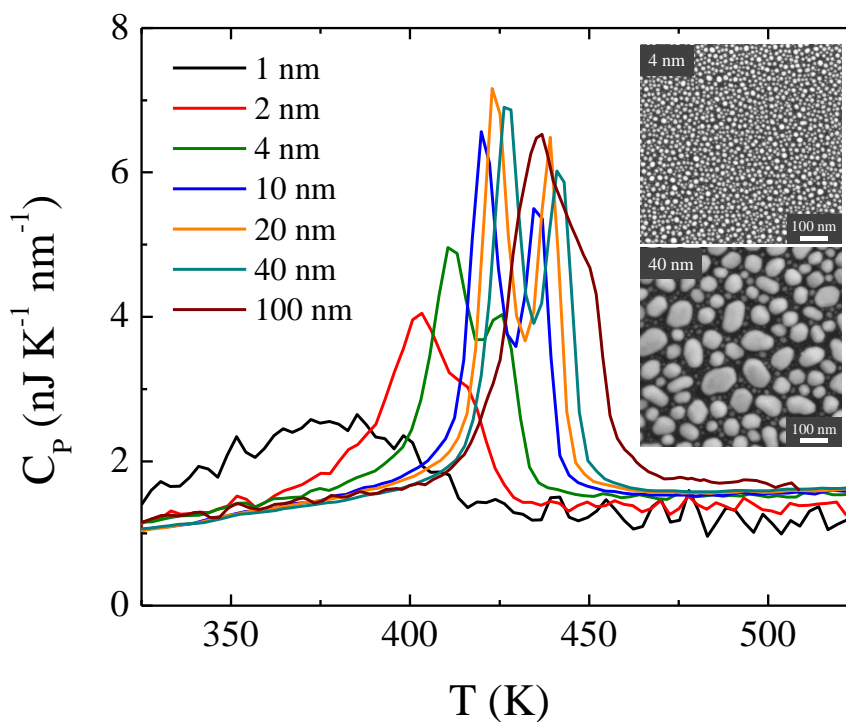


FIG. 3.24 Heat capacity curves normalized by the sample nominal thickness, from 1 to 100 nm. The inset shows two FESEM images that correspond to samples with 4 and 40 nm nominal thickness.

3.4 Conclusions

We have optimized the already existing quasi-adiabatic and power compensated nanocalorimetric techniques, introducing new electronic configuration in order to increase the dynamic heating rates range, from 0.1 to 10^5 K/s. Consequently, resolution levels below $1 \text{ nJ K}^{-1} \text{ mm}^{-2}$, for quasi-adiabatic nanocalorimetry have been attained.

We have also developed a new technique, the microsecond-pulsed heating nanocalorimetry. This technique allows uncommon measurements in quasi-isothermal conditions by promoting local heatings up to 10^6 K/s using DC pulses. The exceptional high resolution achieved, around $75 \text{ pJ K}^{-1} \text{ mm}^{-2} \text{ Hz}^{-1/2}$, permits to measure second-order phase transitions with huge sensitivity, and thermal gradients below 1 K.

In parallel new data treatment has been introduced improving the signal-to-noise ratio and accuracy compared to previous models for heat capacity analysis.

References

- [1] P. Debye. Zur Theorie der spezifischen Wärmen. *Annalen der Physik*, 344(14):789–839, 1912.
- [2] M. Y. Efremov, J. T. Warren, and E. A. Olson. Thin-film differential scanning calorimetry: a new probe for assignment of the glass transition of ultrathin polymer films. *Macromolecules*, 35(5):1–3, 2002.
- [3] A. F. Lopeandia, J. Rodriguez-Viejo, M. Chacon, M. T. Clavaguera-Mora, and F. J. Muñoz. Heat transfer in symmetric U-shaped microreactors for thin film calorimetry. *Journal of Micromechanics and Microengineering*, 16(5):965–971, May 2006.
- [4] A. G. Worthing. Atomic heats of tungsten and of carbon at incandescent temperatures. *Physical Review*, 12(3):199–225, 1918.
- [5] M. Y. Efremov, E. A. Olson, M. Zhang, S. L. Lai, F. Schiettekatte, Z. S. Zhang, and L. H. Allen. Thin-film differential scanning nanocalorimetry: heat capacity analysis. *Thermochimica Acta*, 412:13–23, 2004.

References

- [6] A. F. Lopeandia, J. Valenzuela, and J. Rodríguez-Viejo. Power compensated thin film calorimetry at fast heating rates. *Sensors and Actuators A*, 143(2):256–264, 2008.
- [7] M. Y. Efremov, E. A. Olson, M. Zhang, F. Schiettekatte, Z. Zhang, and L. H. Allen. Ultrasensitive, fast, thin-film differential scanning calorimeter. *Review of Scientific Instruments*, 75(1):179, 2004.
- [8] A. F. Lopeandia. *Development of Membrane-based Calorimeters to Measure Phase Transitions at the Nanoscale*. PhD thesis, Universitat Autònoma de Barcelona, February 2007.
- [9] M. Zhang, M. Efremov, F. Schiettekatte, E. Olson, A. Kwan, S. Lai, T. Wisleder, J. Greene, and L. Allen. Size-dependent melting point depression of nanostructures: Nanocalorimetric measurements. *Physical Review B*, 62(15):10548–10557, October 2000.
- [10] M. Y. Efremov, F. Schiettekatte, M. Zhang, E. A. Olson, A. T. Kwan, R. S. Berry, and L. H. Allen. Discrete periodic melting point observations for nanostructure ensembles. *Physical Review Letters*, 85(17):3560–3563, 2000.
- [11] D. W. Denlinger, E. N. Abarra, K. Allen, P. W. Rooney, M. T. Messer, S. K. Watson, and F. Hellman. Thin film microcalorimeter for heat capacity measurements. *Review of Scientific Instruments*, 65(4):946–959, 1994.
- [12] F. Fominaya, T. Fournier, P. Gandit, and J. Chaussy. Nanocalorimeter for high resolution measurements of low temperature heat capacities of thin films and single crystals. *Review of Scientific Instruments*, 68(11):4191, 1997.
- [13] F. R. Ong and O. Bourgeois. Topology effects on the heat capacity of mesoscopic superconducting disks. *Europhysics Letters*, 79(6):67003, 2007.
- [14] A. F. Lopeandia, L. L. Cerdo, M. T. Clavaguera-Mora, L. R. Arana, K. F. Jensen, F. J. Munoz, and J. Rodríguez-Viejo. Sensitive power compensated scanning calorimeter for analysis of phase transformations in small samples. *Review of Scientific Instruments*, 76(6):065104, 2005.

4. Antiferromagnetic interaction in CoO

Part of this Chapter appears published in *Physical Review B* **83** 140407(R) (2011).

In Chapter 3 we have introduced how thermodynamics relate microscopic properties, as the energy of the matter atoms, with macroscopic ones, such as temperature. In this Chapter, we analyze magnetic transitions using a thermodynamic perspective. We show how thermodynamics and magnetism, which is based on quantum interactions, are related through a macroscopic property: the heat capacity.

We present an exhaustive analysis of the heat capacity of CoO ultrathin films, and its phase transition from antiferromagnetic (AFM) to paramagnetic (PM) states. The magnetic transition is analyzed from nanocalorimetric curves obtained from samples grown in a variety of experimental conditions to modify its thickness and microstructure. The study is completed through the microstructural and magnetic characterization of samples by X-ray diffraction (XRD), transmission electron microscopy, in both planar and cross sectional observations (TEM and XTEM, respectively), and semiconductor quantum interferometer device (SQUID) magnetometry. The magnetic transition is analyzed by quasi-adiabatic nanocalorimetry (QAnC, see Subsection 3.2.1 *Quasi-adiabatic nanocalorimetry*) at heating rates about 6×10^4 K/s.

The Chapter also includes the use of the Debye model to fit the heat capacity curves. From this model we analyze the Debye temperature (T_D), and indirectly the Néel temperature (T_N) and the magnetic energy, which are related to the magnetic interaction. These parameters are directly affected by the microstructure of the samples.

4.1 Introduction

The history of magnetism and magnetic materials began thousands of years ago in the ancient Chinese civilization, where the first mentions of magnetic phenomena in iron oxides based minerals, called lodestones, were reported by Guanzhong (died 645 BC). Magnetic attraction was the first phenomenon to draw the attention of man to lodestone. Several years later, in Greece, Aristotle reported that Thales of Miletus (625 BC) also knew about lodestones and its “magical” properties. However, it was Onomacritus who baptized for the first time one of the most famous magnetic minerals, the Fe_3O_4 , as magnetes. The name arises because its abundance in the Greek prefecture of Magnesia. This is the most ancient name known which evolved into the modern term magnetite and also the name for the physical phenomena: magnetism. During centuries the main technological application was the compass, and no serious theories were performed, as noted Denis Dideron and Jean Lerond d’Alembert in their Encyclopaedia. At that time the knowledge of magnetism was summarized under three entries: magnetic poles, attraction, and transmission of magnetism. The Encyclopaedists had to face the fact that all attempts at interpreting magnetism (including the efforts of the mathematician Bernoulli) were unsuccessful. We would need to wait until the 19th century to observe a clear advance on the theories about magnetism, due to a series of great contributions: Charles-Augustin de Coulomb demonstrated his famous $1/r^2$ interaction law between electric charges, Denis Poisson introduced the notion of a magnetic field, H. C. Oersted showed that a magnetic field could be created by the circulation of an electric current in a conducting wire, André-Marie Ampère repeated this historic experiment, and succeeded in giving it an elegant formulation, Michael Faraday discovered the phenomenon of induction and developed the first dynamo, and James Clerk Maxwell in 1864 crowned the efforts of half a century with the laws of the electromagnetism, which remain today in the analytical basis of magnetism. It was close to the beginning of the 20th century where we could find the first serious works on describing the magnetism in magnetic materials. From the classical point of view, the work of Pierre Curie clarified some ideas on diamagnetism, paramagnetism and ferromagnetism [1], Paul Langevin established the statistical theory of paramagnetism [2] and Pierre Weiss the molecular field theory [3].

The necessity for giant molecular field to explain the magnetism in several substances evidenced the limitations of the theory. At this stage, in 1927, the quantum mechanics made a fundamental contribution to magnetism with the discovery by Paul Dirac of the intrinsic angular momentum of the electron, called spin [4]. After that, in 1929, Werner Heisenberg showed the electrostatic origin of the magnetic interactions responsible of the magnetic order, and how it could be interpreted in terms of coupling between two neighboring spins [5]. With the exchange theory the huge magnetic field created in most ferromag-

4. ANTIFERROMAGNETIC INTERACTION IN CoO

netic materials was perfectly explained. It was in 1936 when Louis Néel established the model for a new kind of magnetic behavior, the antiferromagnetism [6]. Several years later, in 1948, he published a paper entitled *Les propriétés magnétiques des ferrites: ferrimagnétisme et antiferromagnétisme* [7], where he generalized his theory of antiferromagnetic materials supposing that the two magnetic sublattices, which compose it, have unequal magnetic moments (\vec{m}). His theory predicted a novel behavior, the ferrimagnetism, where the spins are aligned antiparallel in a system composed by two lattices with different magnetic moment every one, which produces a nonzero magnetization. In fact, antiferromagnetism is a particular case of ferrimagnetism where both lattices have the same magnetic moment. During last 50 years, a large number of engineering applications using antiferromagnets have been developed.

Matter can be classified depending on the magnetic nature of their atoms (if they show a net magnetic moment, \vec{M} , or not) and how this magnetic moment interact between them. The first group contains the substances constituted of atoms that do not present a permanent \vec{M} , the diamagnetic substances. In the presence of an external magnetic field, those substances react creating a very weak and permanent magnetization in the opposite direction of the applied magnetic field, while the second group includes all the substances with permanent \vec{M} in the atoms or in the molecules that form them. In fact, the substances belonging to the second group, shows both diamagnetic and magnetic behaviors. From these magnetic materials we can identify paramagnetism [Figure 4.1(a)], ferromagnetism [Figure 4.1(b)], ferrimagnetism [Figure 4.1(c)] and antiferromagnetism [Figure 4.1(d)] among other types.

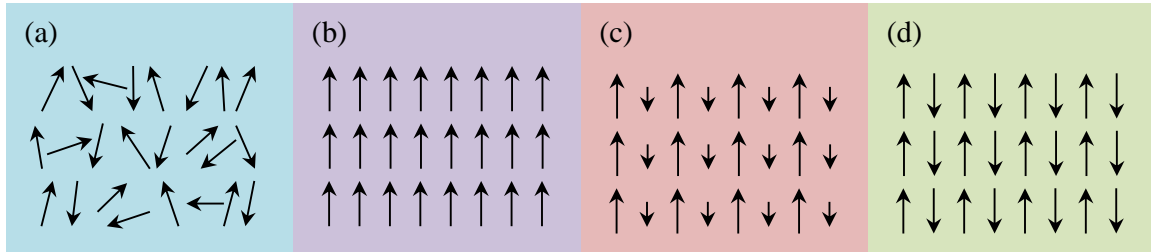


FIG. 4.1 Different types of magnetism: (a) paramagnetism, (b) ferromagnetism, (c) ferrimagnetism, and (d) antiferromagnetism.

The magnetism in matter is originated by the orbital motion of electrons rotating around the nuclei or by its intrinsic spin. The orbital magnetic moment of the electron is proportional to its orbital angular momentum. In atoms, for each electron with angular quantum number $+\ell$ there is another with $-\ell$, cancelling its action. Thus the net result is that, for most materials, the magnetic effect produced by the orbital motion of the electrons is either zero or very small. Very different is the case of the spin contribution. Considering the Pauli Exclusion Principle (i.e. the electrons behave as fermions) and the Hund's Rule for filling the electronic orbitals in an atom, it is found for a given atomic number (Z) that unbalanced spins will result on a net magnetic moment. This is the case for iron, cobalt, nickel,

gadolinium and dysprosium, the only five pure elements showing ferromagnetic behavior. In Figure 4.2, a schematic of the electronic structure of cobalt is shown, where 3 electron spins of the d orbital (in red) interact giving a non-zero magnetic moment.

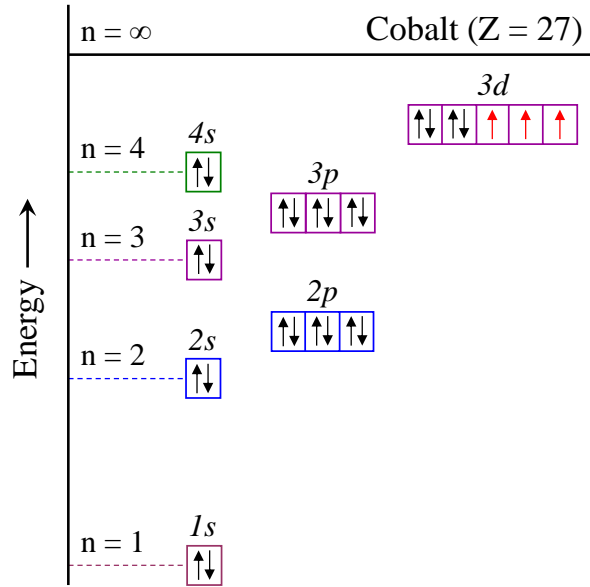


FIG. 4.2 Cobalt electronic structure scheme.

This interaction is given by the coupling between neighboring spins. Heisenberg defined this interaction as the exchange integral (J) written in Equation 4.1, where J is the sum over all pairs i, j of an interaction term.

$$J(i, j) = \iint \psi_i^*(r_1)\psi_j^*(r_2)\frac{1}{r_{12}}\psi_i(r_2)\psi_j(r_1)dr_1dr_2 \quad (4.1)$$

Experimentally, the value of the exchange integral J depends strongly on the crystalline structure (distance between atoms) and the electrostatic interaction between the orbitals. Bethe and Slater found the empirical curve where the value of J is plotted as a function of the ratio between the atomic (a) and the 3d shell radii (r) for different elements on the periodic table (Figure 4.3).

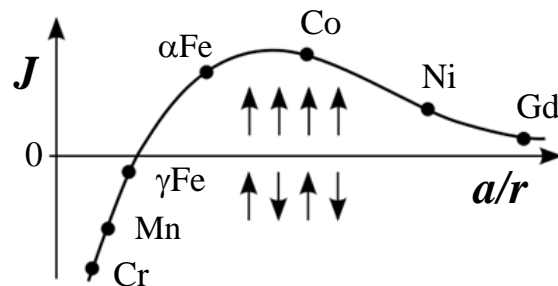


FIG. 4.3 Bethe-Slater curve where the x-axis gives the ratio of radius of atom a to the radius of 3d shell of electron r . The elements with positive J shows ferromagnetic nature such as Fe, Co and Ni and elements with negative J show antiferromagnetic nature.

4. ANTIFERROMAGNETIC INTERACTION IN CoO

When $J > 0$ indicates a ferromagnetic interaction and the magnetic moments of the atoms or molecules are aligned in regular patterns with neighboring spins pointing on the same direction. Otherwise, when $J < 0$ the exchange interaction tends to anti-align neighboring spins. In antiferromagnetic materials, the magnetic moments of atoms or molecules, are aligned in a regular pattern with neighboring spins (on different sublattices) pointing in opposite directions. As shows in Figure 4.1(d), antiferromagnetism is a particular case of ferrimagnetism [Figure 4.1(c)], where the magnetic moments of the two sublattices are equal, and thus the cancelation of the magnetization is completed.

Typically, magnetic materials are characterized by magnetometry. Nevertheless, these experimental measurements on antiferromagnets are very complicated due to the weakness of their magnetic signal ($\vec{M} \approx 0$). Antiferromagnetic materials may exhibit ferromagnetic behavior when an external field is applied. This phenomenon occurs when the magnetization absolute value in one sublattice differs from that other, resulting in a non-zero net magnetization. This effect is mainly promoted by uncompensated (UC) spins in the crystalline structure, which are originated by uncompensated rows, grain boundaries, structure defects, strain. . . The UC spins are spins of atoms which do not interact with the others, but in the presence of an external field they act as a paramagnet. For this reason, during many years antiferromagnetic materials were supposed to be as paramagnetic ones. All these phenomena may disguise the real nature and properties of magnetic nanomaterials and is of crucial importance a deep knowledge of them, both structural and magnetic. The maximum on this net magnetization in AFM materials is achieved for a critical temperature where the magnetic transition occurs, known as Néel temperature (T_N), and the highest the T_N , the highest the AFM exchange coupling energy. The emerging problem, when antiferromagnetic nanomaterials are attempted to be characterized by magnetometry, is the huge amount of mass needed to obtain enough magnetic signal. This drawback has forced scientists to adopt different strategies: such as the buildup of multilayer samples [8] or the development of new sophisticated characterization tools. Among them, X-ray magnetic circular dichroism (XMCD) is a surface technique that is gaining increased attention in synchrotron-based sources to analyze magnetic domains in AFM samples [9, 10].

In addition to the weakness of the magnetic signal, when an antiferromagnetic material is studied, a number of other reasons justify the use of specific heat measurements to study their critical behavior. In oxide nanocrystals, loosely coupled surface spins are often present. Although they represent a small fraction of the total number of magnetic moments in the sample, their magnetic signal dominates in magnetic susceptibility measurements and it may hide the weak magnetic signal characterizing the order-disorder transition at T_N [11]. At the nanoscale, the properties of the matter are affected by structural irregularities. Since nanomaterials present a large ratio of atoms placed on the surfaces, grain boundaries

or defects, which suppose imperfections from the crystalline point of view, affects also the magnetic properties of the matter. The antiferromagnetism, as it also happens with any magnetic interaction, is highly dependent on the crystalline structure. So, due to the superficial stress, there is a crystallinity decrease, which modifies the distances between atoms and then J is also changed. Remembering the Bethe-Slater curve (Figure 4.2) and Equation 4.1, if the exchange integral changes, a particular material may exhibit magnetic behavior or it could disappear. The geometrical frustration [12] or the competing ferromagnetic and antiferromagnetic interactions may lead to different and, perhaps, more complicated magnetic structures as magnetic dead layers or spin glasses and loosely coupled or UC spins [13]. A magnetic dead layer acts as a wall for the magnetic interaction when it is thicker than the magnetic correlation length. It limits and even avoids the magnetic interactions through it.

We recall the first law of thermodynamics, which states that the internal energy of a given magnetic system can be written as

$$dU \equiv dQ + dW = TdS + \vec{H}d\vec{M} \quad (4.2)$$

where T is the system temperature, S its entropy, \vec{H} the applied field and \vec{M} its magnetization. In systems where the total magnetization is null or very small ($\vec{M} \approx 0$), as in antiferromagnets, it is very difficult to calculate the energy involved on the magnetic interaction by magnetometric techniques. They are not enough sensitive on these systems and Equation 4.2 is reduced to the expression $dU = TdS$, then the magnetic interaction could be studied through an extensive property, the heat capacity, which reports information about the system stored energy. The heat capacity is sensitive to any change on the energy within the sample volume, i.e. their atoms, and the interaction between the spins is related with the magnetic entropy, which changes when a magnetic transition occurs. Then the heat capacity reveals information about the own magnetic transition [14].

4.1.1 The cobalt oxide system

The cobalt oxide (CoO), also called cobalt monoxide, belongs to the simplest chemically one-metal family of compounds with antiferromagnetic spin alignment, which are the most common materials that exhibit magnetic properties. Even magnetically undiluted materials, that are paramagnetic at room temperature, usually reveal a Néel transition if the temperature is lowered far enough. The present work focus on CoO, which incorporates ions of the $3d^7$ electronic configuration, and that belongs to one of the most studied crystallographic systems, both in basic science investigations and for practical applications. Previous heat capacity measurements on CoO were undertaken on multilayered samples made of thin CoO layers, each layer being separated from the other by SiO_2 and MgO layers [15, 16].

4. ANTIFERROMAGNETIC INTERACTION IN CoO

The physical explanation for the magnetic interaction in this family of oxides cannot be found in a simple Heisenberg exchange interaction between first neighbors. The strength of the direct exchange interaction depends on the orbital overlap between cobalt and oxygen atoms. The Heisenberg form of exchange applies to some localized systems, but fails even for magnetic oxides such as CoO, because the metal ions are too far apart for the mutual electron repulsion term $e^2 = r_{i,j}$ to establish an antibonding state with a Hund's rule parallel spin alignment. The magnetic behavior of transition metal oxides is governed by a less familiar form of exchange. In those systems, there must be a magnetic interaction that couples second nearest neighbors that observes the Pauli exclusion requirement of antiparallel alignment, so that, their spins have opposite orientations. That way, oxygen atoms always lie midway on the line between next nearest neighbors. This form of mediated or "indirect" exchange interaction is known as *superexchange*. This model proposed by Hendrik Kramers in 1934 [17], describes this effect quite well. Later, in 1950, Phillip Anderson refined the model of Kramers [18]. Superexchange is the coupling of cations spins through the medium of nearest-neighbor anion ligands. It operates in many ionic oxides and localized couples, usually with 3d moments. In the CoO, and below T_N , the Co moments (3d orbitals) are coupled by superexchange interactions mediated by the oxygen atoms (2p orbitals).

The CoO is composed of two elements: cobalt and oxygen. It has two stable phases, the cobalt (II) oxide (CoO) and the cobalt (II,III) oxide (Co₃O₄). The first one is stable up to ~ 800 -1000 K, but in presence of oxygen converts to Co₃O₄, and returns to CoO in a reversible way when cooled in oxygen absence [19]. Then, obtaining one of the two phases from evaporated pure metallic cobalt, depends on the substrate temperature and on the oxygen partial pressure. Moreover, CoO has three different allotropes, the stable one which crystallizes in the rock salt (RS) structure, and two metastable structures of the zinc blende and wurtzite types. Only RS structure shows antiferromagnetic behavior below the Néel temperature. The reason of this magnetic behavior, in the CoO (see Figure 4.4), is a structural contraction along the [1 0 0] directions between the paramagnetic state which corresponds to a face-centered cubic (fcc) structure, with space group $Fm\bar{3}m$, and the AFM state coupled to a body-centered tetragonal (bct) structure, with space group $I4/mmm$ [20–22]. Over the years, different works have established the critical temperature of this transition between 288 and 293 K for the bulk [23, 24].

The election of CoO in this work is due to the large magnetic moment of cobalt and to the value of its magnetic transition temperature. Its magnetic moment promotes a higher heat capacity signal, and the value of its T_N allows engineering applications because it is located around room temperature, when compared with other stable magnetic oxides as nickel oxide (NiO) [25] and manganese oxide (MnO) [26]. Other antiferromagnetic monoxides, such as the iron monoxide (FeO), are not considered because of their instabilities, since FeO decomposes below 575°C following the reaction $4 FeO \rightarrow Fe + Fe_3O_4$ [27]. Fur-

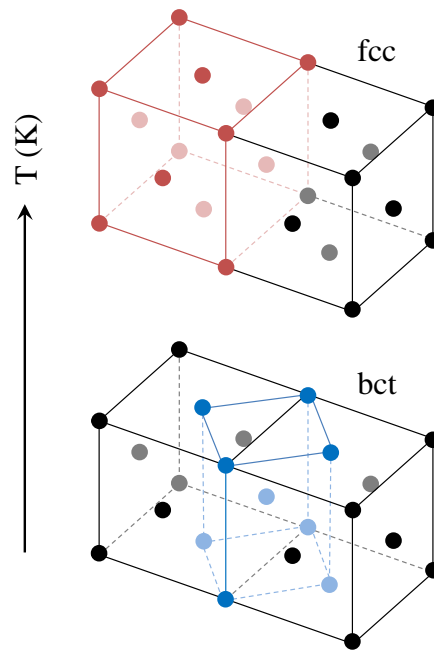


FIG. 4.4 Outline of the structural elongation along the $[100]$ planes, when temperature rises, and the system undergoes a transition from a bct to a fcc structure.

ther, CoO thin films or nanograins often constitute the AFM element of exchange-biased systems [28,29]. For these reasons, CoO can be seen as the archetype of the antiferromagnetic oxides.

Figure 4.5 represents the CoO RS structure on its PM state (in this structure the magnetic alignment is clearly evidenced unlike the tetragonal one and this explains why this structure is used). The spins on some nearest-neighbor transition metal ions are parallel (atoms that belong to the blue plane, and to the red plane), those on other nearest neighbors, which ones are mediated through an oxygen atom are antiparallel (couples of atoms one of them belonging to the blue plane and the other to the red plane). Thus, the spins within a given (111) plane are parallel to each other and antiparallel to those on the two adjacent (111) planes.

4.2 Experimental

As introduced in previous Section, the thermodynamic properties could be understood through a deep knowledge of the samples microstructure as grain size, density of grain boundaries... In this work, different thin film samples have been prepared, modifying their thickness and growth temperatures.

The samples were grown at the LCP-UAB in collaboration with Dr. Francesc Pi. We used both the

4. ANTIFERROMAGNETIC INTERACTION IN CoO

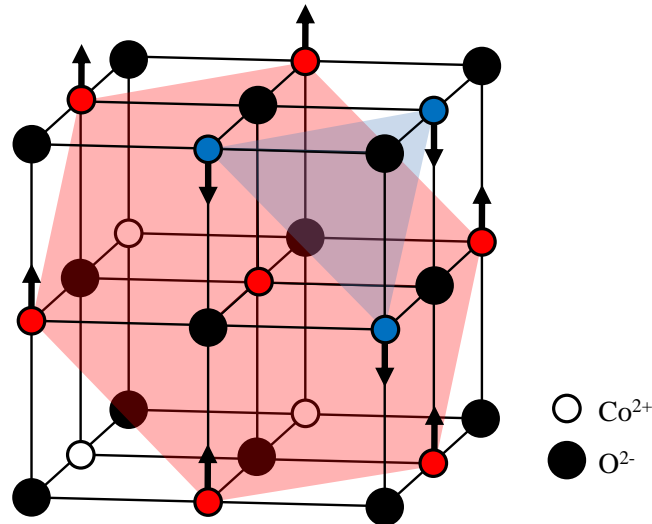


FIG. 4.5 Scheme of the CoO magnetic structure, for geometrical simplicity we use the fcc CoO structure. The spins orientation is indicated by arrows on the transition metal ions. We observe alternating (1 1 1) planes with different FM alignment, which are indicated by red (up spins) and blue (down spins).

in-situ and the immersion cryostat experimental setups described in Section 2.2 *Experimental setups*. Deposition conditions were: base pressure of 1×10^{-6} mbar, a variable oxygen partial pressure raised up to 1×10^{-3} mbar to promote a reactive atmosphere, and substrate temperature fixed between room temperature (RT) and 800 K. Pure metallic cobalt (99.95% purity) is then evaporated at a constant rate of 1.0 ± 0.1 Å/s, obtaining samples whose thicknesses range from 1 to 60 nm. These growth conditions produced samples with different microstructures, phases and even compositions. For this reason a structural and compositional characterization of the samples was done by using XRD, TEM and SQUID.

The CoO samples characterized by XRD were grown in 4×4 mm² silicon (100) pieces using their native SiO₂ as substrate. Their thickness is around 60 nm to ensure detection with a conventional diffractometer, a Philips X'Pert X-ray Diffractometer, which used a Co source with an off-plane inclination of -10° , focusing the Co K α at 1.72 nm. Measurements were conducted in the angular range from 20° to 80° in 2θ .

The SQUID samples were grown in the same 4×4 mm² pieces, but 10 nm thick, and covered *in-situ* by a 20 nm gold layer to prevent sample oxidation or contamination. The magnetometric characterization was carried on through a Quantum Design SQUID MPMS-XL7. The samples were zero-field cooled (ZFC) from a temperature of 300 K, and then measured at 10 K with a reversible field of ± 1 T.

The TEM samples were grown onto commercial TEM windows from SPI Supplies for the planar observations, while for the cross-sectional TEM (XTEM), samples were grown on both silicon wafer substrates

and nanocalorimeters. Typical nanocalorimeters are not adapted to plane view observations, because the calorimetric cell is too thick and blocks the electrons beam. The substrate in the case of the TEM windows is made of Si_3N_4 , for the silicon pieces it is SiO_2 , and for the nanocalorimeters it can be both SiO_2 and Si_3N_4 . In fact, the SiO_2 final layer, onto the devices membrane, may be removed by HF etching with the aim to reduce the device addenda, and hence improving its sensibility. It has been verified that the CoO microstructure does not change between the different substrates. Cross sections were prepared by Ar-ion milling the Si pieces starting at 6 keV (LN2 cooled when necessary) and finishing with an energy of 300 eV to remove artifacts. In the case of the nanocalorimeters, they were sandwiched using PELCO Eponate 12 Kit with BDMA and then cut, in the sample zone, into slices by means of a Leica EM UC6 Ultramicrotome. The thickness of the samples examined by TEM and measured with nanocalorimetry range from 1 to 20 nm. These samples are examined using two different microscopes: a JEOL JEM-2011 with point resolution between 0.14 - 0.19 nm, operated at 200 kV, which incorporates a Gatan 794 MSC 600HP CCD camera, and with a JEOL JEM-3010 HRTEM with point resolution of 0.17 nm, operated at 300 keV, with a Gatan Imaging Filter (model GIF Tridiem).

4.2.1 Nanocalorimetric approach

The first part of the study involves the dependence of the magnetic transition on samples thickness. The samples were measured by using the electronics based on INA 110 and 114 operational amplifiers. The thicknesses range from 1 to 20 nm and the layers are grown at 525 K and 2×10^{-4} mbar of oxygen partial pressure.

The second part of the study investigates the dependence of the magnetic interaction with samples microstructure, which was modified by changing the growth temperature, and by applying thermal treatments to the sample after grown. We used the improved electronics based on INA 103 operational amplifier. In this case, two different samples were measured; their thickness and oxygen partial pressure during growth were fixed at 20 nm and 2×10^{-4} mbar, respectively, while the substrate temperature was 300 K and 675 K. The sample grown at 300 K was subsequently submitted to high temperature annealings, or thermal treatments, up to 675 K to modify its crystallinity.

Finally, to study the influence of the growth protocol on the microstructure, we studied by QAnC the signature of two pairs of samples, which were grown at 2×10^{-4} mbar P_{O_2} and 525 K, one couple 6 nm thick, and the other 8 nm thick. We used a different growth protocol for the sample of every couple: continuous or by steps of 1 nm.

4.3 Microstructural study

Several samples of CoO have been grown onto Si (1 0 0) substrates. An extensive study of evaporation conditions has been performed by varying substrate temperature and oxygen partial pressure, while the evaporation rate was kept constant. Figure 4.6 illustrates the influence of the oxygen partial pressure on phase formation. At a deposition temperature of 300 K low oxygen partial pressures result in metallic hexagonal close-packed (hcp) cobalt (α -phase) (PDF 00-005-0727), while above 6×10^{-5} mbar only face-centered cubic (fcc) CoO is obtained (PDF 00-048-1719).

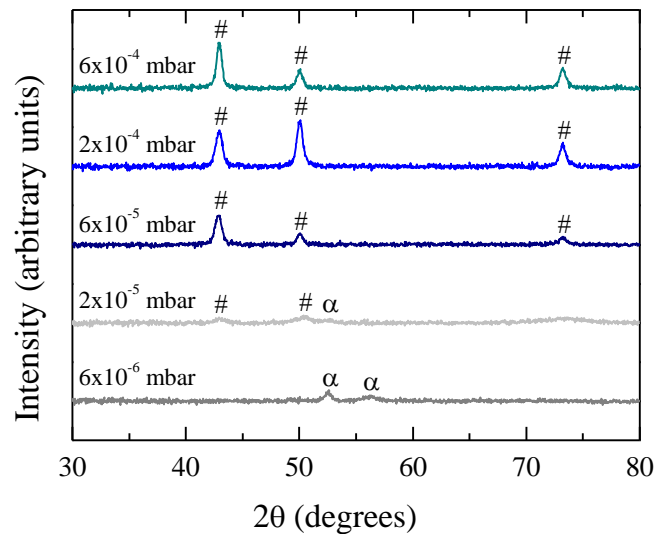


FIG. 4.6 XRD diffractograms obtained from samples deposited at different oxygen partial pressures keeping at 300 K the substrate temperature. The symbol # corresponds to fcc-CoO reflections: in 2θ at 42.7° (1 1 1), 49.7° (2 0 0), and 72.9° (2 2 0). While α indicates the hcp-Co reflections: in 2θ at 52.5° (0 0 2), and 55.9° (1 0 1).

Figure 4.7 highlights a similar behavior for CoO samples grown at 525 K. At low oxygen partial pressures only metallic α -Co phase forms, while at higher pressures fcc-CoO is the only phase observed. At 525 K, we observe a modification of the α -Co pattern respect to the RT microstructure, the (1 0 1) reflection disappears and instead the (1 0 0) is observed.

The diffractograms corresponding to samples grown at 800 K (Figure 4.8) show a large variation of their microstructure with respect to the samples deposited at lower temperatures. At low partial pressures, a metallic phase is observed again, but in this case we assume that it corresponds to the fcc-Co phase (PDF 00-015-0806). When oxygen partial pressure increases a mixture between fcc-Co and fcc-CoO phases is obtained. This limits the temperature range suitable to study the effect of the microstructure onto the CoO magnetic properties.

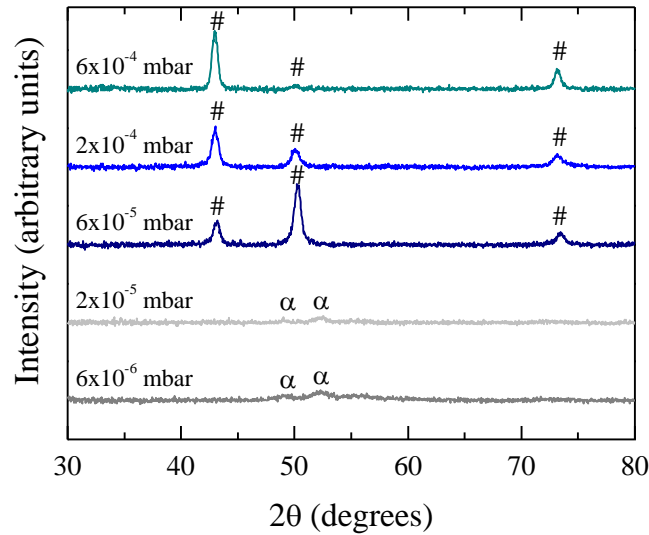


FIG. 4.7 XRD diffractograms obtained from CoO samples deposited at different oxygen partial pressures keeping at 525 K the substrate temperature. The symbol # corresponds to fcc-CoO reflections, while α indicates the hcp-Co reflections: in 2θ at 48.8° (1 0 0), and 52.5° (0 0 2).

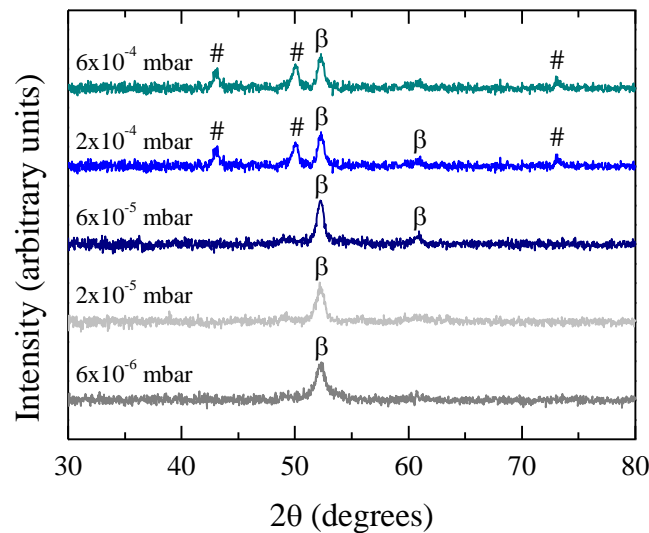


FIG. 4.8 XRD diffractograms obtained from CoO samples deposited at different oxygen partial pressures keeping at 800 K the substrate temperature. The symbol # corresponds to fcc-CoO reflections, while β indicates the fcc-Co reflections: in 2θ at 51.9° (1 1 1), and 60.7° (2 0 0).

As observed for the XRD diffractograms obtained at the lower oxygen pressures, discrimination between α -Co and β -Co phases is not straightforward, because the diffraction peaks intensity of both phases is very weak and they are also superposed. With the aim to discriminate if diffractograms differences are due to two metallic phases instead of a high texture along the α -Co (0 0 2), complementary, SQUID analysis where performed on different samples to differentiate hcp from fcc Co structures by their ferromagnetic signal, since both of them show different magnetic properties [30]. Figure 4.9 shows the magnetization curves acquired at 10 K for pure cobalt 20 nm thick films deposited at 5×10^{-6} mbar, but

4. ANTIFERROMAGNETIC INTERACTION IN CoO

at different deposition temperatures. The external field was applied parallel to the surface. The sample deposited at 300 K shows a lower coercive field (25 Oe) compared with film deposited at 800 K (125 Oe). The results show that the hard magnetic behavior corresponds to the fcc-Co structure instead of the hcp-Co, as previously reported in 40 nm thin films of cobalt successively annealed from the as-deposited state [31].

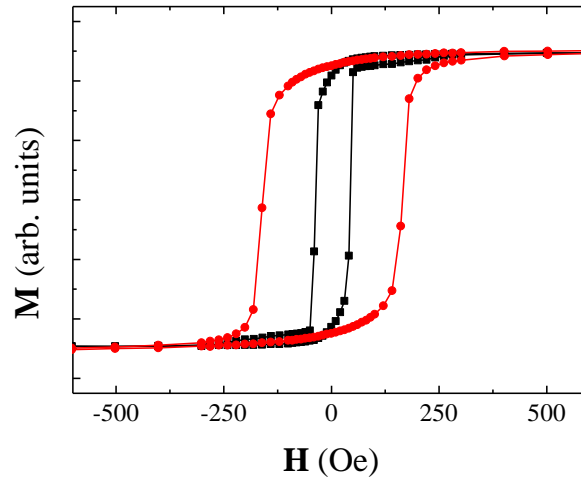


FIG. 4.9 Hysteresis loops over a field variation of ± 1 T at 10 K for two samples, one grown at 300 K (black squares) and the other at 800 K (red circles).

By depositing additional samples at intermediate temperatures and pressures, we were able to draw a phase diagram of vapor phase deposited films, as a function of temperature and oxygen partial pressure (P_{O_2}), as shown in Figure 4.10. As a general trend, in the studied temperature range (from 300 to 800 K), the films deposited at the lowest oxygen pressure showed metallic character with an hcp to fcc-structure transformation appearing as temperature increases. As the deposition temperature increases, the P_{O_2} domain of existence of the hcp-Co phase increases very slowly while fcc-Co domain increases considerably up to 10^{-4} mbar. For high oxygen partial pressures ($> 2 \times 10^{-5}$ mbar) and low temperatures (< 700 K), cobalt transforms into the low-valence fcc cobalt monoxide, which appears to be the stable phase in very large oxygen partial pressure and temperature domain. Only for temperatures above ~ 750 K and P_{O_2} larger than 10^{-4} mbar, a mixture of metallic cobalt and cobalt monoxide was observed. This phase diagram is be used to perfectly control the crystalline phase deposited, simply by tuning the deposition temperature and oxygen partial pressure.

4.3.1 Thickness influence

The influence of thickness on CoO magnetic properties is studied on different samples which ranges from 1 to 20 nm thick. The samples are evaporated at a fixed temperature of 525 K and at 2×10^{-4}

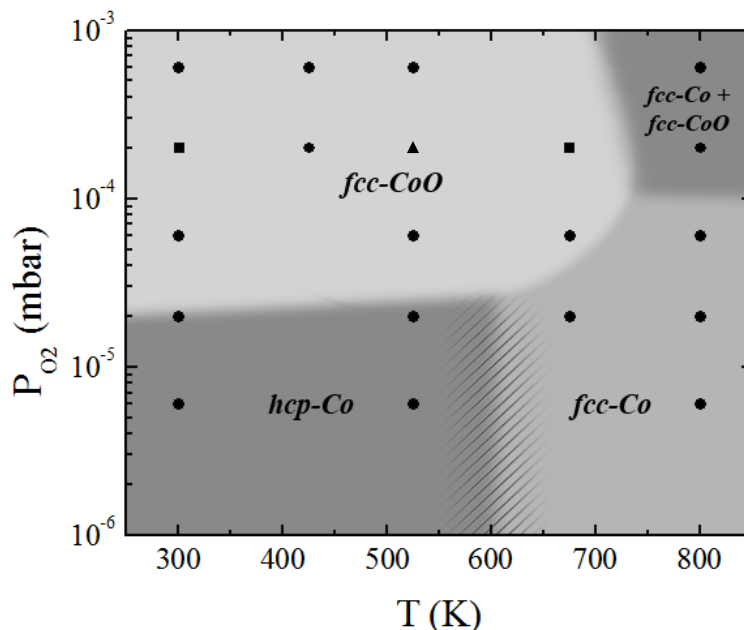


FIG. 4.10 Phase diagram of samples obtained when metallic cobalt is evaporated in oxygen reactive atmosphere at different substrate temperatures. Dots represent characteristic regions for which samples were prepared, not all the samples are represented in the diagram.

mbar of oxygen partial pressure (triangle-shaped point in Figure 4.10). The sample of 1 nm thick [Figure 4.11(a)] does not show any trace of crystallinity. The halo of the electron diffraction (ED) pattern [Figure 4.11(a) inset] corresponds to the amorphous contribution of the deposited CoO and substrate. The energy-dispersive X-ray spectroscopy (EDS) analysis confirms the presence of cobalt. When the sample thickness reaches 2 nm [Figure 4.11(b)], the image taken by the CCD camera is different to the previous one; the ED pattern shows an incipient crystallinity which corresponds to the sample. An inflection occurs when the film reaches 3 nm thick; it is the presence of well-defined grains and boundaries [Figure 4.11(c)]. The corresponding ED pattern shows three rings which match perfectly with the three most important reflections of fcc-CoO structure: (1 1 1), (2 0 0), and (2 2 0). From this thickness and thereafter, the grains increase their diameter with films thickness, the greater the thickness, the larger the grains size. Besides, the corresponding ED patterns show the rings that belong to the fcc-CoO structure, which indicate that samples are completely polycrystalline [Figures 4.11(d), 4.11(e), and 4.11(f)].

Figure 4.12 shows the mean grain diameter obtained after statistical analysis around 100 grains in samples ranging from 3 up to 20 nm. The grain distribution is nearly monodisperse with a standard deviation that increases with film thickness. The nanograins mean diameter increases with film thickness but remains smaller than the thickness of the layers.

To resolve the microstructure we carried out XTEM measurements on two samples, with thicknesses of

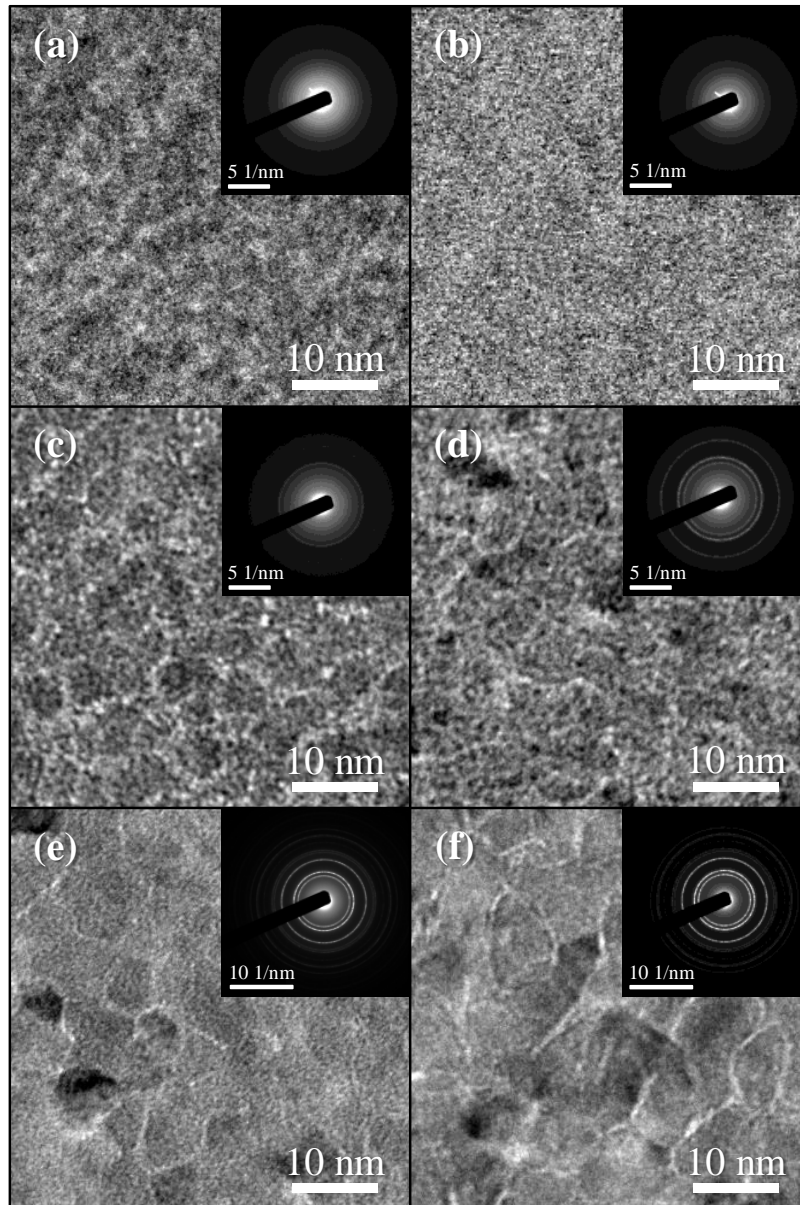


FIG. 4.11 TEM plane view images for CoO samples of different thicknesses: (a) 1 nm, (b) 2 nm, (c) 3 nm, (d) 8 nm, (e) 10 nm, and (f) 20 nm. The corresponding ED captures are included for every image as insets.

2 and 20 nm. Figures 4.13(a) and 4.13(b) show that the 2 nm thick sample is continuous, perfectly wets the silicon nitride substrate and lacks features associated to crystalline grains. We therefore infer that samples thinner than 3 nm are essentially disordered. The XTEM image for the 20 nm thick sample is substantially different, as shown in Figure 4.13(c). The CoO microstructure follows a columnar growth. The dark field image from the previous one is shown in Figure 4.13(d), and it denotes the polycrystalline nature of the samples. Most of the columns have a conical shape, which could be due to the different growth velocity of the three main families of planes observed on the ED patterns. This growth velocity differences promotes the appearance of impingement during growth. Nevertheless, these grains can be

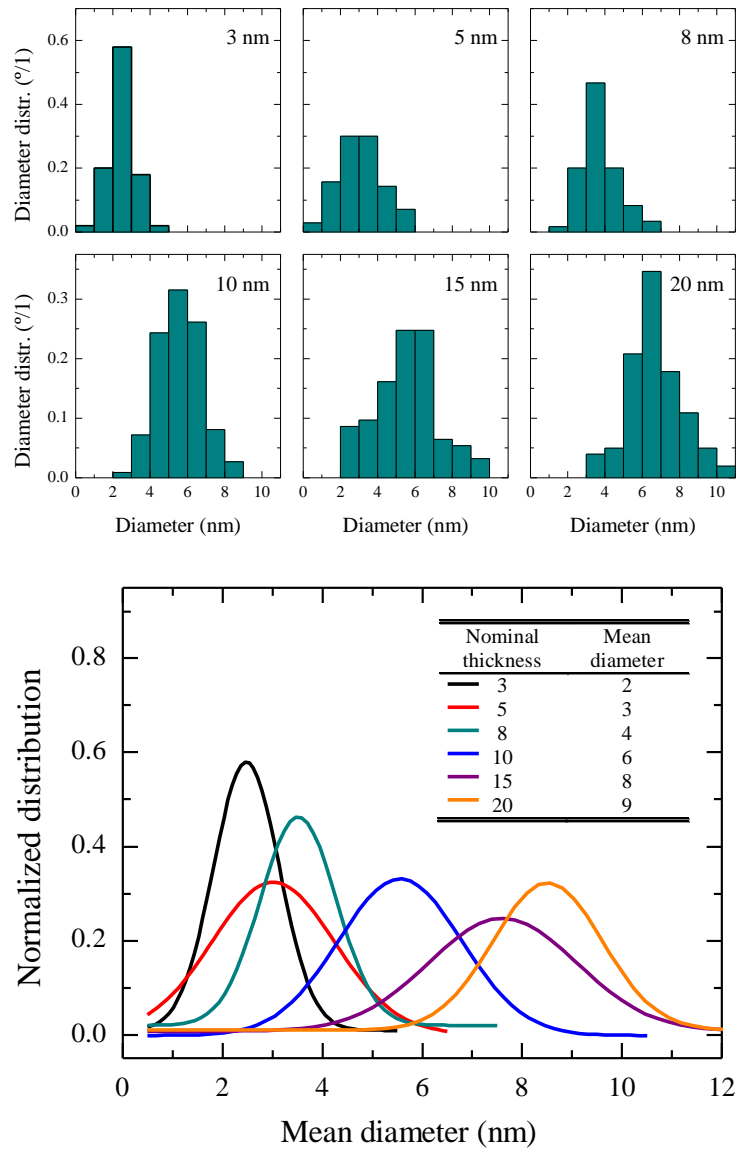


FIG. 4.12 The six upper small graphs represent the number of particles in function of their diameter distribution for different samples thickness. The lower graph shows the Gaussian fit for the grains diameter distribution versus the thickness of the films.

treated in average as columns.

Figure 4.14 illustrates the dependence of both in plane and out plane grain size as a function of nominal thickness. This graph clarifies the microstructure dependencies with thickness: while the nanograins height scales with film thickness, their width evolves slower. As a consequence, the anisotropic grains lead to columns due to the impingement between nanograins. The non-crystalline nature of the sample during its first growth stages is promoted by the amorphous nature of the substrate [16].

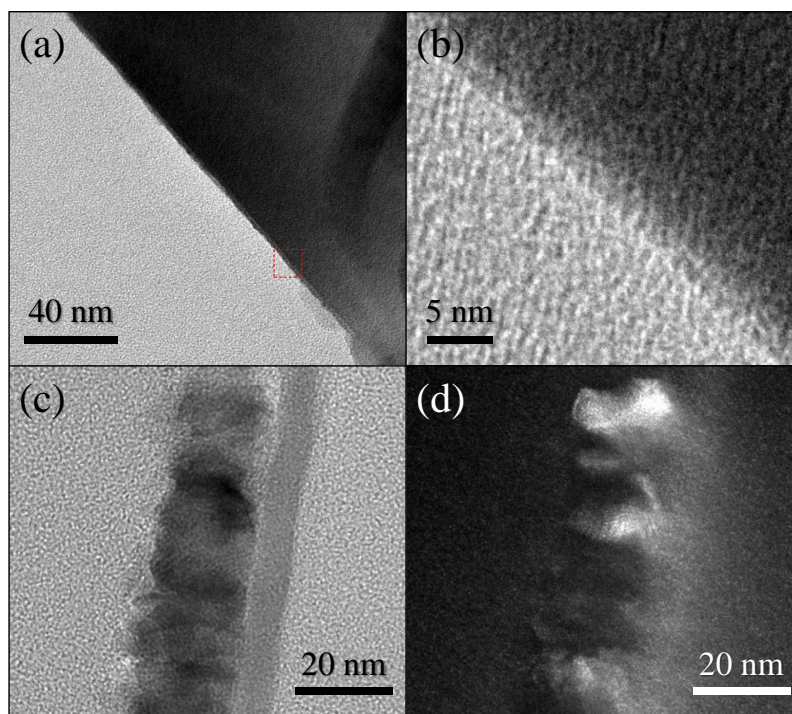


FIG. 4.13 XTEM images for 2 nm thick CoO sample (a) and its magnification from the red dashed squared zone (b). XTEM image for 20 nm thick CoO sample in bright field (c) and the same area in dark field (d).

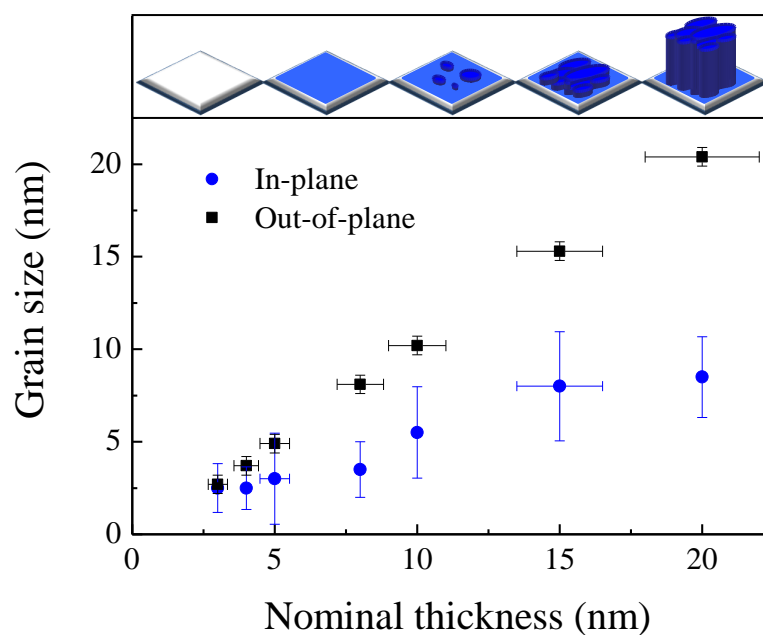


FIG. 4.14 Grain size in-plane and out-of-plane respect to the nominal thickness. The inset shows schematics of the grains structure evolution with film thickness.

4.3.2 Influence of growth temperature

Microstructure characterization was performed on 20 nm thick films grown at identical P_{O_2} (2×10^{-4} mbar) but at different substrate temperatures. Figure 4.15 shows plain view micrographs of films deposited at 300, 675 and 800 K, as well as a sample deposited at 300 K and submitted to a thermal treatment at 675 K during 10 hours. As can be clearly seen in the images, films deposited at 300 K [Figure 4.15(a)] are formed by non-touching well faceted grains, triple points formed by boundaries almost perfectly at 120° from each other, are clearly observed, hinting that growth was performed close to equilibrium. Very rarely twin boundaries are observed. The average grain size was estimated around 6.7 ± 2.0 nm. In the case of sample deposited at 300 K and submitted to a thermal treatment [Figure 4.15(b)], we observe how the grains are touching and fill the space. In this case most of the grains are faceted and occasionally they overlap. The average grain size is 7.1 ± 3.3 nm. The grain growth, promoted by the thermal treatment, is produced mainly in grain boundaries and it is limited by the proximity of neighboring grains. At 675 K [Figure 4.15(c)], films are continuous with touching grains; mainly faceted. More curved and irregular boundaries and rounded up corners are observed compared to lower deposition temperature samples. Many of the triple points are still close to 120° ; however, other triple points seem to be far from equilibrium. Although not frequent, some twins are observed. In that case, grain size is farther off from monodisperse and an average grain size of 18.9 nm is defined with a standard deviation of 8.6 nm.

Films deposited at the highest temperature, 800 K, showed a complete different microstructure [Figure 4.15(d)]. The layer is formed by grains embedded in a matrix. These grains are mainly formed by grown-together grains with very irregular size and shape, and thus distribution size. Some tiny individual grains with a more droplet like shape are seen at the empty areas between the large islands, which show facets and rounded corners. The large islands seem to be formed by incomplete coalescence, during which grain boundaries are preserved within the large island. These grain boundaries show that grains with different orientation coalesced, but the temperature was not enough to reach a perfect recrystallization. Frequency of twinning is high. This microstructure perfectly matches, that expected from XRD, where cohabitation between two phases, fcc-Co and fcc-CoO is detected. Although we cannot confirm it by TEM, due to the higher density of the nanograins, we can suppose that they are constituted of metallic cobalt, and that nanograins are embedded in an oxide matrix as high deposition temperature could have promoted surface oxidation of the grains.

From the cross-section analysis we were able to confirm microstructure and growth habit (Figure 4.16). Films deposited at 300 K were 22 ± 1 nm thick [Figure 4.16(a)], with a clear columnar type growth, and

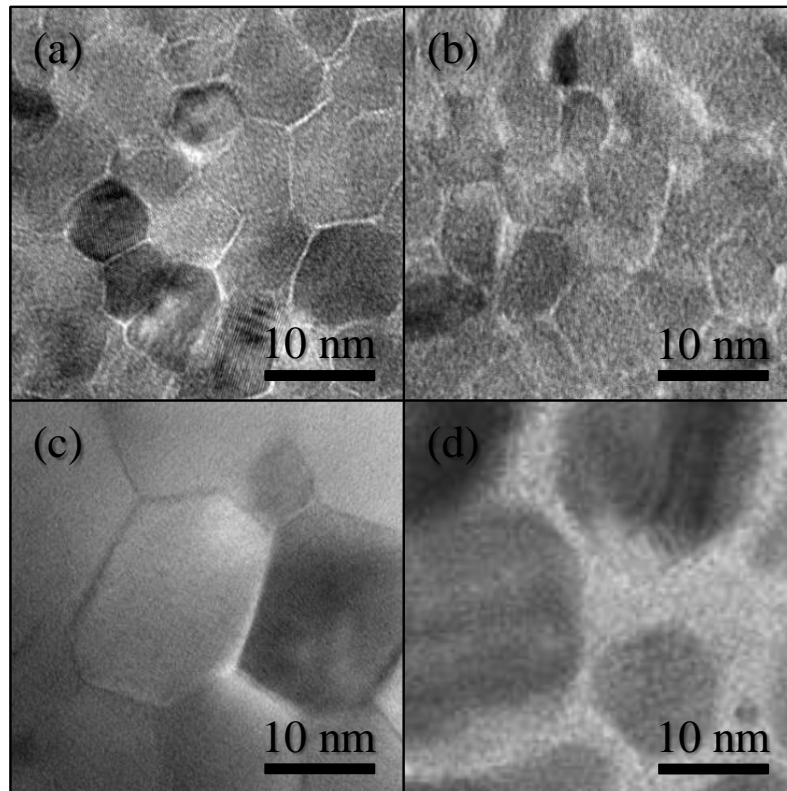


FIG. 4.15 TEM plane view images for 20 nm thick CoO samples growth at different substrate temperature: at 300 K (a), at 300 K and after a thermal treatment at 675 K during 10 hours (b), at 675 K (c), and at 800 K (d).

column width varying from 6 to 10 nm, in accordance with observation in plain view. Also a competitive microstructure with some V-shape grains is clearly observed. Similarly, the sample deposited at 300 K and submitted to a thermal treatment is mainly columnar [Figure 4.16(b)]. However, we can also find V-shaped grains, indicating competitive growth, and the grain boundaries are almost parallel to the surface. On the contrary, films deposited at 675 K were 20 ± 2 nm thick with clear columnar structure [Figure 4.16(c)]. In that case, average column height is almost identical to the layer thickness and grain boundaries are almost perfectly normal to the surface. While the interface between the membrane and the CoO is smooth, the free surface of the layer is rather rough. As expected, films deposited at 800 K showed non uniform thickness [Figure 4.16(d)], the films are formed by disjunctive grains with seems to be covered by a core-shell like structure. The observed grains are ~ 25 nm wide and ~ 10 nm thick.

From the structure-zone models for evaporated films [32,33], we have grown our films from $T_S/T_M \approx 0.1$ (300 K) to $T_S/T_M \approx 0.3$ (675 K), where T_S is the growth temperature, and T_M is the CoO melting temperature. We cross the zone I border, where structures are columnar, consisting of inverted cone-like units separated by wide boundaries showing a very limited adatom motion, to zone II, where structures are also columnar but with tighter grain boundaries, diffusion plays a role in the structures evolution

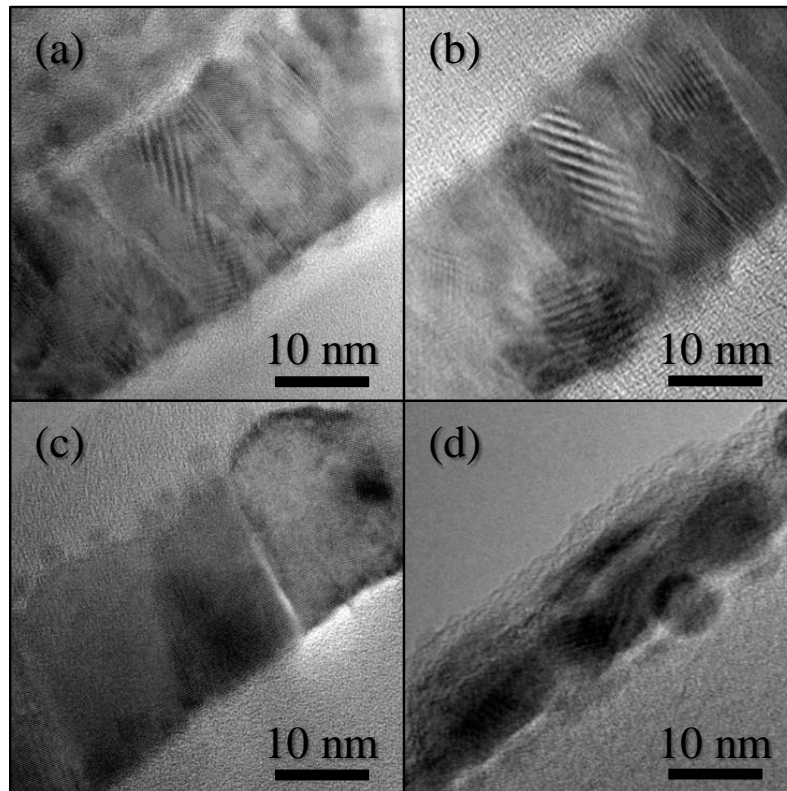


FIG. 4.16 XTEM images for 20 nm thick CoO samples growth at different substrate temperature: (a) at 300 K, (b) at 300 K and after a thermal treatment at 676 K during 10 hours, (c) at 675 K, and (d) at 800 K.

because columnar grain size increases with T_S . Grain boundaries are also nearly perpendicular to the film plane with denser microstructure. The morphology in our films agrees with reported models. However, samples microstructure deposited at 800 K doesn't behave as expected and it deviates dramatically from predictions. The reason is the Co - O bond instability at high temperatures, previously reported [19].

4.4 Antiferromagnetic interaction

4.4.1 Thickness dependence

The specific heat data measured on samples from 1.5 to 20 nm thick are shown in Figure 4.17. The specific heat increases monotonously with temperature, as expected for a dominant lattice contribution. An additional contribution develops as one goes from thin to thick films, which represents the sample magnetic specific heat. The Néel temperature was taken as the temperature at which the inflexion of the C_P curve occurs (see Figure 4.17). The T_N value and the specific heat jump occurring at T_N decrease with decreasing sample thickness. Further, a progressive rounding of the curve representing the temperature

4. ANTIFERROMAGNETIC INTERACTION IN CoO

dependence of the magnetic specific heat is found as one goes toward thinner films. This rounding cannot be due to sample temperature inhomogeneities since it would be identical in all samples. Rather it can be attributed to the existence of a certain size distribution of the CoO nanograins, which tends to be relatively larger in smaller grain size samples. Alternatively, an intrinsic broadening of the specific heat anomaly may exist in nanosize granular systems [14].

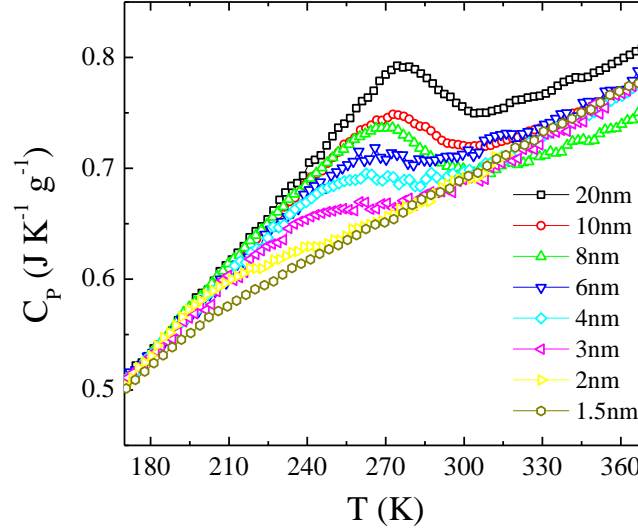


FIG. 4.17 Specific heat extracted from the raw heat capacity measured on the different CoO thin films, from 1.5 to 20 nm.

The variation of the Néel temperature as a function of the grain mean diameters (d) is plotted in the inset of Figure 4.18, and in this Figure a log-log plot of the same quantities as a function of d is shown. The linear behavior revealed by this last plot implies that the Néel temperature follows grain diameter power law dependence. This is in agreement with the Binder theory of critical phenomena in reduced dimension systems [14]. The Néel temperature is expected to obey the following relation:

$$\frac{T_N^{bulk} - T_N^{grain}}{T_N^{bulk}} = \left(\frac{d}{\xi_0} \right)^{-(1/\nu)} \quad (4.3)$$

where T_N^{bulk} is the Néel temperature in the bulk, T_N^{grain} the Néel temperature extracted from the measurement of nanograin films, ξ_0 the magnetic correlation length at $T = 0$ K, and ν the critical exponent related to ξ_0 [note that $\xi(T) = \xi_0(1 - T/T_N^{bulk})^{(-\nu)}$].

The best adjustment between Equation 4.3 and our data (solid line in Figure 4.18) is obtained for $\xi_0 = 1.0 \pm 0.1$ nm and $\nu = 0.48 \pm 0.02$. The short value of the correlation length is consistent with the fact that superexchange coupling is short-ranged and the value of the critical exponent for the correlation length, close to one-half, is in agreement with the expected value within the theory of critical phenomena [14,34,35]. We also did try to adjust our data within the framework of the model of Lang et al. based on spin exchange interactions, however no correct fitting was obtained [36].

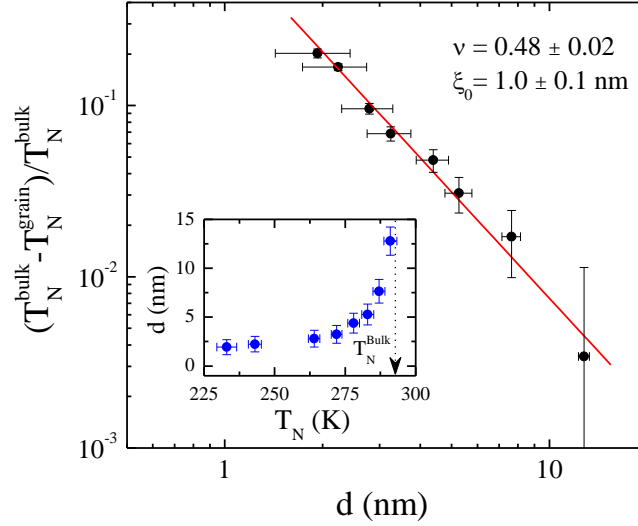


FIG. 4.18 Log-log plot of the variation of the Néel temperature as a function of the mean diameter of the CoO nanograins (d). The solid line in the best fitting obtained with the parameters set to $\xi_0 = 1.0$ nm and $\nu = 0.48$. The inset shows the grain diameter as function of the T_N in normal scale.

The full consistency of the present analysis leads us to conclude that the CoO films are made of an assembly of essentially exchange-decoupled nanograins. For an assembly of AFM grains, a weak inter-grain interaction is expected since there is no *a priori* reason that good lattice matching exists between neighboring grains. Several recent studies of exchange bias in nanosystems reached the same conclusions [37, 38]. Considering that the environment of surface atoms differs from bulk, the magnetic properties of the atoms at the grain surface should differ from those of the atoms in the core of the grains. In principle, the existence of weakly coupled magnetic moments should show up as an upturn in χ , the susceptibility, in magnetic measurements. Such measurements were attempted using highly sensitive SQUID magnetometry. Unfortunately, the weakness of the magnetic moment precludes any conclusions from these measurements.

The fact that the surface moments are not coupled to the moments in the bulk of the grains provide an explanation for the decrease in the magnetic specific heat per unit mass from large grain size to small grain size samples. Although within the Landau theory of second-order phase transition [35], the ratio $\Delta C_P / T_N$ should be approximately the same in all samples; it is actually smaller in small grain size samples than in large grain size ones. This implies that the number of spins involved in the magnetic transition is less in the former than in the latter. For each sample, the magnetic entropy (in $\text{J g}^{-1} \text{K}^{-1}$) is obtained by integrating the magnetic specific heat divided by the temperature ($\Delta C_P^{\text{magn}} / T$) in the entire temperature range, between 120 K and 330 K. The entropy deficit normalized to the bulk entropy is plotted in Figure 4.19 as a function of the nominal sample thickness. The curve obtained mimics the curve, also shown in Figure 4.19, representing the ratio of the number of surface to volume atoms

4. ANTIFERROMAGNETIC INTERACTION IN CoO

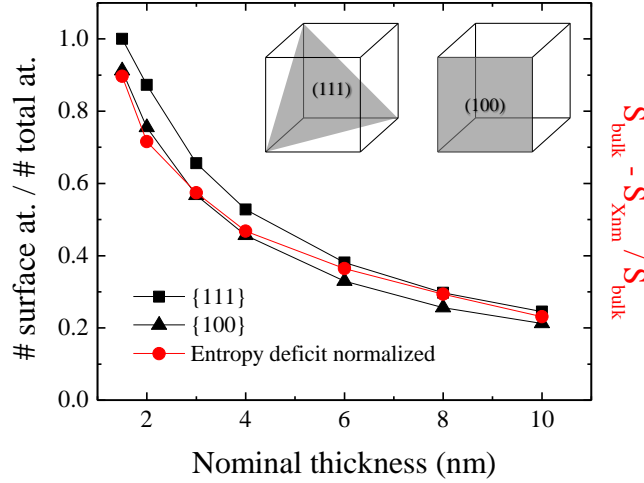


FIG. 4.19 Ratio of atoms in surface to the total number of atoms in a nanograin (considering surface densities of atoms for families of planes {1 1 1} and {1 0 0}) are compared to the normalized entropy deficit for each CoO film with respect to the value of the CoO film of 20 nm.

(number of surface atoms/number of total atoms) and calculated by using the TEM-derived grain size values.

4.4.2 Dependence on growth temperature

Figure 4.20(a) shows C_P curves of 20 nm thick films deposited at 300 K and 675 K, keeping constant the oxygen partial pressure at 2×10^{-4} mbar (square-shaped points in Figure 4.10). The T_N of samples grown at 300 K and 675 K is estimated at 284 ± 4 K and 290 ± 4 K, respectively. By fitting and subtracting the CoO lattice contribution to the specific heat, we also obtain the magnetic entropy of both samples [Figure 4.20(b)]. The Debye model [39], see Equation 4.4, is used to fit the lattice contribution to the CoO specific heat at constant pressure.

$$C_P \cong 9Nk_B \left(\frac{T}{T_D} \right)^3 \int_0^{(T_D/T)} \frac{x^4 e^x}{(e^x - 1)^2} dx \quad (4.4)$$

The sample deposited at higher temperature presents larger magnetic entropy ($\Delta S^{\text{magn}} = 42.1 \text{ mJ g}^{-1} \text{ K}^{-1}$), than the sample deposited at the lowest temperature ($\Delta S^{\text{magn}} = 23.5 \text{ mJ g}^{-1} \text{ K}^{-1}$). The magnetic entropy is obtained by integrating between 150 and 350 K.

The reported variations on transition temperature and magnetic specific heat or entropy, can be explained by microstructure differences between both samples (as previously shown in Figures 4.15(a), 4.15(c), 4.15(a), and 4.15(c)). The volume ratio of the interfacial to the crystalline components, for samples with a columnar growth, may be estimated by $4\delta/d$, where d is the average diameter of the columns

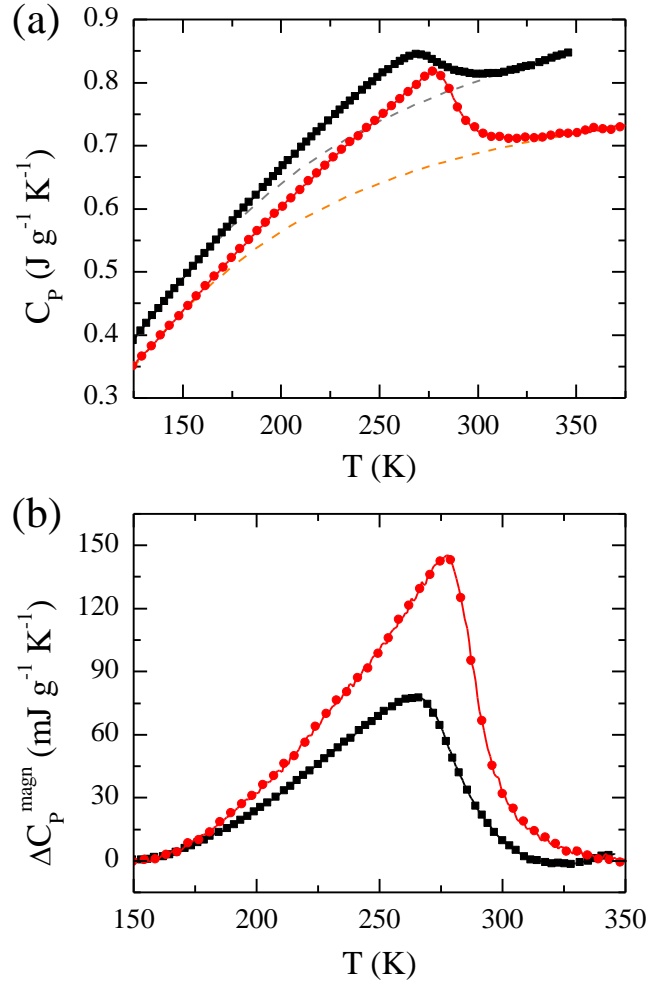


FIG. 4.20 (a) Specific heat curves for samples deposited at a substrate temperature of 300 K (black squares) and 675 K (red circles). Dashed lines correspond to the Debye model fitting of the lattice contribution. (b) Magnetic specific heat corresponding to the AFM to PM transition.

and δ is the average thickness of the grain boundaries, which is determined to be on the order of 3 to 6 atomic distances from the TEM images. The unit cell parameter of the fcc-CoO is 4.26 \AA [40], i.e. three atomic distances, then using an average value of $\delta = 7.10 \text{ \AA}$ (five atomic distances), the volume ratio for the sample deposited at 300 K is calculated to be 42% of the total volume, while the volume ratio for the sample deposited at 675 K is 15%. This difference is directly related with the magnetic entropy increase of almost 70%. The situation is remarkably different for sample grown at 300 K and annealed for several times at 675 K. In this case, the C_p data in Figure 4.21(a) exhibits significant changes while the microstructure, i.e. grain size, hardly evolves during the thermal treatments. Therefore, in this case, the ratio between interstitial and crystalline atoms, cannot account for the observed heat capacity variations, because the volume ratio for the sample reduces from 42% to 40%, while its thermodynamic properties, as the magnetic entropy increases up to $\Delta S^{\text{magn}} = 33.0 \text{ mJ g}^{-1} \text{K}^{-1}$, more than 40% [Figure 4.21(b)].

4. ANTIFERROMAGNETIC INTERACTION IN CoO

Generally, as the annealing time increases, the C_P at a given temperature decreases (we took 150 K as reference temperature), and the ΔC_P^{magn} or the energy related to AFM interaction increases, as shown in Figure 4.21(b). The sample annealed for 30 s shows a slightly different behavior since the specific heat remains constant, while the ΔC_P^{magn} shows the maximum increase. We interpret this behavior as being due to a stress relief in the crystalline grains during the first few seconds of the thermal treatment. Interestingly, as structural defects or interfaces may lead to uncompensated spins, their reduction or elimination by annealing can reduce the amount of these UC spins, as already observed by Gornakov et al. [41]. We cannot relate completely the increase of the ΔC_P^{magn} with the small grain boundary reduction through a grain growth (from 6.6 to 7.1 nm), as reported by the TEM characterization. Furthermore, the C_P reduction might be due to a partial oxygen mass loss during successive thermal treatments under high vacuum. Besides, grain growth may be understood with δ as temperature dependent variable: the higher the growth temperature or the thermal treatment time, the thinner the grain boundaries. Unfortunately, TEM characterization does not provide grain boundary images with enough resolution.

To gain more insight in the origin of the observed heat capacity variations and study the effect of the thermal treatments at the grains boundaries we investigate the behavior of the UC spins from magnetic measurements. The as-deposited sample reveals a spin-glass behavior when ZFC/FC curves are compared [Figure 4.22(a)]. The vertical shift ($M_E = 0.4 \pm 0.1$ emu/g) produced when FC measurement is done [Figure 4.22(a) inset] is the demonstration of the existence of UC spins [42] or FM coupling at grain boundaries [43]. However, we do not observe an exchange bias field, which suggests that the vertical shift is originated by frustrated spins (spin-glass behavior), which also promote a small hysteresis cycle. The saturation magnetization for this sample at 50 kOe is 7.7 emu/g. This is a very small value considering that a magnetization range of 161 - 283 emu/g results if all Co spins in bulk CoO are ferromagnetically ordered if the orbital Co moment is not, or is, quenched by the crystal field, respectively. In this sample the uncompensated spins represent almost the 3 - 5% of the total magnetic atoms of the sample. The results for the sample after the 4th annealing are shown in Figure 4.22(b). The saturation magnetization at 50 kOe is enhanced up to 26.7 emu/g, so that the quantity of atoms that align with external field have increased a value of 19 emu/g, which corresponds to the 9 - 17% of the magnetic atoms of the sample. The increase of the UC spins indicates a reduction of the spin-glass behavior, i.e. the energy provided to the sample has given mobility to the atoms to reorganize them and to overcome the frustration. However, the presence of exchange bias interaction [Figure 4.22(b) inset] suggests that these UC spins are in fact ferromagnetically coupled. This conclusion is supported by the high increase and the absolute value of the magnetization. As the thermal treatments are carried out under high vacuum, the CoO may be reduced to Co metal at grain boundaries, which explains the magnetization increase. The non-stoichiometric nature of the CoO located at grain boundaries may favor the formation of Co-

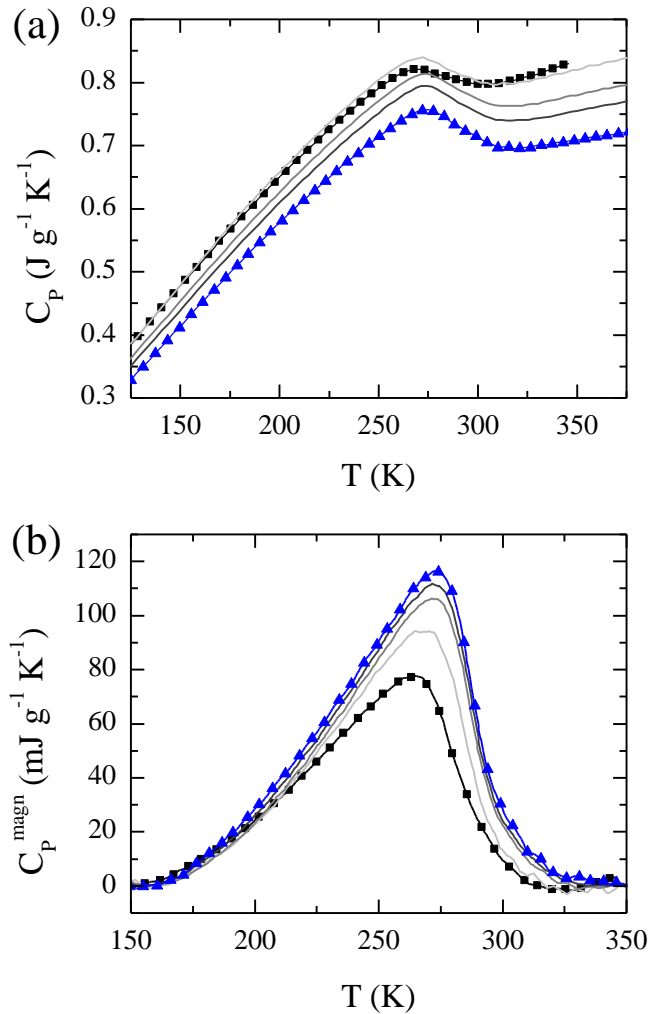


FIG. 4.21 (a) Specific heat curves for sample as-deposited at a substrate temperature of 300 K (black squares), and after successive thermal treatments at 675 K and during 0.01 h (light grey line), 0.1 h (grey line), 1 h (dark grey line), and 10 h (blue triangles). (b) Magnetic specific heat corresponding to the AFM to PM transition.

rich compounds when treated at medium temperatures in low oxygen pressure environments [44]. We believe the annealing procedure promotes pure Co clusters at the grain boundaries, while the oxygen diffuses through AFM grains improving the CoO stoichiometry. This will explain the AFM energy and the slight T_N increases, as clearly seen in Figure 4.21(b). As a consequence, an exchange coupling within the antiferromagnetic grains arises [Figure 4.22(b) inset] producing an exchange bias field $H_E = 510 \pm 20$ Oe. On the contrary, the vertical shift disappears, which corroborates that grain boundaries do not exhibit spin glass behavior yet.

The heat capacity curve for the sample deposited at 300 K and its successive thermal treatments show a different slope [see Figure 4.22(a)], which is clearly seen above the magnetic transition. This affects dramatically the Debye fitting because at temperatures far enough of the Debye temperature ($T \gg T_D$),

4. ANTIFERROMAGNETIC INTERACTION IN CoO

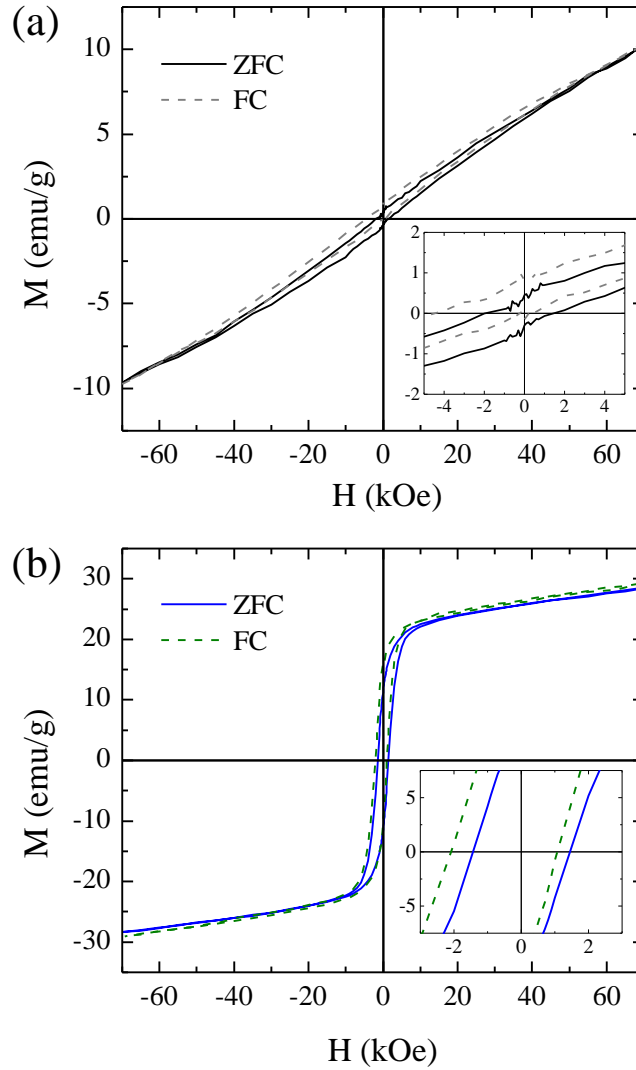


FIG. 4.22 (a) Magnetization curves for the as-deposited sample in ZFC (black lines), and FC at 5 T (grey dashed lines). (b) Magnetization curves for the sample after 10 hours of thermal treatment in ZFC (blue lines), and FC at 5 T (green dashed lines). The insets show a detail of the M-H curves.

Equation 4.4 tends to $C_P = 3Nk_B$, which is a constant value that only depends on the sample mass. This slope variation has two implications, which are in fact related, a heat capacity enhancement that is reduced as the thermal treatments are performed, and an increase of the Debye temperature promoted by microstructural disorder reduction. Heat capacity enhancement has been previously reported [45–47], besides Debye temperature reduction at nanoscaled systems [46].

If we try to fit the Debye model by considering 517.8 K as the Debye temperature for the bulk CoO [48], in the as-deposited state of the sample, the value for the $3Nk_B$ tends to $0.8 \text{ J g}^{-1} \text{ K}^{-1}$, while after several thermal treatments, the C_P value at high temperatures gives $0.7 \text{ J g}^{-1} \text{ K}^{-1}$. It is not possible since sample mass remains unaltered. The lack of a perfect sample prevents us to obtain the Dulong-Petit limit for the CoO by fitting the Debye model. Then, we calculate the number of CoO atoms within a layer of 20 nm

thick, hence we obtain the value of $3Nk_B = 0.7 \text{ J g}^{-1} \text{ K}^{-1}$. With this value we determine the Debye temperature for the sample deposited at 300 K and after every thermal treatment (Figure 4.23). From the second thermal treatment, and so on, Debye temperature and magnetic entropy increase while heat capacity reduces.

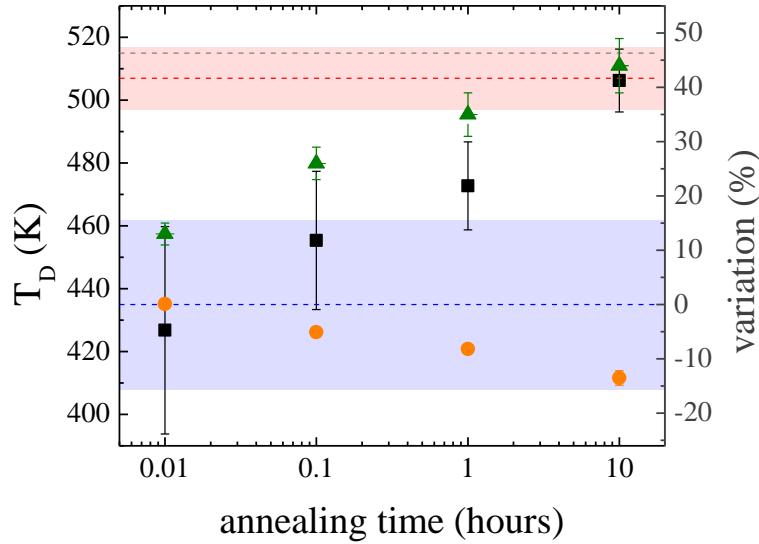


FIG. 4.23 Debye temperature versus the annealing time for the sample deposited at 300 K (black squares). Dashed lines represents the Debye temperature and its error (colored area) for the sample deposited at 300 K (blue), 675 K (red) and for the bulk CoO (grey). On the grey axis it is represented the magnetic entropy increase as a function of the initial value for the sample deposited at 300 K (green triangles), besides the specific heat reduction at $T = 150 \text{ K}$ after different thermal treatments (orange circles).

These results suggest that it is possible to increase the Debye temperature, without modifying apparently the grain size; however the sample microstructure is modified. The most plausible hypothesis is that high temperatures, achieved during thermal treatment, promote the oxygen diffusion through the sample, and as a consequence, the grain boundaries became Co rich. In fact, oxygen diffusion, rather than crystal growth, may be the explanation for the AFM interaction improvement, and even, for the exchange coupling emergence between AFM and FM interfaces. There is also the possibility that the increase in heat capacity is only due to microstructural defects reduction, without oxygen diffusion into the grains. Further investigations are needed to solve this disjunctive.

4.4.3 Microstructure dependence

While in previous Subsections the microstructure was modified either by the deposition temperature or by carrying out specific thermal treatments at high temperatures, in this Subsection we analyze two pairs of samples (6 and 8 nm thick), grown at the same conditions, but with different growth protocols leading to

4. ANTIFERROMAGNETIC INTERACTION IN CoO

remarkable variations in the microstructure. In the procedure different from normal continuous growth, films are deposited in steps of 1 nm, separated by latent periods of 5 minutes during which the deposition is stopped. TEM observations showed that the CoO grain size in these samples is similar to the grain size obtained in 2 nm thick samples prepared by continuous evaporation. The specific heat measured on these two different films is compared in Figure 4.24 to the specific heat measured on films of the same thicknesses, prepared by continuous evaporation. Both the T_N and the specific magnetic contribution are much smaller in films grown by step evaporation and the properties of both films prepared by step evaporation are very similar to those of the normal 2 nm thick samples. In agreement with previous observations [16], our results establish that the microstructure rather than the film thickness controls the magnetic properties.

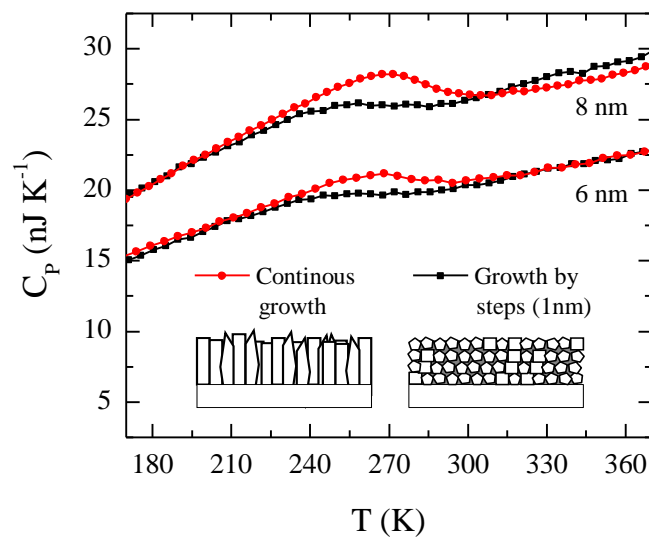


FIG. 4.24 Heat capacity vs temperature of 6 nm and 8 nm CoO films grown by two different methods: continuous growth and step-by-step growth (see text). In the inset: sketches of the microstructure of the films in the two growth processes.

4.5 Conclusions

A deep study of the samples microstructure has been done with the aim to know the influence of growth conditions. A phase diagram is used to perfectly control the crystalline phase deposited, simply by tuning deposition temperature and oxygen partial pressure.

Using quasi-adiabatic nanocalorimetry, we have shown that it is possible to measure the thermodynamic signature of an antiferromagnetic second-order phase transition in a system that is close to the 0D limit. Actually, the observed scaling of the Néel temperature with the nanograin diameter down to 1.5 nm is

characteristic of phase transition in finite 3D systems. The magnetic entropy decreases very significantly as the size of the nanograins is reduced. This observation has very special importance for exchange-bias nanosystems where antiferromagnetic CoO layers are often studied in conjunction with ferromagnetic ones. The technique high sensitivity permits the measurement of T_N for ultrathin single layers with grain sizes down to 1.5 nm.

The magnetic interaction in antiferromagnetic oxides is clearly influenced by grain size and grain boundaries density. Grain boundaries of samples deposited at room temperature act as magnetic dead layers until they are submitted to thermal treatments. These thermal treatments could promote the oxygen diffusion from boundaries to grains, which improves the CoO stoichiometry and the formation of Co-rich clusters. While the antiferromagnetic energy increases, an exchange coupling between antiferromagnetic grains and ferromagnetically coupled boundaries arises. The microstructure evolution with successive annealings is monitored through Debye temperature, which increases as sample microstructure becomes ordered. We state that microstructure, rather than film thickness, controls the magnetic properties in antiferromagnetic oxides.

References

- [1] P. Curie. Lois expérimentales du magnétisme. Propriétés magnétiques des corps à diverses températures. *Ann. Chim. Phys.*, 5:289–405, 1895.
- [2] P. Langevin. Magnetism et theory des electrons. *Ann. Chim. Phys.*, 5:70–127, 1905.
- [3] P. Weiss. La variation du ferromagnétisme avec la température. *Comptes Rendus*, 143:1136, 1906.
- [4] P. A. M. Dirac. The theory of magnetic poles. *Physical Review*, 74(7):817, 1948.
- [5] W. Heisenberg. Mehrkörperproblem und Resonanz in der Quantenmechanik. *Zeitschrift für Physik A Hadrons and Nuclei*, 38(6):411–426, 1926.
- [6] L. Néel. Théorie du paramagnétisme constant; application au manganèse. *C. R. Acad. Sc.*, 203:304–306, 1936.
- [7] L. Néel. Propriétés magnétiques des ferrites: ferrimagnétisme et antiferromagnétisme. *Ann. Phys.*, 3(2):137–198, 1948.

4. ANTIFERROMAGNETIC INTERACTION IN CoO

- [8] K. S. Takahashi, M. Kawasaki, and Y. Tokura. Interface ferromagnetism in oxide superlattices of $\text{CaMnO}_3/\text{CaRuO}_3$. *Applied Physics Letters*, 79(9):1324, 2001.
- [9] F. Nolting, A. Scholl, J. Stohr, J. W. Seo, J. Fompeyrine, H. Siegart, J. P. Locquet, S. Anders, J. Luning, E. E. Fullerton, M. F. Toney, M. R. Scheinfein, and H. A. Padmore. Direct observation of the alignment of ferromagnetic spins by antiferromagnetic spins. *Nature*, 405(6788):767–9, June 2000.
- [10] P. Gambardella, A. Dallmeyer, K. Maiti, M. C. Malagoli, W. Eberhardt, K. Kern, and C. Carbone. Ferromagnetism in one-dimensional monatomic metal chains. *Nature*, 416(6878):301–4, March 2002.
- [11] T. Ambrose and C. L. Chien. Finite-size effects and uncompensated magnetization in thin antiferromagnetic CoO layers. *Physical Review Letters*, 76(10):1743–1746, 1996.
- [12] A. P. Ramirez. Magic moments. *Nature*, 421:483, 2003.
- [13] M. Gruyters. Spin-Glass-Like Behavior in CoO Nanoparticles and the Origin of Exchange Bias in Layered CoO/Ferromagnet Structures. *Physical Review Letters*, 95(7):077204, August 2005.
- [14] K. Binder. Statistical Mechanics of Finite 3-Dimensional Ising Models. *Physica*, 62(4):508–526, 1972.
- [15] E. N. Abarra, K. Takano, F. Hellman, and A. E. Berkowitz. Thermodynamic measurements of magnetic ordering in antiferromagnetic superlattices. *Physical Review Letters*, 77(16):3451–3454, October 1996.
- [16] Y. J. Tang, D. J. Smith, B. L. Zink, F. Hellman, and A. E. Berkowitz. Finite size effects on the moment and ordering temperature in antiferromagnetic CoO layers. *Physical Review B*, 67(5):54408, 2003.
- [17] H. A. Kramers. L'interaction Entre les Atomes Magnétogènes dans un Cristal Paramagnétique. *Physica*, 1(1-6):182–192, January 1934.
- [18] P. W. Anderson. Antiferromagnetism. Theory of Superexchange Interaction. 79(2):350–356, 1950.
- [19] Georg Brauer, editor. *Handbook of Preparative Inorganic Chemistry, Volume 1*. Academic Press, 2nd edition, 1963.

- [20] W. L. Roth. Multispin Axis Structures for Antiferromagnets. *Physical Review*, 111(3):772–781, 1958.
- [21] W. L. Roth. Magnetic Structures of MnO, FeO, CoO, and NiO. *Physical Review*, 110(6):1333–1341, 1958.
- [22] M. D. Reichtin and B. L. Averbach. Tetragonal Elongation in CoO Near the Néel Point. *Physical Review Letters*, 26(24):1483–1485, 1971.
- [23] B. D. Cullity and C. D. Graham. *Introduction to magnetic materials*. Wiley-IEEE Press, 2nd edition, 2008.
- [24] F. J. Romero, J. Jimenez, and J. Del Cerro. Calorimetric investigation on the paramagnetic–antiferromagnetic phase transition in CoO. *Journal of Magnetism and Magnetic Materials*, 280(2-3):257–263, September 2004.
- [25] M. Massot, A. Oleaga, A. Salazar, D. Prabhakaran, M. Martin, P. Berthet, and G. Dhalenne. Critical behavior of CoO and NiO from specific heat, thermal conductivity, and thermal diffusivity measurements. *Physical Review B*, 77(13):134438, 2008.
- [26] D. Bloch, R. Maury, C. Vetter, and W. B. Yelon. Order-parameter and the discontinuous antiferro-paramagnetic transition in manganese oxide. *Physics Letters A*, 49(5):354–356, October 1974.
- [27] N. N. Greenwood and A. Earnshaw. *Chemistry of the Elements*. Butterworth - Heinemann, 1997.
- [28] W. H. Meiklejohn and C. P. Bean. New Magnetic Anisotropy. *Physical Review*, 102(5):1413–1414, 1956.
- [29] J. Nogues and I. K. Schuller. Exchange bias. *Journal of Magnetism and Magnetic Materials*, 192(2):203–232, 1999.
- [30] V. A. de la Peña O’Shea, I. de P. R. Moreira, A. Roldán, and F. Illas. Electronic and magnetic structure of bulk cobalt: the alpha, beta, and epsilon-phases from density functional theory calculations. *The Journal of Chemical Physics*, 133(2):024701, July 2010.
- [31] A. Sharma, R. Brajpuria, S. Tripathi, and S. M. Chaudhari. Study of annealed Co thin films deposited by ion beam sputtering. *Journal of Vacuum Science & Technology A*, 24(1):74, 2006.

4. ANTIFERROMAGNETIC INTERACTION IN CoO

- [32] B. A. Movchan and A. V. Demchishin. Study of the structure and properties of thick vacuum condensates of nickel, titanium, tungsten, aluminium oxide and zirconium dioxide. *The Physics of Metals and Metallography*, 28:83–90, 1969.
- [33] J. R. Anderson, editor. *Chemisorption and Reactions on Metal Films*. Academic Press, New York, 1971.
- [34] H. E. Stanley. *Introduction to Phase Transitions and Critical Phenomena*. Oxford University Press, 1971.
- [35] L. D. Landau and E. M. Lifshitz. *Statistical Physics, Part 1*, Vol. 5, 1980.
- [36] X. Y. Lang, W. T. Zheng, and Q. Jiang. Size and interface effects on ferromagnetic and antiferromagnetic transition temperatures. *Physical Review B*, 73(22):224444, 2006.
- [37] G. Vallejo-Fernandez, T. Deakin, K. O’Grady, S. Oh, Q. Leng, and M. Pakala. Measurement of the antiferromagnet activity in exchange bias systems. *Journal of Applied Physics*, 107(9):09D709–09D709, 2010.
- [38] V. Baltz, G. Gaudin, P. Somani, and B. Dieny. Influence of edges on the exchange bias properties of ferromagnetic/antiferromagnetic nanodots. *Applied Physics Letters*, 96(26):262505, 2010.
- [39] P. Debye. Zur Theorie der spezifischen Wärmen. *Annalen der Physik*, 344(14):789–839, 1912.
- [40] R Kannan and Mohindar S. Seehra. Percolation effects and magnetic properties of the randomly diluted fcc system $\text{Co}_p\text{Mg}_{1-p}\text{O}$. *Physical Review B*, 35(13):6847–6853, 1987.
- [41] V. S. Gornakov, O. A. Tikhomirov, C. G. Lee, J. G. Jung, and W. F. Egelhoff. Thickness and annealing temperature dependences of magnetization reversal and domain structures in exchange biased Co/Ir–Mn bilayers. *Journal of Applied Physics*, 105(10):103917, May 2009.
- [42] M. Fitzsimmons, B. Kirby, S. Roy, Z-P Li, I. Roshchin, S. Sinha, and I. K. Schuller. Pinned magnetization in the antiferromagnet and ferromagnet of an exchange bias system. *Physical Review B*, 75(21):214412, June 2007.
- [43] J. Nogues, C. Leighton, and I. K. Schuller. Correlation between antiferromagnetic interface coupling and positive exchange bias. *Physical Review B*, 61(2):1315–1317, 2000.

- [44] D. P. Dutta, G. Sharma, P. K. Manna, A. K. Tyagi, and S. M. Yusuf. Room temperature ferromagnetism in CoO nanoparticles obtained from sonochemically synthesized precursors. *Nanotechnology*, 19(24):245609, June 2008.
- [45] J Rupp and R Birringer. Enhanced specific-heat-capacity (c_p) measurements (150 - 300 K) of nanometer-sized crystalline materials. *Physical Review B*, 36(15):7888–7890, 1987.
- [46] Y Y Chen, Y D Yao, S S Hsiao, S U Jen, B T Lin, H M Lin, and C Y Tung. Specific-heat study of nanocrystalline palladium. *Physical Review B*, 52(13):9364–9370, 1995.
- [47] R. Meyer, Laurent Lewis, S. Prakash, and P. Entel. Vibrational properties of nanoscale materials: From nanoparticles to nanocrystalline materials. *Physical Review B*, 68(10):104303, September 2003.
- [48] R. Parthasarathy, P. R. Sarode, and K. J. Rao. Debye temperature of oxides with the NaCl structure. *Journal of Materials Science*, 16:3225, 1981.

5. Silicide formation of Pd₂Si

Most of this Chapter appears published in *Applied Physics Letters* **102** 143111 (2013), and *Applied Physics Letters* **105** 013113 (2014).

In this Chapter we present the study of the Pd₂Si phase formation, starting from thin films of palladium (Pd) onto silicon substrate. The formation kinetics is analyzed from calorimetric curves obtained by using different techniques. With the aim to determine the role of the silicon substrate during silicide reaction, both single crystal silicon (1 0 0) (c-Si) and amorphous silicon (a-Si) are used. The study is completed through the morphological and structural characterization of the samples by micro-X-ray diffraction (μ -XRD), cross sectional transmission electron microscopy (XTEM) and field emission scanning electron microscopy (FESEM) when using c-Si, and by XTEM and *in-situ* synchrotron X-ray diffraction (XRD) when using a-Si. The kinetics of the transformation on c-Si is analyzed at fast heating rates of about 10^4 K/s, while for the reaction of Pd with a-Si we have expanded the heating rate range from 0.1 to 10^5 K/s, to analyze the linearity of the temperature dependence of the activation energies related to silicide formation. The differences in the methodology used to analyze the reaction between Pd and c-Si or a-Si are related to the ability to grow a-Si on a variety of substrates which enables additional calorimetric analysis. The Chapter also includes the use of a kinetic model to fit the calorimetric traces. From this model the most relevant kinetic parameters, i.e. activation energies, associated to the various mechanisms, which control the formation of the silicide, have been calculated.

5.1 Introduction

The comprehension of silicide kinetics between two thin film materials is central to many applications, in relevant areas such as Electronics, Materials Science and Surface Science. The fabrication of nm-size transistors in complementary metal-oxide-semiconductor (CMOS) technology highly depends on the formation of low-ohmic contacts by the reaction between silicon and a thin metallic layer. During the reaction of two materials and, in particular, during the reaction between thin films, metastable phases can be thermodynamically stabilized due to the contribution of interface and surface energies to the total Gibbs free energy of the system. The nature of intermediate phases will also depend on the ratio of elements present in the reaction zone, i.e. thickness of the initial layers. This difficulty highlights the requirement to use a combination of characterization techniques to get a full understanding of the reaction mechanisms and phase formation. An additional consideration in silicide formation is the continuous decrease of the dimensions of electronic devices, which imposes severe requirements from the point of view of processing to minimize interdiffusion and cross-talk effects between the different regions of the device. As the dimensions of the devices are reduced to the nm-scale, the thermally induced solid-state formation of the silicide phase becomes extremely dependent on process parameters and material characteristics, such as metal thickness, substrate orientation, or surface roughness [1–3]. Technological applications of silicide materials impose that fast heating processes are thus being considered to reduce the adverse impact of more traditional long-thermal treatments. Techniques such as rapid thermal annealing (RTA, with heating rates, $\beta \sim 100$ K/s) or pulsed laser annealing (PLA, $\beta \sim 10^6 - 10^7$ K/s) are gaining widespread use in nm-scale devices because of their superior control in the activation and localization of dopants [4]. PLA is also being tested for Si-rich silicide formation [5] because of the reduced thermal budget relative to those of conventional furnace annealing approaches.

The mechanisms of silicide formation, including diffusion plus reactions, and their activation energies are relatively well described in isothermal annealings or moderate temperature up scans for a variety of silicides [6, 7]. However, the dependence on ramp rate is not at the same level of maturity and further investigations are required. The activation energies linked to intermediate reactions between a metal and a semiconductor are often considered to be Arrhenius when the explored temperature interval of the reaction occurs within few tens of degrees. In most studies of thin film reactions involving thermodynamic or structural parameters the heating rate achievable is limited by the experimental technique, i.e. by the temporal resolution to obtain accurate data. Traditional heating rates in calorimetric studies are below 5 K/s. In the case of *in-situ* XRD analysis, the scanning rate is limited by the signal-to-noise ratio of the XRD spectra and often reaction rates are limited to 100 K/s.

5. SILICIDE FORMATION OF Pd₂Si

Calorimetry is a well-known technique to explore the kinetics and thermodynamics of phase formation between pairs of materials when they are submitted to thermal treatments [8], in thin multilayered systems [9, 10], and also amorphous and polycrystalline thick layers on substrates [11]. If the solids are in thin film form the amount of materials is typically too small to be directly measured by conventional differential scanning calorimetry (DSC). A useful strategy such as using multilayers consisting of many repetitions of the fundamental A/B stack is often used to increase the analyzed mass and resolve the calorimetric transitions [12]. However, this approach does not realistically reproduce the systems at use in real applications, which often involve single layers or bilayer [13]. In this respect, phase transformations from calorimetry are often studied isothermally or with moderate heating rates around 10 K/min. However, analysis at faster heating rates, are becoming more important due to the decrease of device dimensions, as stated previously. The use of very thin films and faster heating ramps in silicide formation can modify the temperature of the reaction and may, as well, introduce changes in the physical-chemical mechanisms that control the development of the intermediate phases. Therefore, it is questionable if conventional DSC studies on thick films at close to 1 K/s may be informative enough of reaction processes occurring at the much higher heating rates relevant for nm-size chip contacts. As a consequence, it is relevant to check if different factors control the kinetics in fast thermal processing. Extension of previous studies to analyze intermediate phase sequence and formation at higher heating rates to mimic real processing will thus provide a better understanding about the phase formation by reactive diffusion in thin films and devices [14]. The use of novel nanocalorimetric techniques eases the study of phase formation at ultrafast heating rates mimicking the conditions that will be used in future technologies to create the contact gates in the new generation of nanoscale transistors. Additionally, increasing the heating rate gives access to the analysis of smaller amounts of materials, as shown in Chapter 3. It is clear then, that the use of membrane-based calorimetry enables a level of exploration not attempted before. Only recently, several groups worldwide have developed membrane-based calorimetric techniques with enough resolution to allow these studies [14–18]. First measurements by fast scanning nanocalorimetry on Ni/amorphous Si thin films at heating rates of 10⁵ K/s have been reported [19], but no comparable data exist yet on the more interesting reaction between an ultrathin metal layer and monocrystalline Si at such fast heating rates.

The silicide reaction has often been analyzed by *in-situ* XRD to monitor sequential phase formation during a temperature excursion or isothermal measurements. At faster heating rates, synchrotron radiation offers a promising route to *in-situ* characterize the silicide reaction [20, 21] and can be combined with resistive or optical measurements to obtain complementary information on the reaction [22, 23]. Recently, a study of Pd₂Si formation between 50 nm thick films of Pd with a thin monocrystalline Si substrate was carried out by conventional DSC at heating rates ranging from around 0.4 to 1.7 K/s [24]. An example

with important implications in nowadays microelectronic industry is the reaction between an ultrathin metal layer and silicon to form low-resistive materials to be used as metal gates. NiSi [25, 26], or more recently Ni(Pt)Si [27], are the silicides of choice for actual sub-nm devices. The kinetics and thermodynamics of formation of those silicides is often complex due to the creation of intermediate metastable phases before the stable one sets in. For instance, NiSi formation starting from 13 nm Ni on single-crystalline Si is preceded by a mixture of Ni₂Si and Ni₃Si₂ phases [28]. We use Pd and Si as a model system, since only one stable phase, hexagonal Pd₂Si, can form below 800 °C [29, 30].

It is also important to remark that calorimetry lacks the structural information required to correlate the observed thermodynamic phase transitions to structural changes in the sample. For this reason, simultaneous X-ray scattering and calorimetry experiments using standard-type calorimeters have been successfully attempted in the past [31, 32]. However, standard calorimeters are often not well suited for complementary XRD analysis. The field of simultaneous synchrotron and complementary techniques to characterize phase formation is gaining attention in the scientific community as a way to fully characterize the system under study [33–36]. The new generation of wide angle and fast detectors is also helping to monitor phase changes at faster rates and with unprecedented spatial and temporal resolution opening a vast field of exploration in materials science. In this respect, membrane-based calorimeters provide a unique platform to combine the easy thin-film geometry for X-ray characterization with the high sensitivity of the nanocalorimeter to resolve phase transitions in samples of mass as small as few ng [37, 38]. In this Thesis we complement the calorimetric data by *in-situ* synchrotron radiation analysis of phase formation and structural analysis by transmission electron microscopy. Additionally, in this work, we use a combination of calorimetric techniques, from standard DSC to fast-scanning nanocalorimetry, to evaluate the kinetic and thermodynamic parameters that control the formation of Pd₂Si in a very wide heating rate interval.

5.2 Experimental

The Pd layers (12 nm thick in most calorimetric experiments), are grown from pure Pd pellets (99.95% purity) on c-Si or a-Si surfaces. The samples are grown at room temperature and a pressure of 10⁻⁶ mbar with a growth rate of 1.0 ± 0.1 Å/s. Nanocalorimetric measurements are carried out *in-situ* at a base pressure of 10⁻⁶ mbar, and also using the specific setup for simultaneous XRD characterization. The main particularities to each Si substrate are described in their specific section.

5.2.1 Calorimetric approach

The silicide reaction of ultrathin films in the very large heating rate interval proposed here (from 0.1 to 10⁵ K/s) is analyzed by two different setups and three methodologies to obtain accurate power vs. temperature data. At slow heating rates, from 0.1 to 1 K/s, the calorimetric scans are recorded with a Perkin Elmer DSC 7, while from 10 to 10⁵ K/s the measurements are done using membrane-based nanocalorimeters. In particular, at rates above 2x10⁴ K/s, we use quasi-adiabatic nanocalorimetry (QAnC) [39, 40]. The intermediate heating rate regime, from 10 to 10⁴ K/s, is achieved using saw-tooth nanocalorimetry (STnC) current-time profiles [41]. In this range, heat losses are important, and we only access an apparent heat capacity. In this case the baseline correction was performed by measuring a second up scan. Both techniques are carefully described in Section 3.2 *Principle of operation*. The temperature calibration of the nanocalorimeters was done after the silicide formation by the dynamic method, described in Subsection 2.1.2 *Nanocalorimeter calibration*.

5.3 Pd₂Si formation on Si (1 0 0)

5.3.1 Preparation of Pd/c-Si samples

Thin film nanocalorimetric sensors with a sensitive area made of single-crystalline Si (1 0 0) are micro-fabricated starting from silicon on insulator (SOI) wafers following a procedure described elsewhere [42]. The native oxide, which covers the surface of the 300 nm thick c-Si, is etched with a 5% HF solution to obtain an H-terminated Si surface previously to place the nanocalorimeters in the high vacuum chamber.

The heat capacity measurements are done in a heating rate range of 10⁴ K/s, for this reason only QAnC is used. The measurements consist of the following consecutive steps: (a) 100 successive scans up to temperatures around 850 K to obtain the initial offset in heat capacity between the empty calorimetric cells (baseline correction), (b) Deposition of 12 ± 1 nm thick Pd films, (c) Annealing of the Pd layer at 375K for 15 min, (d) Calorimetric scan up to 850 K to complete the Pd-Si reaction, and (e) 100 consecutive temperature scans after the silicide reaction is completed. The second, postreaction, scan is used for baseline subtraction in order to obtain accurate data to model the calorimetric traces. Several heating rates were used in step (d) to extract kinetic information of the intermetallic reaction on different samples of identical thickness. Since the reaction is irreversible, the averaging of multiple scans, widely used in fast scanning nanocalorimetry to improve the signal-to-noise ratio, is not useful and the first scan

after Pd deposition contains all the valuable information of the silicide reaction.

The morphological and structural characterization of the samples is performed by XTEM (Jeol JEM-2011, with resolution point between 0.14 - 0.19 nm, operated at 200 kV), FESEM (Carl Zeiss Merlin, operated at 1 kV), and μ -XRD (Bruker D-8 Advance system coupled with a Gadds detector with Cu K $_{\alpha}$, $\lambda = 1.54 \text{ \AA}$). The preparation of the samples for the XTEM characterization is not obvious due to the membrane-based nature of the nanocalorimeter. The devices are sandwiched using PELCO Eponate 12 Kit with BDMA and then they are cut, on the sample zone, into slices by means of a Leica EM UC6 Ultramicrotome.

5.3.2 Results and Discussion

Figure 5.1 shows the calorimetric experimental data for a sample measured at $3 \times 10^4 \text{ K/s}$. The onset of the silicide reaction occurs at $\sim 9 \text{ ms}$, where a large variation of the slope in the differential voltage signal is observed. The growth of the Pd layer slightly delays the temperature of the sample calorimetric cell with respect to the empty reference cell up to the onset of the reaction [Figure 5.1(b) and inset]. The acceleration in the temperature evolution is more clearly identified in Figure 5.1(c) that shows the increase of the heating rate as a consequence of the exothermic reaction in the sample during the first scan (red curve). Finally, the specific heat capacity is obtained by applying corrections due to different addenda and heating rates (b) between the sample and the reference cell [Figure 5.1(d)]. It is clearly observed that the Pd₂Si is completely formed before 730 K during the first pulse and no more exothermic reactions are observed on successive scans.

The subtraction of the 1st and 2nd scans for the three heating rates results in the calorimetric traces shown in Figure 5.2(a). Integration of the exothermic peaks yields an enthalpy of formation $\Delta H_f = 260 \pm 20 \text{ J/g}$ in agreement with previously reported values $260.2 \pm 10.1 \text{ J/g}$ [43] and $259.0 \pm 9.7 \text{ J/g}$ [44] for Pd₂Si formation. Similar agreement was found in the analysis of the reaction between Ni and a-Si by fast-scanning calorimetry and DSC [14, 19]. Our results do not exclude, however, that thinner films may have variations in the enthalpy of formation due to size effects.

On the other hand, the Kissinger analysis indicates an apparent activation energy $E_{ap} = 0.40 \pm 0.05 \text{ eV}$ greatly differing from the activation energy of $\sim 0.8 \text{ eV}$ extracted from the DSC data of Hoummda et al. [24] at low heating rates (in the range 0.4 - 1.7 K/s) with 50 nm thick Pd layers. To gain more insight into the specific thermodynamic processes playing a role in the formation of the silicide and

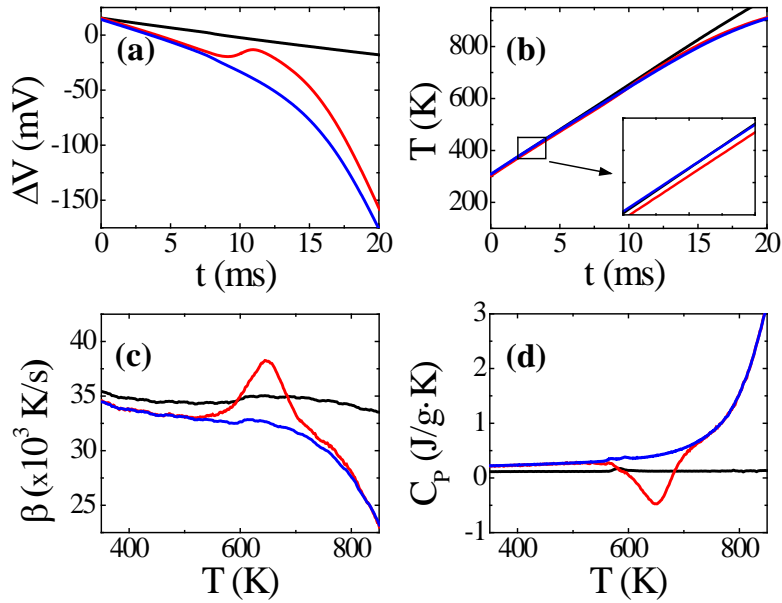


FIG. 5.1 Calorimetric data obtained during an up scan at a heating ramp at $\sim 3 \times 10^4$ K/s till 850 K. Black curve: difference between empty calorimeters; red curve: difference between sample (1st scan) and reference; blue curve: difference between sample (2nd scan) and reference cell. (a) Voltage difference as a function of time. (b) Temperature of the sample calorimetric cell versus annealing time. (c) Heating rate (b) vs. temperature during calorimetric scans. (d) Specific heat capacity data as a function of temperature.

their activation energies we carry out a detailed simulation of our calorimetric data. Our first attempt consists of fitting the experimental data shown in Figure 5.2 using a linear-parabolic model to match calorimetric traces measured at slower heating rates [24]. However, the abrupt onset of the peaks in Figure 5.2(a) could only be obtained by introducing the nucleation of the silicide phase. The differences between both models can be appreciated in Figure 5.2(b). The proposed model considers the formation of a single phase, Pd_2Si , following two main processes: nucleation and lateral growth of Pd_2Si along the initial interface and vertical growth of the silicide phase. Its main features have been previously described in other systems [45, 46]. Briefly, the fraction of silicide phase that is formed at the Pd/Si interface can be written within the Kolmogorov - Johnson - Mehl - Avrami - Erofeev (KJMAE) model as (see Subsection 5.3.3 *KJMAE kinetic model*)

$$x_L(T) = 1 - \exp(-x_L^{ext}(T)) \quad (5.1)$$

where

$$x_L^{ext}(T) = \pi \int_{T_0}^T \frac{I(T')}{\beta(T')} \left\{ \int_{T_0}^{T'} \frac{U_L(T'')}{\beta(T'')} dT'' \right\}^2 dT' \quad (5.2)$$

where both the nucleation rate, I , and the lateral growth rate, U_L , have an Arrhenius temperature dependence, β is the heating rate which is temperature dependent, and the initial nuclei have been assumed to be cylinders with negligible radius r_0 and height L_0 . The vertical growth of the new phase can be either reaction or diffusion controlled, following the growth laws, $L^2 \propto Dt$ or $L \propto Kt$, respectively, where

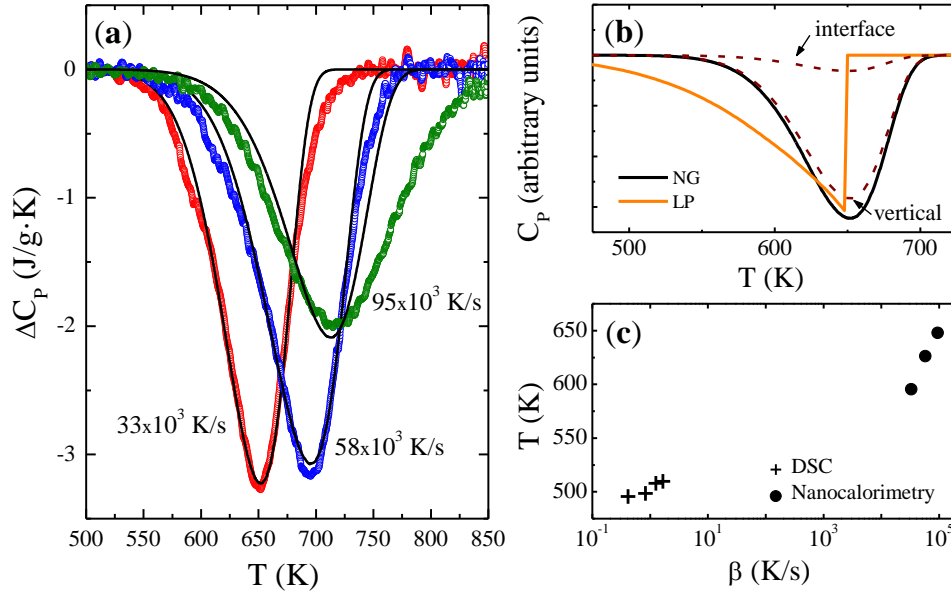


FIG. 5.2 (a) Specific heat capacity difference between 1st and 2nd scan vs. Temperature for 12 nm Pd samples measured at three different rates. The continuous lines correspond to the calculated data using the nucleation and growth model. (b) Comparison between linear-parabolic growth (LP) and nucleation and growth models (NG) (see Subsection 5.3.3 *KJMAE kinetic model* for further details). The dotted lines within the NG peak are the interface and vertical contribution to the calorimetric peak. (c) T-HR-T diagram for the Pd₂Si formation compared with DSC data from Ref. [24].

L is the thickness of the Pd₂Si film, D is an effective diffusion coefficient that does not discriminate in which direction is the new film growing (i.e., consuming Pd or Si) and K is the interfacial reaction constant. The ΔC_p can be calculated as the temperature derivative of the total transformed fraction, x , multiplied by the reaction enthalpy, ΔH , $\Delta C_p(T) = \Delta H dx/dT$. The calculation is performed in a discrete way for every nucleus. When a certain fraction of Pd₂Si has vertically grown enough to reach the final thickness of the silicide layer, L_f , it stops growing. This approximation produces a smooth ending of the calorimetric peaks provided the nucleation/lateral growth along the interface remains the limiting mechanism. The presence of a single peak is related to the significant overlap between the interfacial nucleation and growth and the vertical growth [Figure 5.2(b)]. The model reproduces satisfactorily the calorimetric traces measured at heating rates 33×10^3 K/s and 58×10^3 K/s, but fails to explain the curve width measured at 95×10^3 K/s. The best fit for the experimental data have been obtained using the values shown in Table 5.1.

The activation energy obtained from the Kissinger method, 0.4 eV/at, is compatible with the apparent activation energy for the reaction at the interface, E_A . Therefore, our model suggests that the thermodynamic processes controlling the formation of Pd₂Si at the very fast rates used in this work are related to the nucleation and lateral growth during the initial stages of growth. The results of our fast scanning

5. SILICIDE FORMATION OF Pd₂Si

TABLE 5.1 Values used for the modeling of the calorimetric signal. Uncertainties are estimated from the tolerance to produce comparable χ^2 in the fit.

$(IU_L^2)^{1/3} = A_0 \exp(-\frac{E_A}{k_B T})$
$A_0 = (4.0 \pm 0.5) \times 10^5$ nuclei/s
$E_A = (0.38 \pm 0.04)$ eV/at
$D = D_0 \exp(-\frac{E_D}{k_B T})$
$D_0 = (0.05 \pm 0.04)$ cm ² /s
$E_D = (1.00 \pm 0.20)$ eV/at
$L_0 = (2 \pm 1)$ nm, $L_f = (20 \pm 1)$ nm

nanocalorimetry experiments and those already reported by conventional DSC are summarized in the temperature-heating rate-transformation (T-HR-T) diagram shown in Figure 5.2(c). In this T-HR-T diagram, the temperature needed to achieve $\sim 10\%$ volume fraction of Pd₂Si (or ~ 2.2 nm thick Pd₂Si) is plotted as a function of the heating rate. To fit the data from Ref. [14], an initial interlayer of palladium silicide of thickness 4 nm had to be added to the model in accordance with the finding that sputtered Pd films on Si form an intermediate layer during the deposition process [47]. These data highlight the difference in the transformation mechanism observed between conventional DSC on sputtered Pd layers and fast-scanning nanocalorimetry on Pd films grown by electron beam evaporation at room temperature. The change in the activation energies could originate from a true change of mechanism induced by the large variations in heating rate or from differences in the initial surface state of the Si wafer. The formation of a thin SiO₂ layer on the Si surface during the initial measurement protocol (baseline determination) may inhibit the initial reaction at almost room temperature between Pd and Si, retarding the nucleation of the new phase and, enhancing the overlap of the calorimetric traces associated to the nucleation and growth and the vertical growth of the silicide phase as shown in Figure 5.2(b). XTEM observations have not revealed the presence of the oxide at the interface between Pd₂Si and Si, however, we do not rule out the possibility of an oxide mediated formation of the silicide phase, as has been observed in other investigations [48, 49].

The FESEM image shown in Figure 5.3(a) corresponds to the surface of a sample heated up to 850 K at 33×10^3 K/s. The surface is smooth and contains microcracks oriented parallel to the Si (001) planes. The presence of cracks at the surface may be related to built-in stresses during the silicide growth. When the sample is cycled many times [Figure 5.3(b)], the microstructure dramatically changes by generating a high density of protrusions and increasing the roughness of the surface. The images obtained using the backscattered electrons (BSE) show that substantial cycling introduces inhomogeneities in composition

which correspond to areas with different Pd-Si ratios [inset of Figure 5.3(b)]. The agglomeration of Pd₂Si is well documented for isothermal reaction studies of Pd on Si (0 0 1) [30]. Our results show that fast heating reduces Si segregation and yields smoother films which may be advantageous for chip interconnections. The XTEM images (Figure 4) confirm the roughness of the samples after substantial cycling. Electron diffraction (ED) performed on film section [Figure 5.3(c), inset] corroborates the formation of the Pd₂Si hexagonal structure (PDF 00-019-0893). No evidence of free palladium is detected. ED with almost discrete spots indicates a preferred orientation of the grains. The μ -XRD pattern [Figure 5.3(c)] confirmed the preferred orientation of the Pd₂Si layer along the [0 0 ℓ] direction, as 0 0 8 reflection peak presents a larger intensity than that expected when compared with the powder diffraction pattern. Also, no reflections corresponding to the palladium were observed, confirming the consumption of the whole Pd layer during the process.

5.3.3 KJMAE kinetic model

The initial reaction stage is assumed in this model as nucleation along the interface which grows in the plane of the original interface by increasing in radius. Impingement effects between nuclei are accounted for by the Avrami expression (Equation 5.1). Or, equivalently, when heating at a rate $\beta(T)$,

$$x_L^{ext}(t) = \pi \int_{t_0}^t I(\tau) \left\{ r^* + \int_{\tau}^t U_L(t') dt' \right\}^2 d\tau \quad (5.3)$$

where the initial radius of the critical nuclei, r^* , may be neglected, leading to Equation (5.2). The thickening of the Pd₂Si layer can be quantitatively described by either a diffusion-limited or reaction controlled growth. So, the product layer growth is described by

- $\frac{dL}{dt} = \frac{D}{2L}$, diffusion-controlled growth
- $\frac{dL}{dt} = K$, reaction-controlled growth

where D is an effective diffusion coefficient and K is an effective reaction constant. Combining the initial nucleation-lateral growth and the vertical growth mechanisms, under scanning up in temperature at a rate $\beta(T)$, the reaction rate is given by $\frac{dx}{dT} = \frac{1}{L_f} \frac{dL}{dT}$, with $\frac{dL}{dT} = L_0 \frac{dx_L}{dT} + \int_{T_0}^T \left[\frac{dx_L}{dT} \right]_T \theta(T', T) dT'$

$$\text{where } \theta(T', T) \begin{cases} = \left[\frac{dL_V}{dT} \right]_T, & \text{if } L_V(T', T) = L_0 + \int_T^{T'} \frac{dL}{dT} dT'' < L_f \\ = 0, & \text{if } L_V(T', T) \geq L_f \end{cases}$$

The first term in the right hand side of this last equation accounts for the thickening rate due to new emerging nuclei, and the second term adds the rate of increase in vertical length at T of all the nuclei

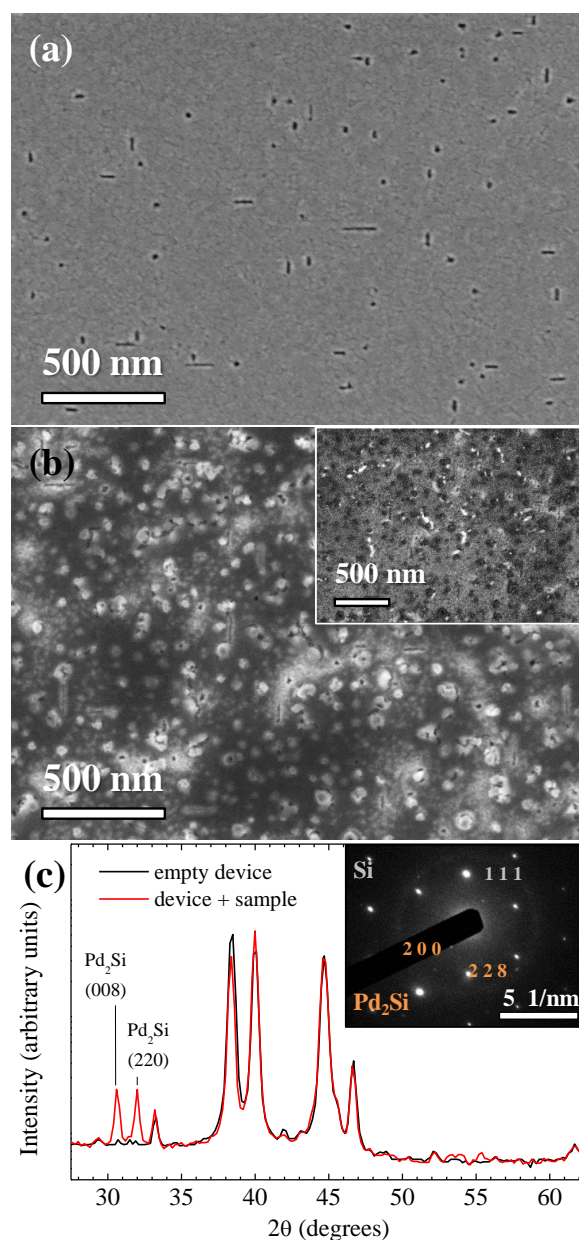


FIG. 5.3 (a) FESEM image of a sample fast ramped up to 850 K. (b) FESEM image of a sample after multiple fast scans to 850 K. Inset: BSE image showing compositional inhomogeneities. (c) μXRD pattern of sample shown in (b), the pattern of the empty nanocalorimeter is shown for comparison. Inset: ED pattern; orange reflections correspond to Pd_2Si sample, grey reflections to Si (100) substrate.

created at any intermediate temperature T' with $T_0 \leq T' \leq T$ (provided the Pd reactant is not exhausted).

The nucleation and growth model is very useful when two maxima in the reaction rate occur during the formation of a single product phase. In our experiments no such two maxima are observed. In spite of this the calorimetric traces are better fitted with this model. The difficulty to nucleate the product phase leads to a significant overlap between the maxima associated with the interface nucleation and lateral growth and the vertical growth. Once the nuclei are formed the acceleration in the reaction rate is higher

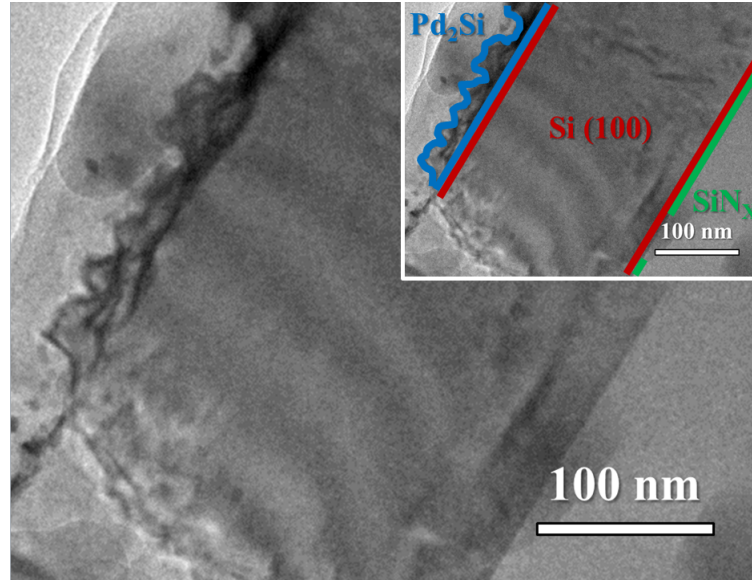


FIG. 5.4 Cross sectional TEM image which shows the roughness of the Pd₂Si film after hundreds of cycles. Inset: schematic of the XTEM image showing the distribution of the different layers that are observed, corresponding to the sample and the calorimetric device.

than that predicted in the linear-parabolic model [as shown in Figure 5.2(b)]. From the nucleation and growth model we see that the growth of the new phase in the vertical direction is orders of magnitude faster than along the interface (see Figure 5.5). The formation of the new phase is therefore limited by the nucleation and growth along the interface, and as soon as new nuclei form, they start growing perpendicular to the interface. Since no limitation is found in the vertical growing rate, the use of a fully linear or parabolic or a mixed linear-parabolic model in the growth does not significantly change the calorimetric trace.

The amount of new phase has been calculated for a heating rate, β of 35×10^3 K/s, and a temperature step, ΔT of 0.2 K, using the following equations

- Linear vertical growth: $\Delta d = K \cdot \Delta T / \beta$
- Diffusive controlled: $\Delta d = (D \cdot \Delta T / \beta)^{1/2}$
- Lateral growth: $\Delta d = (IU_L^2)^{1/3} \cdot (\pi r^2)^{1/2} \cdot \Delta T / \beta$

5. SILICIDE FORMATION OF Pd₂Si

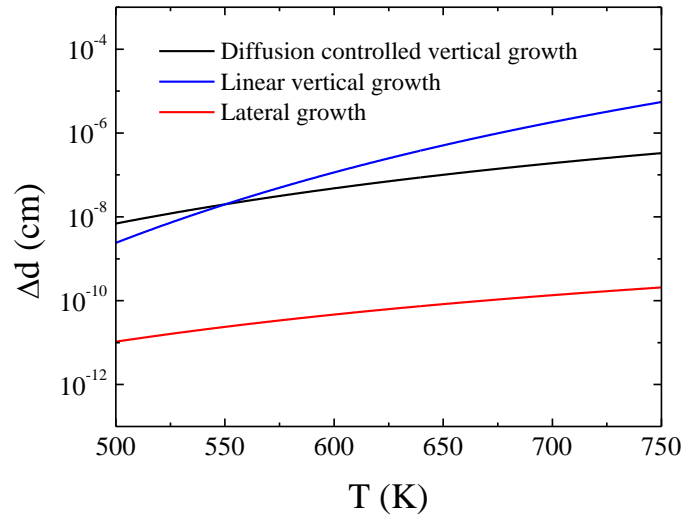


FIG. 5.5 New phase that would form as a function of temperature at the interface, and on the vertical direction in case of having a parabolic (diffusion controlled) or a linear regime.

5.4 Pd₂Si formation on amorphous Si

5.4.1 Preparation of Pd/a-Si samples

For the a-Si substrate, three heating rate regions are well-defined and they impose the use of different calorimetric techniques. The range from 0.1 to 1 K/s is covered by DSC and we use aluminum (Al) foil as a substrate, while for the heating rate range from 10 to 10⁴ K/s we use STnC, and thereafter QAnC.

Thin films of a-Si and Pd are sequentially grown on aluminum (Al) foil or onto the nanocalorimeters. The Al foil is previously covered by a thin SiO₂ layer to prevent interaction with the a-Si layer during heat treatments in the DSC. The foil is then folded and introduced in the DSC pan, allowing a net mass of Pd/a-Si of ~0.1 mg. For both STnC and QAnC, samples are deposited onto nanocalorimeters following the same procedure than for the DSC samples, without previous SiO₂ deposition. Given the initial thickness of the Pd and a-Si layers, the product of the reaction will consist on ~20 nm of Pd₂Si, with a slight excess of Si after the reaction is completed.

The structural and morphological analysis of the samples is done by XRD (Philips X'Pert, Cu K_α source at $\lambda = 1.54 \text{ \AA}$) and XTEM, and as in the monocrystalline silicon case, the samples are prepared following the procedure described above. For standard X-ray characterization multilayers consisting of 10 periods of [12 nm Pd / 15 nm a-Si / 30 nm SiO₂] were grown. *In-situ* X-ray diffraction measurements were carried out at the MSPD beamline of the ALBA Synchrotron Light Facility at Barcelona directly onto

calorimetric chips. To increase the signal-to-noise ratio of the synchrotron data during the heat treatment, the thickness of the layers was slightly increased to 75 nm a-Si + 60 nm Pd, keeping the same compositional ratio as in the ultrathin stack. In this case, upon temperature rise and completion of the reaction, a thin film of Pd₂Si around 100 nm thick is formed leaving a silicon excess of approximately 30 nm.

5.4.2 Results and Discussion

In Figure 5.6 we show the calorimetric measurements covering the heating rate interval from 0.1 to 10⁵ K/s. The curves are normalized to their maximum intensity for the sake of clarity [Figures 5.6(a) and 5.6(b)]. The calorimetric traces show two broad exothermic features which shift towards higher temperatures as the heating rate increases. Only in the curve obtained at 10 K/s, using STnC [Figure 5.6(b)], the first exothermic jump is not resolved. This is the result of the lower sensitivity at these low heating rates. An extensive structural and calorimetric study reveals that the two broad exothermic jumps, observed in Figure 5.6, are composed of four calorimetric peaks associated to different mechanisms of transformation, producing most likely a single phase, Pd₂Si (see Subsection 5.4.3 *Calorimetric and structural analysis* for further information on the nature and microstructure of the phases). The nature of the low temperature broad change on heat capacity is inferred by analyzing the influence of several mild heat treatments to the calorimetric signal. These measurements confirm that the first exothermic jump corresponds to intermixing of Pd and a-Si to build up an amorphous/nanocrystalline layer at the interface followed by nucleation of Pd₂Si along the Pd/a-Si interface. This is in agreement to a significant number of previous reports that attribute the presence of the first feature to nucleation barriers that control the initial phase formation [9]. The second broad exothermic jump corresponds to both the a-Si crystallization (x-Si) and the vertical growth of the Pd₂Si phase [see Figure 5.6(a) inset]. In fact, the large enthalpy associated with the DSC and QAnC calorimetric traces [Figures 5.6(a) and 5.6(c)] with respect to pure Pd₂Si formation clearly indicates other processes are active in this temperature range. The enthalpy of the complete reaction at the fastest rates is 93 μJ, which includes 18 μJ due to intermixing at the interface, 12 μJ as a result of the crystallization of 11 nm (~ 26 ng) of a-Si [50], and 63 μJ due to the formation of 180 ng of Pd₂Si [51].

To gain more insight into the mechanisms that control the phase transformation in the whole temperature interval, we use the Kolmogorov - Johnson - Mehl - Avrami - Erofeev (KJMAE) formalism to fit the calorimetric traces [45, 46]. For the sake of clarity, we only include fitting curves for the highest heating rate of every measurement technique (solid orange lines in Figure 5.6). The complete set of fittings and the equations used to describe the main processes are described in detail in Subsection 5.4.4 *KJMAE*

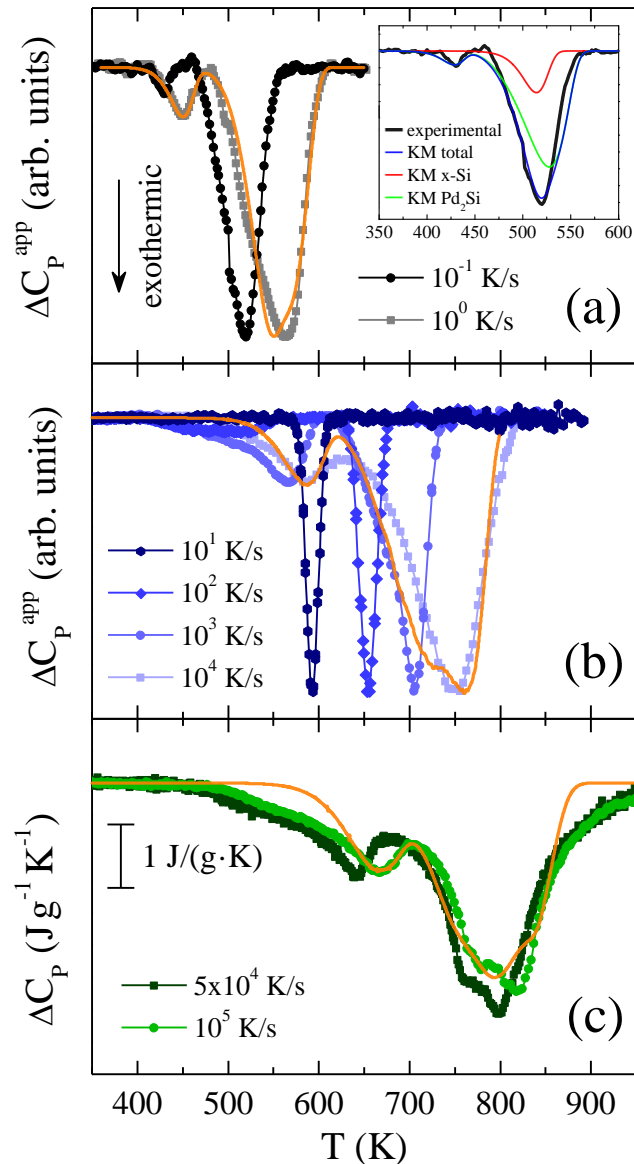


FIG. 5.6 Calorimetric data of the silicide reaction. Apparent heat capacity vs. temperature measured with: (a) DSC at 0.1 and 1 K/s, and (b) with STnC methodology at intermediate heating rates from 10 to 10^4 K/s. (c) Specific heat as a function of temperature obtained at 5×10^4 and 10^5 K/s. The solid orange lines correspond to the calculated data using the KJMAE formalism. The inset in (a) shows the experimental data for the sample measured at 0.1 K/s and the fitting curves obtained from the kinetic model (KM) showing the Pd₂Si formation (green line) and the a-Si crystallization (red line).

kinetic model. The kinetic model incorporates the following processes: i) nucleation of Pd₂Si within the Pd_xSi_{1-x} interfacial region, ii) a-Si crystallization through a growth front from the interface and iii) vertical growth of Pd₂Si. Note that the kinetic model does not include the intermixing reaction. The crystallization of a-Si is catalyzed by the presence of the Pd₂Si phase and therefore occurs at lower temperatures than expected for pure Si, in agreement with many previous reports [52, 53]. According to the kinetic model the crystallization of a-Si and the vertical growth of Pd₂Si are fully overlapped [inset

Figure 5.6(a)].

The analysis and interpretation of the temperature evolution of those exothermic events is the main outcome of this study. The general trend can be rapidly appreciated from Figure 5.6. As the heating rate is increased up to 10^5 K/s the onset and maximum of the peaks shift to higher temperatures as expected for thermally activated processes. To obtain a first insight we use a simplified methodology, the Kissinger plot (Figure 5.7), to estimate the average activation energy of the transformation during the heating ramp [54]. We consider only two main processes and average values of the heating rate, since in STnC and QAnC methodologies the heating rate is not constant throughout the measurement when silicide formation occurs.

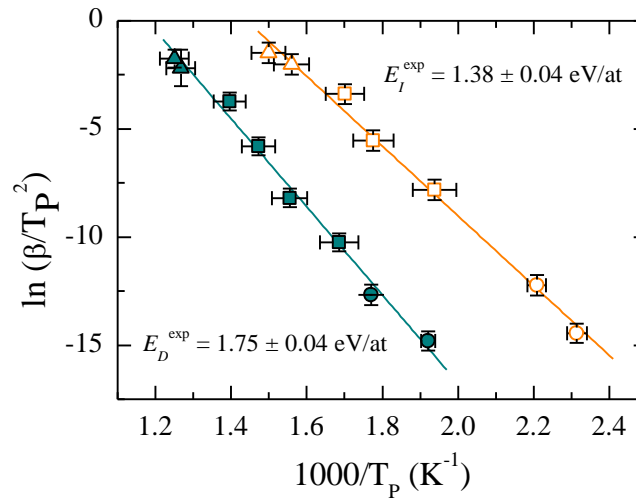


FIG. 5.7 Kissinger plot for the first (open symbols) and second (filled symbols) exothermic peaks. Data obtained from QAnC at fast heating rates (triangles), from conventional DSC at slower rates (circles), and from STnC at intermediate heating rates (squares). Continuous lines represent best fits to the data which yield the activation energies.

As illustrated in Figure 5.7, both peaks exhibit a linear behavior in the whole temperature interval with activation energies of 1.38 ± 0.04 eV/at for the first peak and 1.75 ± 0.04 eV/at for the second one. This average energy values are slightly higher than those previously reported by Homma et al. [55] in couples of Pd/a-Si:H, where an activation energy of 1.1 eV/at for a reaction-limited Pd₂Si formation and 1.4 eV/at for a diffusion-limited growth was found. Although it is normally assumed that Pd and Si fluxes are coupled and both contribute to Pd₂Si growth, the activation energy evaluated here for the second peak coincides with the value of 1.7 eV/at found for Si mobility through polycrystalline Pd₂Si [56].

Table 5.2 highlights the excellent agreement between the activation energies obtained for the nucleation and vertical growth of Pd₂Si using the kinetic modeling and those obtained using the Kissinger methodology. The difference between the simulated data and the experimental calorimetric traces in the low

5. SILICIDE FORMATION OF Pd₂Si

TABLE 5.2 Activation energies for the Pd₂Si nucleation (E_I), Pd₂Si vertical growth (E_D) and a-Si crystallization (E_U) obtained from the kinetic model (KJMAE formalism) and experimentally (Kissinger method). L_T corresponds to the final thickness of the Pd₂Si film.

	KJMAE formalism	Kissinger method
E_I	(1.38 ± 0.05) eV/at	(1.38 ± 0.04) eV/at
E_D	(1.81 ± 0.05) eV/at	(1.75 ± 0.04) eV/at
E_U	(1.72 ± 0.05) eV/at	
L_T	(20.3 ± 2.0) nm	

temperature region of Figure 5.6 highlights the increased importance of the initial interdiffusion as the heating rate increases. Interestingly, the ratio between the areas associated to the two transformation mechanisms (nucleation at the interface and vertical growth) involving Pd₂Si is not constant and shows a clear dependence with the heating rate. The variation can be easily inferred from Figure 5.6. The fastest the heating rate is, the higher is the proportion of Pd₂Si formed during the nucleation stage compared to the amount transformed during the vertical growth. This is reflected in the model by the parameter L_0 , which indicates the initial height occupied by the Pd₂Si nuclei [Equation 5.9 in Subsection 5.4.4 *KJMAE kinetic model*]. We identify the nucleation region with the premixed zone at the interface that has reached the required stoichiometry to initiate nuclei formation. Figure 5.8(a) shows the evolution of the thickness of this nucleation zone as a function of the heating rate. While at the slowest rates of 0.1 - 1 K/s the nucleation process at the interface creates a 1.2 nm thick Pd₂Si layer, at fastest heating rate of 10⁵ K/s the thickness of the interfacial layer grows up to 4.8 nm, four times larger.

The interfacial formation mechanism of Pd₂Si at the lowest and highest heating rates is schematized in Figure 5.8(b). We interpret these differences as follows: at low heating rates (0.1 - 1 K/s) a thin mixed disordered region forms between Pd and a-Si at temperatures below 400 K. This region acts as the seed layer for the formation of the initial nuclei of Pd₂Si that occurs around 450 K (1st calorimetric peak). On increasing the temperature the Pd₂Si grows vertically by Pd and/or Si diffusion through the Pd₂Si interlayer. However, at ultrafast heating rates above thousands of K/s, the scheme changes dramatically. The activation energy for nucleation drives the nucleation peak towards higher temperatures (~ 650 K), enabling substantial intermixing before the interfacial layer has formed. As a consequence, the mixed disordered region is now four times thicker than the one obtained at slower heating rates. Since we assume nucleation only occurs within the premixed region, the heat dissipated during nucleation of Pd₂Si is also four times larger. Remarkably, in spite of the thickness increase of the nucleation-driven interfacial Pd₂Si layer, the vertical growth strictly follows an Arrhenius temperature dependence which

may indicate that the diffusion-controlled process occurs via fast diffusion paths, probably through grain boundaries connecting the Pd and Si reservoirs.

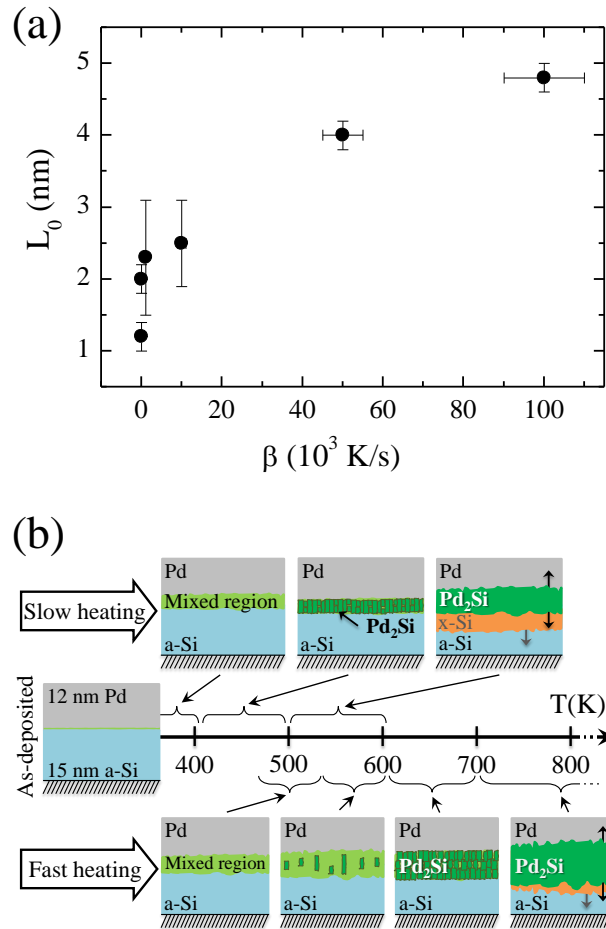


FIG. 5.8 Thickness of the initial Pd₂Si that forms at the a-Si/Pd interface as a function of the heating rate. (b) Schematics of the initial growth mode at the interface a-Si/Pd for slow (top) and fast (bottom) heating.

5.4.3 Calorimetric and structural analysis

The DSC measurements were carried out on Pd/a-Si layers grown onto Al foil previously covered by a vapor-deposited thin SiO₂ layer. Subsequently, the foil was folded and placed in the Al pan of the DSC. The mass of a-Si/Pd material was ~ 0.1 mg. Given the uncertainty of the mass we estimate the overall enthalpy of the DSC scans of Figure 5.6(a) to be 450 ± 100 J/g. The uncertainty in the enthalpy evaluation of the QAnC data of Figure 5.6(c) is much lower with a value of 480 ± 40 J/g (which corresponds to the total energy of the reaction, 93 μ J, by the total mass of the sample, 195 ng). In order to analyze in detail the exothermic jumps observed in Figure 5.6, to infer possible mechanisms of transformation, several tests were performed. In particular, the nature of the low temperature peak, which is formed by two events, is inferred by analyzing the influence of several mild heat treatments to the calorimetric

5. SILICIDE FORMATION OF Pd₂Si

signal. Figure 9(a) illustrates that the first peak is very sensitive to low temperature thermal treatments, since it disappears in a sample that was stored at room temperature (RT) for a period of one month. On the contrary, the second peak remains unchanged, except for a small shift due to slight variations in heating rate between the two samples. The small slope at the onset of the first peak [black line in Figure 9(b)] suggests that a diffusion-controlled mechanism rules the kinetics during the early growth stages. This is supported by the fact that the negative heat of mixing between Pd and Si favors the formation of an amorphous Pd_xSi_{1-x} alloy at the interface [57]. Figure 9(b) illustrates this behavior by comparing the calorimetric traces of a fresh Pd/a-Si couple (black curve) with a sample that has been previously annealed at 375 K for 15 min (grey curve). While the main peak remains unaltered, the remarkable change in both the onset and the slope of the reaction between both samples suggests that the intermixing between Pd and a-Si at the interface is completed during the low temperature annealing.

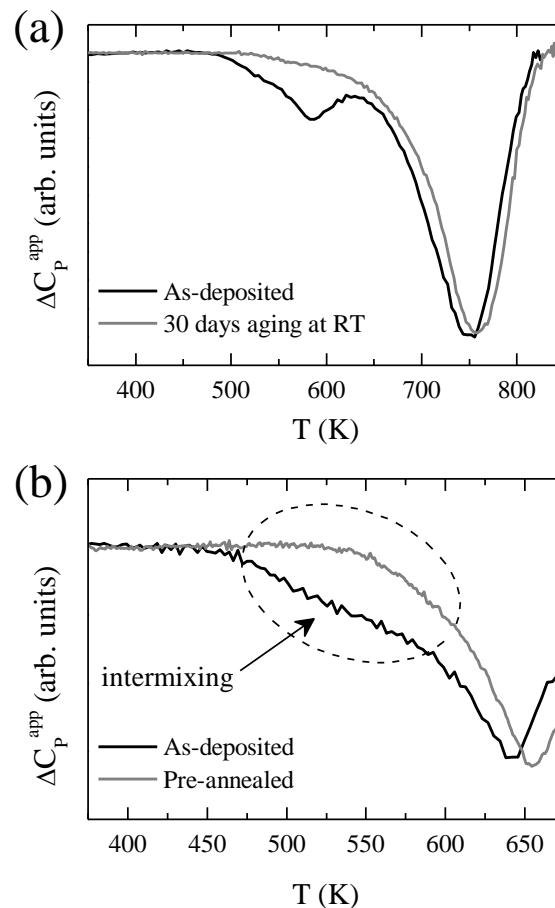


FIG. 5.9 Heat capacity versus temperature. (a) Aging effect during silicide formation. The black curve corresponds to a fresh Pd/a-Si bilayer measured in-situ in the deposition chamber immediately after growth, while the grey curve corresponds to a sample aged during 30 days at RT before the calorimetric up scan. Up scans carried out at $\sim 10^4$ K/s. (b) Diffusion/intermixing between a-Si and Pd at the interface. Comparison between a fresh Pd/a-Si bilayer (black line) and a sample that has been annealed at 375 K during 15 minutes prior to the calorimetric scan (grey line). Up scans performed at 5×10^4 K/s.

The nature of the first peak has been elucidated by both *ex-situ* XRD and *in-situ* synchrotron radiation measurements. In Figure 5.10(a) we plot the XRD spectra of two samples that have been thermally treated at 0.1 K/s up to 425 K (at the beginning of the first DSC peak, grey curve) and up to 650 K (after completion of the reaction, black curve). Although pure Pd is largely observed in samples treated at 425 K, reflections from the Pd₂Si hexagonal structure (PDF 00-019-0893), which becomes the unique phase present at 650 K, clearly appear, indicating that Pd₂Si starts to nucleate and grow during this low temperature peak. We note that the growth has a preferred orientation along the [00 ℓ] direction, which is consistent with the electron diffraction (ED) pattern and with previous works on metal/a-Si [2]. Figure 5.10(b) shows the intensity variations of the Pd (1 1 1) and Pd₂Si (0 0 16) X-ray diffraction peaks monitored *in-situ* during up scans at 1 K/s. The onset of the reaction at around 475 K is marked by the decrease of the Pd signal. As temperature increases the formation of the silicide becomes apparent from the increase of the Pd₂Si (0 0 16) diffraction intensity. This evolution is compatible with the calorimetric measurements of Figure 5.6. Note that the onset temperature threshold increases as heating rate increases. We have not observed any X-ray diffraction peak from crystalline Si. We assume Si crystallizes after nucleation of Pd₂Si and as soon as it is formed it is consumed by the vertical growth of Pd₂Si. The small amount persisting after complete formation of Pd₂Si due to excess Si in the initial stack was not detected by XRD.

The microstructural characterization by XTEM, of the ultrathin sample treated up to 1000 K, is shown in Figure 5.11. The film, after its fast thermal treatment by QAnC, is smooth and continuous with a final thickness around 20 nm [see Figure 5.11(a)]. The ED pattern (inset) corresponds to the hexagonal structure of the Pd₂Si phase. The magnified image in Figure 5.11(b) shows the same sample in bright field (left) and in dark field (right), confirming its polycrystalline nature and final thickness around 20 nm. Unfortunately, the thickness of the XTEM slices and the high density of the sample do not allow us to directly observe the Pd₂Si grain boundaries.

Based on those results, we assign the first exothermic peak to intermixing of Pd and a-Si to build up an amorphous/nanocrystalline layer at the interface, followed by nucleation of Pd₂Si along the a-Si/Pd interface. The second exothermic peak corresponds to the overlap of two processes: Si crystallization and vertical growth of Pd₂Si. The complete reaction path is schematized in Figure 5.12.

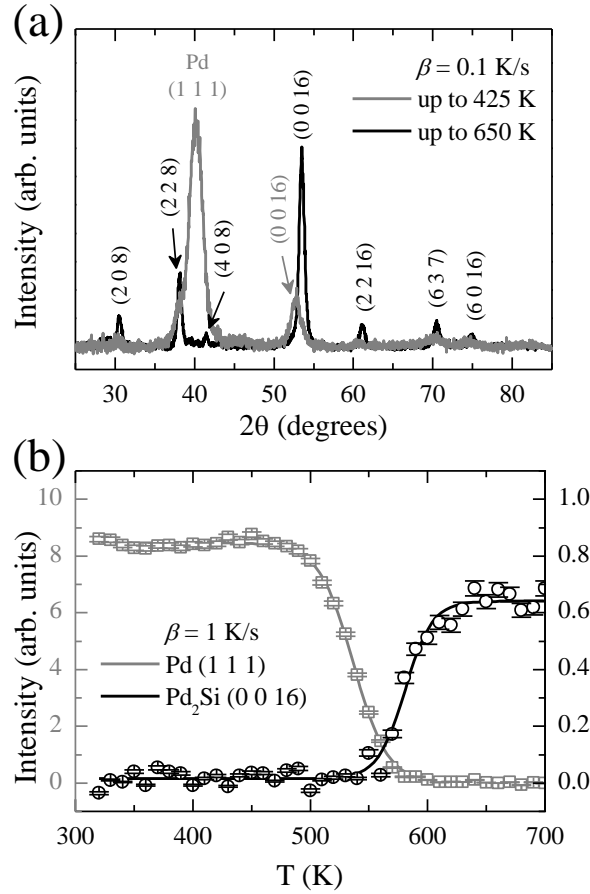


FIG. 5.10 (a) XRD patterns for two samples heated up to 425 K and 650 K at 0.1 K/s. All the diffraction lines correspond to Pd_2Si except the Pd (1 1 1) at $2\theta = 40^\circ$. (b) *In-situ* synchrotron X-ray data for the evolution of the Pd (1 1 1) and the Pd_2Si (0 0 16) lines during a thermal ramp at 1 K/s. The lines are a guide to the eye.

5.4.4 KJMAE kinetic model

In this case, for the Pd_2Si formation from a-Si, the KJMAE kinetic model [45,46,50] includes three processes: nucleation of Pd_2Si at the Pd/Si interface (process 2 in Figure 5.12, a-Si crystallization (process 3) and the vertical growth of the Pd_2Si with a diffusion limited growth (process 4 in Figure 5.12. We neglect for simplicity the initial mixing of the components (process 1 in Figure 5.12). Processes 3 and 4 are fully overlapped in temperature. The heat capacity as a function of temperature is obtained by

$$\Delta C_P(T) = \Delta H_{Pd_2Si} \frac{dx_{Pd_2Si}}{dT} + \Delta H_{x-Si} \frac{dx_{x-Si}}{dT} \quad (5.4)$$

where ΔH_{Pd_2Si} denotes the total enthalpy of formation of the silicide and ΔH_{x-Si} the one for the crystallization of a-Si transformed fractions. In order to calculate the transformed fraction of Pd_2Si , x_{Pd_2Si} , one has to consider the fraction transformed along the interface, x_L , and the growth in the

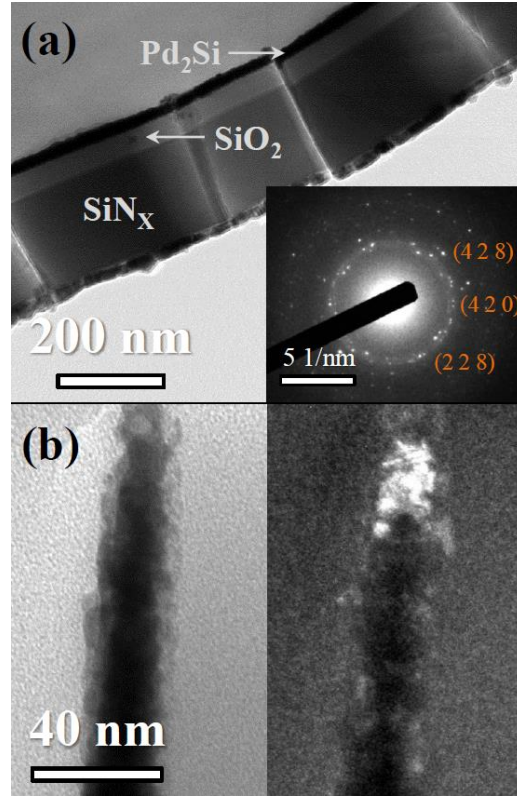


FIG. 5.11 XTEM images of the sample after measured at 5×10^4 K/s up to 1000 K: (a) Onto the membrane of the calorimetric chip enlarged by 100 kX. Inset: shows the corresponding ED pattern. (b) A Pd₂Si film at 250 kX in bright field (left) and in dark field (right).

vertical direction, L ,

$$x_{Pd_2Si}(T) = \frac{x_L(T)L(T)}{L_T} \quad (5.5)$$

where L_T is the final thickness of the Pd₂Si film, once all metallic Pd has reacted. The fraction of silicide phase that is formed at the a-Si/Pd interface at a certain temperature T can be written within the KJMAE formalism as Equation 5.1, with the extended transformed fraction expressed as

$$x_L^{ext}(t) = \pi \int_{T_0}^T \frac{I(T')}{\beta(T')} \left\{ r_0 + \int_{T'}^T \frac{U_L(\tau)}{\beta(\tau)} d\tau \right\}^2 dT' \quad (5.6)$$

where β is the heating rate, which can be temperature dependent, r_0 is the initial radius of the nuclei and $I(T)$ and $U_L(T)$ are respectively the nucleation rate and the lateral growth rate, both with an Arrhenius temperature dependence. We emphasize the first calorimetric jump, which mainly corresponds to the nucleation of the silicide at the a-Si/Pd interface, could only be reproduced by considering the growth rate to be negligible. In this case, the modeling provides the product $I r_0^2$, as can be deduced from Equation 5.5 when the growth rate goes to zero,

$$x_L^{ext}(t) = \pi \int_{T_0}^T \frac{I(T')}{\beta(T')} r_0^2 dT' \quad (5.7)$$

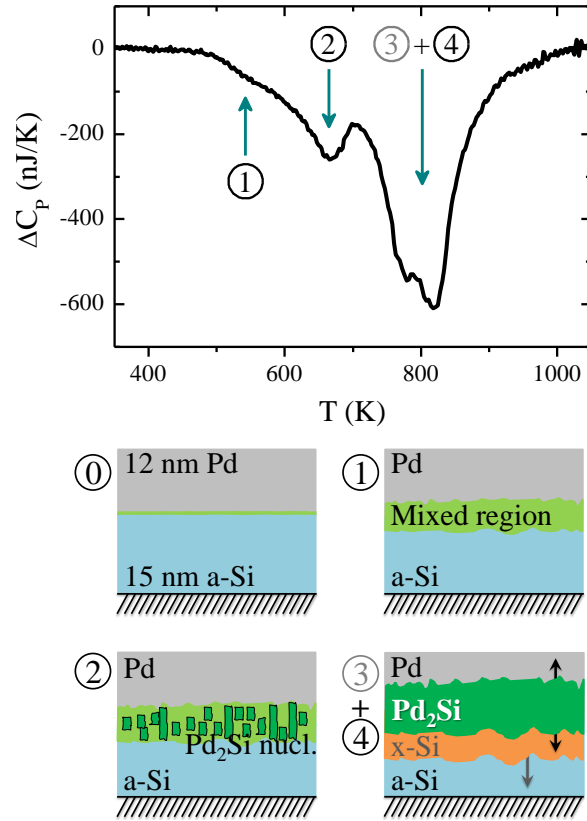


FIG. 5.12 (Top) Heat capacity versus temperature data for a Pd/a-Si bilayer measured at 10^5 K/s with the main events marked by an arrow: (1) diffusion/intermixing, (2) nucleation of Pd_2Si , and two overlapped processes: (3) crystallization of a-Si and (4) vertical growth of Pd_2Si . (Bottom) Schematics of reaction mechanisms giving rise to the exothermic features of the calorimetric data. The (0) scheme is the corresponding to the as-deposited state prior to any thermal treatment.

The vertical growth of the silicide follows a diffusion controlled mechanism that can be described by

$$\frac{dL}{dT} = \frac{D}{L\beta}(1 - x_V) \quad (5.8)$$

where D is an effective diffusion coefficient that accounts for the average diffusion rate both in the Pd and Si direction, which shows an Arrhenius dependence with temperature, and the factor $(1 - x_V)$, being $x_V = L/L_T$, accounts for the slowing down of the diffusion rate due to a reduction of the diffusing species. Integrating, L can be written as

$$L^2(T) = L_0^2 + \int_{T_0}^T \frac{2D(T')}{\beta(T')} [1 - x_V(T')] dT' \quad (5.9)$$

where L_0 is the initial height of the nuclei that forms at the interface, and it is equivalent to the intermixing region thickness.

We assume the crystallization of a-Si is catalyzed by the presence of Pd_2Si at the mixed region. Crystalline Si forms through a parallel front which transforms the a-Si. The growth rate of the crystallization

front, U_{x-Si} , has an Arrhenius temperature dependence,

$$U_{x-Si} = U_{0,x-Si} \exp\left(-\frac{E_U}{k_B T}\right) \quad (5.10)$$

The crystallized fraction of x-Si, x_{x-Si} , can be written as

$$x_{x-Si} = \frac{1}{D_{0,a-Si}} \int_{T_0}^T \frac{U_{x-Si}(T')}{\beta(T')} [1 - x_{x-Si}(T')] dT' \quad (5.11)$$

where the factor $(1 - x)$ was introduced to account for the slow termination of the crystallization peak. $D_{0,a-Si}$ corresponds to the remaining a-Si after the formation of the Pd₂Si layer at the interface (since L_0 depends on the heating rate, and determines the remaining a-Si, $D_{0,a-Si}$ is a heating rate dependent variable as well). Table 5.3 lists the main parameters involved in the fitting of the calorimetric traces.

TABLE 5.3 Parameters of the KJMAE kinetic model.

	Pd ₂ Si formation	a-Si crystallization
	$Ir_0^2 = I_0 r_0^2 \exp(-E_I/k_B T)$	
Nucleation	$I_0 r_0^2 = (7.5 \pm 3.4) \times 10^{13}$ nuclei/s	
	$E_I = (1.38 \pm 0.05)$ eV/at	
	$D = D_0 \exp(-E_D/k_B T)$	$U_{x-Si} = U_{0,x-Si} \exp(-E_U/k_B T)$
Vertical growth	$D_0 = (1.9 \pm 2.0) \times 10^3$ cm ² /s	$U_{0,x-Si} = (8.3 \pm 2.0) \times 10^8$ cm ² /s
	$E_D = (1.81 \pm 0.05)$ eV/at	$E_U = (1.72 \pm 0.05)$ eV/at
Final thickness	$L_T = (20.3 \pm 2.0)$ nm	$L_{x-Si} = 10.2$ to $13.8 (\pm 10\%)$ nm

Figure 5.13 reproduces calorimetric traces that illustrate the good matching between the model and the experimental data of Figure 5.6. It is important to note that during the STnC and QAnC measurements the heating rate is not strictly constant. In fact, the STnC is a simplification of the power compensated thin film calorimetry technique described elsewhere [41]. Due to the relatively large time constant of the calorimeter in high vacuum it was not possible to actively control the temperature ramp during silicide formation at heating rates above 10 K/s. Therefore a current-time profile has been used, instead. The observed lack of agreement in the onset of the vertical growth peak arises from a small uncoupling between the maximum of the heating rate and the extent of the reaction. This is due to the strong exothermic signal associated to silicide formation that locally enhances the temperature of the heater/sensor. This effect, together with the large heat losses associated to the low heating rates, is clearly observed for the saw-tooth curve fitting at 10³ K/s, and is more evident as the heating rate diminishes. For this reason the fittings for the STnC curves measured at 10 and 100 K/s are not presented, neither used for the kinetic parameters calculation.

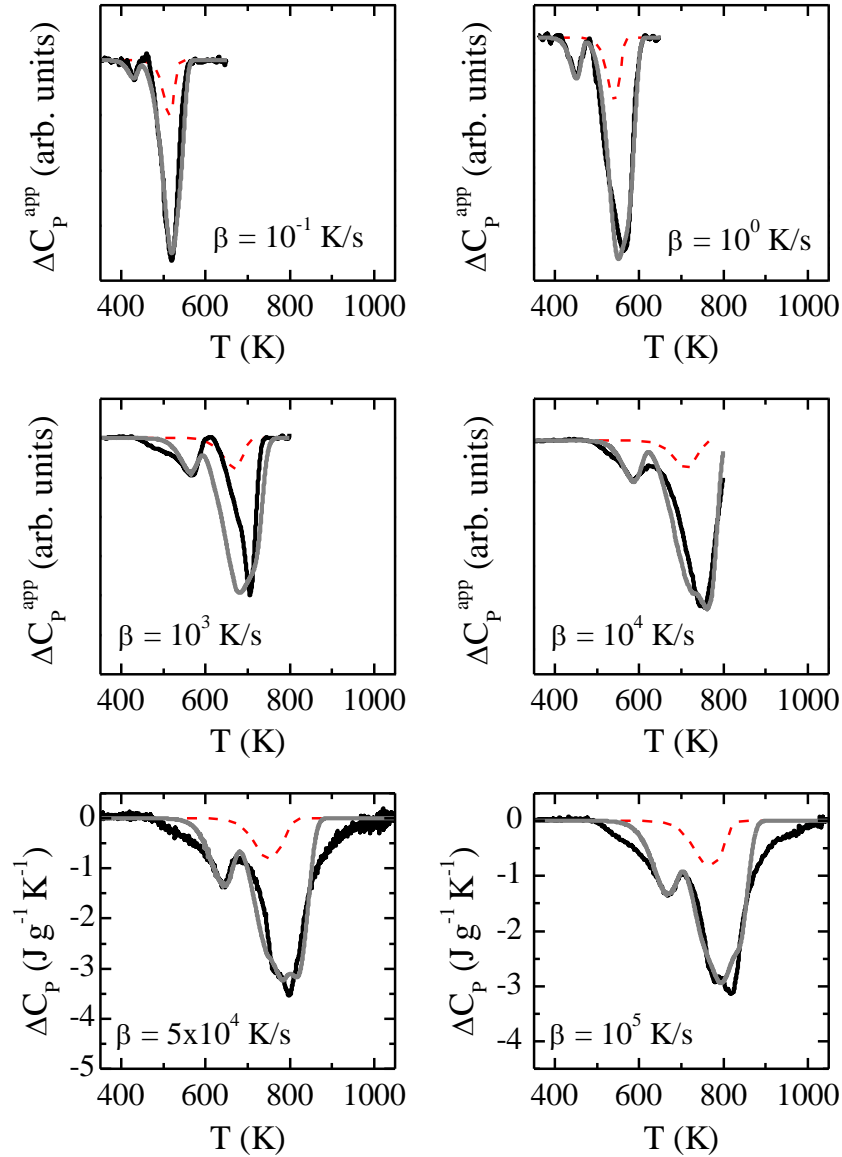


FIG. 5.13 Comparison between the ΔC_p obtained from experimental data (black lines) measured at 0.1 and 1 K/s (DSC), 10^3 and 10^4 K/s (STnC), 5×10^4 and 10^5 K/s (QAnC) and the values derived from Equation 5.4 of the kinetic model (grey lines). Red dashed lines report the calorimetric signal corresponding to the a-Si crystallization obtained from the kinetic model.

5.4.5 Simultaneous characterization by synchrotron radiation

In this Subsection we show the potentiality of carrying out simultaneous X-ray diffraction and calorimetric experiments to study phase formation during thin film reactions. This study has been done at the MSPD beamline of the ALBA Synchrotron in Barcelona. To increase the diffracting signal we use slightly thicker bilayers with identical overall stoichiometry as that used previously.

Three Pd (60 nm) / a-Si (75 nm) bilayer samples were measured by nanocalorimetry and X-ray diffrac-

tion at three different heating rates: 0.1, 1 and 10 K/s. In this case, the fastest heating rate is limited by the Mythen detector due to the low amount of mass available for X-ray scattering, and the lowest heating rate is determined by the sensitivity of the nanocalorimetric technique. The results are shown in Figure 5.14. The background of every plot is a 2D map of the X-ray signal as a function of temperature. These 2D maps represent a region about 12° of the total range covered by the Mythen detector. The colour marks the intensity of the signal. The superimposed symbols represent the apparent heat capacity extracted from nanocalorimetry at the three different heating rates. The nanocalorimetric curves are obtained by removing a 2nd scan (baseline) where no reaction takes place. The difference in apparent heat capacity provides information about the kinetics of the silicide formation overcoming the contribution of the addenda. The peak is related to the formation of Pd₂Si during the temperature up scan and it moves to higher temperatures as the heating rate increases, typical of thermally activated processes. The exothermic peaks are wider than those observed in commercial differential scanning calorimetry using samples with much higher mass amounts [58]. In fact, the broad signals of the various calorimetric traces shown in Figure 5.14 include several exothermic peaks that are partially overlapped in temperature. As previously demonstrated [58] the main processes involved in the silicide formation are: interdiffusion between Pd and a-Si to form a disordered Pd_xSi_{1-x} phase at the interface, nucleation of Pd₂Si in this mixed region, crystallization of amorphous silicon and vertical growth of Pd₂Si. In this case, due to the highly energetic reactions, self-heating is considerable and the control of the PI over the heating rate is not fast enough to individually differentiate the partially overlapped processes. Thus a single, broad, calorimetric peak is measured. The X-ray data of Figure 5.14 permits to follow several steps of the solid-state reaction. The loss of intensity of the Pd peak occurs at much lower temperatures than the onset of the apparent formation of Pd₂Si. Both events are marked as vertical dashed lines in Figure 5.14. First, the disappearance of the Pd at a temperature that depends on the heating rate (first vertical dashed line of Figure 5.14) highlight the partial consumption of Pd to form a non-crystalline Pd_xSi_{1-x} alloy at the interface, indistinguishable in the X-ray spectra. The onset temperatures of Pd consumptions are 440, 480 and 510 K for the 0.1, 1 and 10 K/s data, respectively. The disappearance of the Pd (1 1 1) peak occurs over a temperature interval of 80 - 100 K, and free Pd is completely consumed after the appearance of the Pd₂Si (0 0 16) diffraction peak. At temperatures of 540 K (0.1 K/s), 560 K (1 K/s) and 590 K (10 K/s) the Pd₂Si phase produces a coherent signal [Pd₂Si (0 0 16) reflection] that is clearly resolved in the XRD pattern.

The apparent delay between the calorimetric trace associated to silicide formation and the formation of Pd₂Si from the XRD spectra is mainly related to the minimum amount of material required to get a coherent signal from the Pd₂Si layer. In addition, as mentioned before the strong variation of the thermal resistance during silicide formation alters the thermal profile measured by the nanocalorimeter.

5. SILICIDE FORMATION OF Pd₂Si

These variations difficult the use of a suitable baseline to correct for heat losses and the addenda of the calorimetric cell, as clearly observed from the negative slope before the onset of the transformation at 420 - 425 K, in the trace recorded at 0.1 K/s, [Figure 5.14(a)].

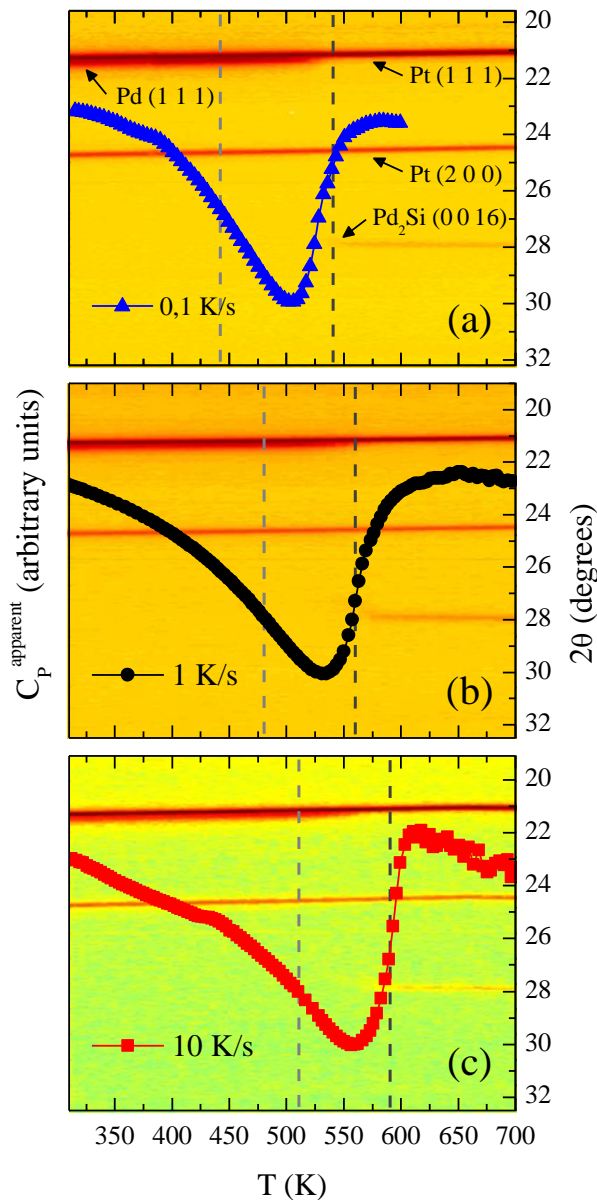


FIG. 5.14 Nanocalorimetric signal (symbols) for samples formed by 75 nm a-Si and 60 nm Pd bilayers at three different heating rates: (a) 0.1 K/s, (b) 1 K/s and (c) 10 K/s. The background of every graph corresponds to a 2D plot of the XRD patterns. Colour variations within each graph indicate the relative intensity of the XRD peaks. Dashed vertical lines mark the onset of Pd consumption (grey) and the appearance of the Pd₂Si diffraction peak (dark grey) obtained from the analysis of the XRD spectra.

Figure 5.15 show individual X-ray spectra obtained during the thermal treatments with acquisition times of 1 frame every 10 K for the samples measured at 1 and 10 K/s, and 1 frame every 2 K for the sample measured at 0.1 K/s. Before and after every experiment, more accurate XRD spectra with exposure times

to about 100 seconds were acquired. From these spectra it is deduced that Pd₂Si was the only crystalline phase formed during silicide formation. Figure 5.15(a) shows the as-deposited Pd/a-Si bilayer on the calorimetric chip as well as the product of the reaction after heating the sample to high temperature at 1 K/s. The Pd (1 1 1) reflection at 21.30° superposed to the Pt (1 1 1) diffraction peak at 21.15° is clearly resolved. After the thermal treatment, the Pd (1 1 1) peak disappears and a new peak at 28.15° assigned to the Pd₂Si (0 0 16) reflection appears. The {0 0 ℓ } family of planes is the only one that appears in the entire diffractogram, which indicates a strong texture in the [0 0 ℓ] direction. Figure 5.15(b) illustrates the evolution of the Pd₂Si (0 0 16) diffraction peak as a function of temperature during a temperature up scan at 1 K/s. Every spectrum is recorded with a temperature shift of 10 K. During heating up, the palladium diffraction signal remains unaltered up to 530 K, and then it starts to disappear gradually up to 590 K, when it disappears completely. After the palladium signature begins to fade, the Pd₂Si structure starts to diffract from 560 K to 640 K, when it is completely formed [Figure 5.15(b)]. The displacement of the peaks due to the thermal expansion of the unit cell has been corrected. This fact shows that during silicide formation, the Pd₂Si structure suffers a contraction as the temperature rises. The Pd₂Si unit cell undergoes a reduction along the c axis of 41.6 ± 5.4 pm between the {0 0 ℓ } planes during its formation, which supposes $\sim 1.5\%$ of the cell parameter length. Now, comparing the XRD patterns for the samples measured at three different heating rates, we observe a subtle difference on the resulting Pd₂Si reflection [Figure 5.15(c)]. By using the Scherrer equation [59] with the Pd₂Si (0 0 16) reflection, we estimate the mean coherent domains in a direction that is perpendicular to the substrate. As apparent from Figure 5.15(c) the ordered domains increase with the heating rate from 22 nm at 0.1 K/s to 30 nm at 10 K/s (Table 5.4). In all cases the average size is smaller than the Pd₂Si layer thickness, ~ 100 nm, which confirms the samples are polycrystalline with a strong texture along the [0 0 ℓ] direction. These parameters have been obtained by fitting the peaks with a Lorentzian function. These results as well as the temperature of the calorimetric peak minimum are summarized in Table 5.4.

TABLE 5.4 Parameters obtained from nanocalorimetric and XRD patterns: β is the heating rate, T^{cryst} is the temperature of crystallization, $FWHM$ is the full width at half maximum and θ_C is the centre of the Pd₂Si diffraction peak, both of them have been obtained by fitting a Lorentzian function. Finally, d^{mean} is the mean size of the ordered domains calculated by the Scherrer equation.

β (K/s)	T^{cryst} (K)	$FWHM$ (degrees)	θ_C (degrees)	d^{mean} (nm)
0.1	506 ± 10	0.20 ± 0.02	14.08 ± 0.01	22.3 ± 0.4
1	535 ± 11	0.16 ± 0.02	14.08 ± 0.01	28.2 ± 0.6
10	559 ± 11	0.15 ± 0.02	14.07 ± 0.01	30.2 ± 0.7

5. SILICIDE FORMATION OF Pd₂Si

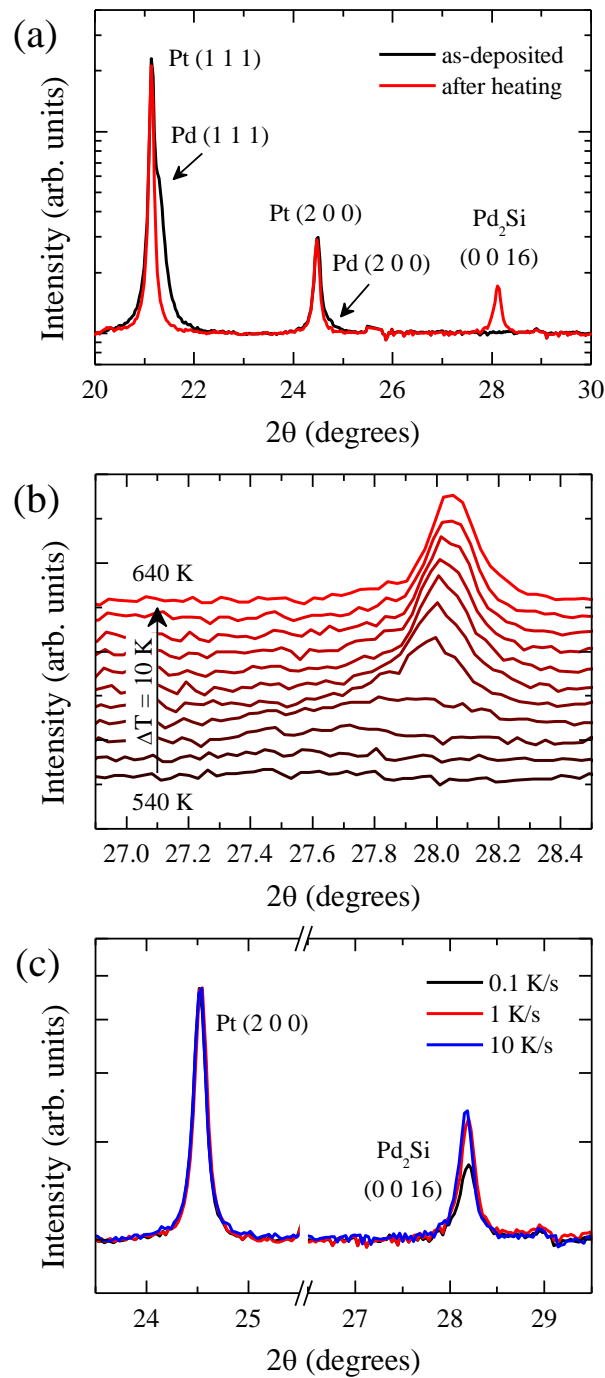


FIG. 5.15 (a) XRD patterns acquired during 100 seconds for the same sample: prior to the heat treatment (black line) and after it (red line). (b) XRD patterns acquired every 10 seconds for the sample measured at 1 K/s. The patterns obtained every 10 K from 540 K to 640 K are stacked vertically to show the evolution of the Pd₂Si structure formation with temperature. (c) XRD patterns acquired during 100 seconds for samples which have been thermally treated at three different heating rates: 0.1 K/s (black line), 1 K/s (red line) and 10 K/s (blue line).

5.5 Conclusions

We have studied the silicide formation between palladium and both single crystal and amorphous silicon. By modeling the calorimetric signal, we have determined the reaction kinetics.

The reaction between Pd and c-Si produces a single exothermic peak in the calorimetric trace, an indication that the nucleation and lateral growth and the vertical growth are substantially overlapped. The kinetics of the reaction is limited by the nucleation and lateral growth along the Pd/Si interface. The reaction enthalpy is consistent with values reported at slower heating rates for the formation of Pd₂Si, which is the only phase observed by XTEM and μ -XRD analysis of the samples.

In the case of the reaction between Pd and a-Si the picture is far more complex, since four processes can be identified: intermixing forming a disordered Pd_xSi_{1-x} region at the a-Si/Pd interface, nucleation of Pd₂Si in the premixed region, crystallization of a-Si, and simultaneously vertical growth of the Pd₂Si phase. More fundamentally, when analyzed over a wide heating rate interval of six orders of magnitude, from 0.1 to 10⁵ K/s, the formation of Pd₂Si, both with respect to the nucleation and the vertical growth, exhibits a pure Arrhenius behavior. The enhanced mass diffusion observed during the initial stages of the reaction increases with heating rate, due to the thermally activated nucleation of the Pd₂Si phase.

A combination of membrane-based nanocalorimetry and X-ray diffraction techniques has been developed to characterize phase transformation during silicide reaction. While nano-calorimetry provides information about the kinetics and thermodynamics of phase formation, X-ray diffraction shows the structural characteristics of the phases. Calorimetry indicates that silicide formation is kinetically activated with different processes overlapping to produce a single, broad, calorimetric peak. The X-ray diffraction data show how the structure is compressed along the basal plane, in the [00 ℓ] direction, when formed. No differences in the crystalline structure are observed for samples heated at 0.1, 1 and 10 K/s, except for a small variation on the mean size of the ordered domains, which increases with the heating rate. The Pd₂Si thin films are polycrystalline and textured along the [00 ℓ] direction.

References

- [1] W. D. Buckley and S. C. Moss. Structure and electrical characteristics of epitaxial palladium silicide contacts on single crystal silicon and diffused P-N diodes. *Solid-State Electronics*, 15(12):1331–1337, December 1972.

5. SILICIDE FORMATION OF Pd₂Si

- [2] R. W. Bower, D. Sigurd, and R. E. Scott. Formation kinetics and structure of Pd₂Si films on Si. *Solid-State Electronics*, 16(12):1461–1471, 1973.
- [3] G. Y. Robinson. Palladium silicide formation observed by Auger electron spectroscopy. *Applied Physics Letters*, 25(3):158, October 1974.
- [4] Hou-Yu Chen, Chia-Yi Lin, Min-Cheng Chen, Chien-Chao Huang, and Chao-Hsin Chien. Nickel Silicide Formation using Pulsed Laser Annealing for nMOSFET Performance Improvement. *Journal of The Electrochemical Society*, 158(8):H840, August 2011.
- [5] Hou-Yu Chen, Chia-Yi Lin, Chien-Chao Huang, and Chao-Hsin Chien. The effect of pulsed laser annealing on the nickel silicide formation. *Microelectronic Engineering*, 87(12):2540–2543, December 2010.
- [6] J. A. Kittl, M. A. Pawlak, C. Torregiani, A. Lauwers, C. Demeurisse, C. Vrancken, P. P. Absil, S. Biesemans, C. Detavernier, J. Jordan-Sweet, and C. Lavoie. Kinetics of Ni₃Si₂ formation in the Ni₂Si–NiSi thin film reaction from in situ measurements. *Applied Physics Letters*, 91(23):232102, 2007.
- [7] C. Van Bockstael, C. Detavernier, R. L. Van Meirhaeghe, J. L. Jordan-Sweet, and C. Lavoie. In situ study of the formation of silicide phases in amorphous Ni–Si mixed layers. *Journal of Applied Physics*, 106(6):064515, 2009.
- [8] M. T. Clavaguera-Mora, N. Clavaguera, D. Crespo, and T. Pradell. Crystallisation kinetics and microstructure development in metallic systems. *Progress in Materials Science*, 47(6):559–619, January 2002.
- [9] E. Ma, C. V. Thompson, and L. A. Clevenger. Nucleation and growth during reactions in multilayer Al/Ni films: The early stage of Al₃Ni formation. *Journal of Applied Physics*, 69(4):2211, February 1991.
- [10] M. Gonzalez-Silveira, M. Clavaguera-Mora, F. Pi, and J. Rodriguez-Viejo. Calorimetric evidence of asymmetry in the nucleation of CuMg₂ in Cu/Mg multilayers. *Physical Review B*, 69(11):113411, March 2004.
- [11] C. Michaelsen, K. Barmak, and T. P. Weihs. Investigating the thermodynamics and kinetics of thin film reactions by differential scanning calorimetry. *Journal of Physics D: Applied Physics*,

- 30(23):3167–3186, December 1997.
- [12] F. Spaepen and C. V. Thompson. Calorimetric Studies of Reactions in Thin films and Multilayers. *Applied Surface Science*, 38:1–12, 1989.
- [13] J. Orava, A. L. Greer, B. Gholipour, D. W. Hewak, and C. E. Smith. Characterization of supercooled liquid $\text{Ge}_2\text{Sb}_2\text{Te}_5$ and its crystallization by ultrafast-heating calorimetry. *Nature Materials*, 11(4):279–283, April 2012.
- [14] L. P. Cook, R. E. Cavicchi, N. Bassim, S. Eustis, W. Wong-Ng, I. Levin, U. R. Kattner, C. E. Campbell, C. B. Montgomery, W. F. Egelhoff, and M. D. Vaudin. Enhanced mass transport in ultrarapidly heated Ni/Si thin-film multilayers. *Journal of Applied Physics*, 106(10):104909, 2009.
- [15] D. W. Denlinger, E. N. Abarra, K. Allen, P. W. Rooney, M. T. Messer, S. K. Watson, and F. Hellman. Thin film microcalorimeter for heat capacity measurements. *Review of Scientific Instruments*, 65(4):946–959, 1994.
- [16] S. L. Lai, G. Ramanath, and L. H. Allen. High speed (10^4 °C/s) scanning microcalorimetry with monolayer sensitivity (J/m^2). *Applied Physics Letters*, 67(9):1229–1231, 1995.
- [17] S. A. Adamovsky, A. A. Minakov, and C. Schick. Scanning microcalorimetry at high cooling rate. *Thermochimica Acta*, 403(1):55–63, June 2003.
- [18] P. J. McCluskey and J. J. Vlassak. Combinatorial nanocalorimetry. *Journal of Materials Research*, 25(11):2086, 2010.
- [19] R. K. Kummamuru, L. De La Rama, L. Hu, M. D. Vaudin, M. Y. Efremov, M. L. Green, D. A. LaVan, and L. H. Allen. Measurement of heat capacity and enthalpy of formation of nickel silicide using nanocalorimetry. *Applied Physics Letters*, 95(18):181911, 2009.
- [20] S. Gaudet, P. Desjardins, and C. Lavoie. The thermally-induced reaction of thin Ni films with Si: Effect of the substrate orientation. *Journal of Applied Physics*, 110(11):113524, 2011.
- [21] J. Fouet, M. I. Richard, C. Mocuta, C. Guichet, and O. Thomas. In situ combined synchrotron X-ray diffraction and wafer curvature measurements during formation of thin palladium silicide film on Si (001) and Si (111). *Nuclear Instruments and Methods in Physics Research Section B: Beam Interactions with Materials and Atoms*, 284:74–77, August 2012.

5. SILICIDE FORMATION OF Pd₂Si

- [22] D. Smeets, J. Demeulemeester, D. Deduytsche, C. Detavernier, C. M. Comrie, C. C. Theron, C. Lavoie, and A. Vantomme. Simultaneous real-time X-ray diffraction spectroscopy, Rutherford backscattering spectrometry, and sheet resistance measurements to study thin film growth kinetics by Kissinger plots. *Journal of Applied Physics*, 104(10):103538, 2008.
- [23] Magali Putero, Benjamin Duployer, Ivan Blum, Toufik Ouled-Khachroum, Marie-Vanessa Coulet, Carine Perrin, Eric Ziegler, Christophe Muller, and Dominique Mangelinck. Combined in situ X-ray scattering and electrical measurements for characterizing phase transformations in nanometric functional films. *Thin Solid Films*, 541:21–27, August 2013.
- [24] K. Hoummada, A. Portavoce, C. Perrin-Pellegrino, D. Mangelinck, and C. Bergman. Differential scanning calorimetry measurements of kinetic factors involved in silicide process. *Applied Physics Letters*, 92(13):133109, 2008.
- [25] P. Gas, F. M. D'Heurle, F. K. LeGoues, and S. J. La Placa. Formation of intermediate phases, Ni₃Si₂ and Pt₆Si₅: Nucleation, identification, and resistivity. *Journal of Applied Physics*, 59(10):3458, May 1986.
- [26] D. Mangelinck, K. Hoummada, and I. Blum. Kinetics of a transient silicide during the reaction of Ni thin film with (1 0 0) Si. *Applied Physics Letters*, 95(18):181902, 2009.
- [27] D. Kim, A. Domenicucci, and S. S. Iyer. An investigation of electrical current induced phase transformations in the NiPtSi/polysilicon system. *Journal of Applied Physics*, 103(7):073708, 2008.
- [28] C. Rivero, P. Gergaud, M. Gailhanou, O. Thomas, B. Froment, H. Jaouen, and V. Carron. Combined synchrotron X-ray diffraction and wafer curvature measurements during Ni-Si reactive film formation. *Applied Physics Letters*, 87(4):041904, 2005.
- [29] M. Wittmer and K. N. Tu. Growth kinetics and diffusion mechanism in Pd₂Si. *Physical Review B*, 27(2):1173, 1983.
- [30] R. Suryana, O. Nakatsuka, and S. Zaima. Formation of Palladium Silicide Thin Layers on Si (1 1 0) Substrates. *Japanese Journal of Applied Physics*, 50(5):05EA09, May 2011.
- [31] Dusan Lexa. Hermetic sample enclosure for simultaneous differential scanning calorimetry/synchrotron powder X-ray diffraction. *Review of Scientific Instruments*, 70(5):2242, 1999.

- [32] F. Nemouchi, D. Mangelinck, C. Bergman, P. Gas, and Ulf Smith. Differential scanning calorimetry analysis of the linear parabolic growth of nanometric Ni silicide thin films on a Si substrate. *Applied Physics Letters*, 86(4):041903, 2005.
- [33] Augusto Marcelli, Plinio Innocenzi, Luca Malfatti, Mark a Newton, Julietta V Rau, Eglof Ritter, Ulrich Schade, and Wei Xu. IR and X-ray time-resolved simultaneous experiments: an opportunity to investigate the dynamics of complex systems and non-equilibrium phenomena using third-generation synchrotron radiation sources. *Journal of synchrotron radiation*, 19(Pt 6):892–904, November 2012.
- [34] Peter Zalden, Giuliana Aquilanti, Carmello Prestipino, Olivier Mathon, Bérangère André, Matthias Wuttig, and Marie Vanessa Coulet. Simultaneous calorimetric and quick-EXAFS measurements to study the crystallization process in phase-change materials. *Journal of synchrotron radiation*, 19(Pt 5):806–13, September 2012.
- [35] Kechao Xiao, John M. Gregoire, Patrick J. McCluskey, Darren Dale, and Joost J. Vlassak. Scanning AC nanocalorimetry combined with in-situ X-ray diffraction. *Journal of Applied Physics*, 113(24):243501, 2013.
- [36] Martin Rosenthal, David Doblaz, Jaime J Hernandez, Yaroslav I Odarchenko, Manfred Burghammer, Emanuela Di Cola, Denis Spitzer, a E Antipov, L S Aldoshin, and Dimitri a Ivanov. High-resolution thermal imaging with a combination of nano-focus X-ray diffraction and ultra-fast chip calorimetry. *Journal of synchrotron radiation*, 21(Pt 1):223–8, January 2014.
- [37] M. Zhang, M. Yu. Efremov, E. a. Olson, Z. S. Zhang, and L. H. Allen. Real-time heat capacity measurement during thin-film deposition by scanning nanocalorimetry. *Applied Physics Letters*, 81(20):3801, 2002.
- [38] M. Molina-Ruiz, A. F. Lopeandia, F. Pi, D. Givord, O. Bourgeois, and J. Rodriguez-Viejo. Evidence of finite-size effect on the Néel temperature in ultrathin layers of CoO nanograins. *Physical Review B*, 83(14):140407, April 2011.
- [39] A. F. Lopeandia, J. Rodriguez-Viejo, M. Chacon, M. T. Clavaguera-Mora, and F. J. Muñoz. Heat transfer in symmetric U-shaped microreactors for thin film calorimetry. *Journal of Micromechanics and Microengineering*, 16(5):965–971, May 2006.
- [40] M. Y. Efremov, E. A. Olson, M. Zhang, S. L. Lai, F. Schiettekatte, Z. S. Zhang, and L. H. Allen.

5. SILICIDE FORMATION OF Pd₂Si

- Thin-film differential scanning nanocalorimetry: heat capacity analysis. *Thermochimica Acta*, 412:13–23, 2004.
- [41] A. F. Lopeandia, F. Pi, and J. Rodriguez-Viejo. Nanocalorimetric analysis of the ferromagnetic transition in ultrathin films of nickel. *Applied Physics Letters*, 92(12):122503, 2008.
- [42] Y. Anahory, M. Guihard, D. Smeets, R. Karmouch, F. Schiettekatte, P. Vasseur, P. Desjardins, L. Hu, L. H. Allen, and E. Leon-Gutierrez. Fabrication, characterization and modeling of single-crystal thin film calorimeter sensors. *Thermochimica Acta*, 510(1-2):126–136, 2010.
- [43] F. R. Boer, R. Boom, W. C. M. Mattens, A. R. Miedema, and A. K. Niessen. *Cohesion in metals: transition metal alloys*. North-Holland, 1988.
- [44] S. V. Meschel and O. J. Kleppa. Standard enthalpies of formation of some 4d transition metal silicides by high temperature direct synthesis calorimetry. *Journal of Alloys and Compounds*, 274(1):193–200, 1998.
- [45] K. R. Coffey, L. A. Clevenger, K. Barmak, D. A. Rudman, and C. V. Thompson. Experimental evidence for nucleation during thin-film reactions. *Applied Physics Letters*, 55(9):852, August 1989.
- [46] M. Gonzalez-Silveira, J. Rodriguez-Viejo, G. Garcia, F. Pi, F. J. Ager, J. L. Labar, A. Barna, M. Menyhard, and L. Kotis. Influence of layer microstructure on the double nucleation process in Cu/Mg multilayers. *Journal of Applied Physics*, 100(11):113522, 2006.
- [47] T. Hosoi, K. Sano, K. Hosawa, and K. Shibahara. Formation Kinetics and Work Function Tuning of Pd₂Si Fully Silicided Metal Gate. *Japanese Journal of Applied Physics*, 46(4B):1929–1933, April 2007.
- [48] C. Detavernier, R. L. Van Meirhaeghe, F. Cardon, R. A. Donaton, and K. Maex. CoSi₂ formation in the presence of interfacial silicon oxide. *Applied Physics Letters*, 74(20):2930, 1999.
- [49] R. T. Tung. Oxide mediated epitaxy of CoSi₂ on silicon. *Applied Physics Letters*, 68(24):3461, June 1996.
- [50] M. Molina-Ruiz, A. F. Lopeandia, M. Gonzalez-Silveira, Y. Anahory, M. Guihard, G. Garcia, M. T. Clavaguera-Mora, F. Schiettekatte, and J. Rodriguez-Viejo. Formation of Pd₂Si on single-

- crystalline Si (100) at ultrafast heating rates: An *in-situ* analysis by nanocalorimetry. *Applied Physics Letters*, 102(14):143111, 2013.
- [51] J. C. C. Fan and C. H. Anderson Jr. Transition temperatures and heats of crystallization of amorphous Ge, Si, and $\text{Ge}_{1-x}\text{Si}_x$ alloys determined by scanning calorimetry. *Journal of Applied Physics*, 52(6):4003, 1981.
- [52] D. He, J. Y. Wang, and E. J. Mittemeijer. The initial stage of the reaction between amorphous silicon and crystalline aluminum. *Journal of Applied Physics*, 97(9):093524, 2005.
- [53] Z. Wang, J. Wang, L. Jeurgens, and E. Mittemeijer. Tailoring the Ultrathin Al-Induced Crystallization Temperature of Amorphous Si by Application of Interface Thermodynamics. *Physical Review Letters*, 100(12):125503, March 2008.
- [54] H. E. Kissinger. Reaction Kinetics in Differential Thermal Analysis. *Analytical Chemistry*, 29(11):1702, 1957.
- [55] K. Homma, T. Koike, S. Ando, K. Adachi, and M. Motohashi. Interfacial Reaction and Silicide Formation in Pd/a-Si:H Layered Films. *Electronics and Communications in Japan, Part 2*, 80(3):12–22, 1997.
- [56] E. C. Zingu, J. W. Mayer, C. Comrie, and R. Pretorius. Mobility of Pd and Si in Pd_2Si . *Physical Review B*, 30(10):5916–5922, 1984.
- [57] L. J. Chen. Solid state amorphization in metal/Si systems. *Materials Science and Engineering*, R29(June):115–152, 2000.
- [58] Manel Molina-Ruiz, Aitor F. Lopeandía, Marta Gonzalez-Silveira, Gemma Garcia, Inma Peral, Maria T. Clavaguera-Mora, and Javier Rodríguez-Viejo. Kinetics of silicide formation over a wide range of heating rates spanning six orders of magnitude. *Applied Physics Letters*, 105(1):013113, July 2014.
- [59] Paul Scherrer. Bestimmung der Grösse und der Inneren Struktur von Kolloidteilchen Mittels Röntgenstrahlen. *Mathematisch-Physikalische Klasse*, 2:98–100, 1918.

6. General conclusions

The objectives of this work were to improve energy resolution achieved with already existing quasi-adiabatic nanocalorimetry (QAnC), as well as expanding the dynamic range of heating rates combining both QAnC and power compensated nanocalorimetry (PCnC). Furthermore, the successful development of microsecond-pulsed heating nanocalorimetry (μ -PHnC) is one of the main achievements of this Thesis. It opens the way to measure heat capacity in quasi-isothermal conditions, offering high resolution, down to $75 \text{ pJ K}^{-1} \text{ mm}^{-2} \text{ Hz}^{-1/2}$, characteristics of QAnC, combined with small thermal gradients. Proof of concept of this technique is performed measuring the CoO second-order phase transition. Better thermal gradients compared with QAnC are obtained. The elimination of thermal gradients leads to a narrowing around 15 K on the transition peak. The study of components involved on the heat capacity data treatment, give rise to an alternative derivation improving signal-to-noise ratio and accuracy of heat capacity data.

The optimized QAnC is used to study the antiferromagnetic transition in ultrathin films of CoO. The improved technique sensitivity, below $1 \text{ nJ K}^{-1} \text{ mm}^{-2}$, allows the study of samples as thin as 1.5 nm. The observed scaling of the Néel temperature with the nanograin diameter is characteristic of phase transition in finite 3D systems. We state that the microstructure, rather than the film thickness, controls the magnetic properties in such antiferromagnetic oxides. Magnetic interaction in antiferromagnetic oxides is clearly influenced by grain size and grain boundaries density. Magnetic signature is found to deeply rely on oxygen stoichiometry inside the CoO sample.

The formation kinetics in Pd₂Si system is analyzed by summing up differential scanning calorimetry (DSC) for measurements from 0.1 and 1 K/s, saw-tooth nanocalorimetry (STnC) from 10 to 10⁴ K/s, and QAnC for 10⁵ K/s. The reaction between Pd and c-Si produces a single exothermic peak in the calorimetric trace, an indication that the nucleation and lateral growth and the vertical growth are substantially overlapped. The kinetics of the reaction is limited by the nucleation and lateral growth along the Pd/Si interface. The reaction between Pd and a-Si is far more complex, since four processes were identified:

intermixing forming a disordered $\text{Pd}_x\text{Si}_{1-x}$ region at the a-Si/Pd interface, nucleation of Pd_2Si in the premixed region, crystallization of a-Si, and simultaneously vertical growth of the Pd_2Si phase. During the simultaneous XRD study, the diffraction data show how the structure is compressed along the basal plane, in the $[00\ell]$ direction, when formed. No differences in the crystalline structure are observed for samples heated at 0.1, 1 and 10 K/s, and measured by PCnC, except for a small variation on the mean size of the ordered domains, which increases with the heating rate.

List of publications

Mainly related to this Thesis:

- M. Molina-Ruiz, A. F. Lopeandia, F. Pi, D. Givord, O. Bourgeois, and J. Rodriguez-Viejo. Evidence of finite-size effect on the Néel temperature in ultrathin layers of CoO nanograins. *Physical Review B*, 83:140407(R), 2011.
- M. Molina-Ruiz, A. F. Lopeandia, M. Gonzalez-Silveira, Y. Anahory, M. Guihard, G. Garcia, M. T. Clavaguera-Mora, F. Schiettekatte, and J. Rodriguez-Viejo. Formation of Pd₂Si on single-crystalline Si (100) at ultrafast heating rates: and in-situ analysis by nanocalorimetry. *Applied Physics Letters*, 102:143111, 2013.
- M. Molina-Ruiz, A. F. Lopeandia, M. Gonzalez-Silveira, G. Garcia, I. Peral, M. T. Clavaguera-Mora, and J. Rodriguez-Viejo. Kinetics of silicide formation over a wide range of heating rates spanning six orders of magnitude. *Applied Physics Letters*, 105:013113, 2014.
- M. Molina-Ruiz, P. Ferrando-Villalba, C. Rodríguez-Tinoco, G. Garcia, I. Peral, J. Rodriguez-Viejo, and A. F. Lopeandia. Simultaneous nanocalorimetry and fast XRD measurements to study the silicide formation in Pd/a-Si bilayers. *Journal of Synchrotron Radiation*, submitted.

Other publications:

- D. Petti, E. Albisetti, H. Reichlova, J. Gazquez, M. Varela, M. Molina-Ruiz, A. F. Lopeandia, K. Olejnik, V. Novak, I. Fina, B. Dkhil, J. Hayakawa, X. Marti, J. Wunderlich, T. Jungwirth, and R. Bertacco. Storing magnetic information in IrMn/MgO/Ta tunnel junctions via field-cooling. *Applied Physics Letters*, 102:192404, 2013.

- P. Ferrando-Villalba, A. F. Lopeandia, Ll. Abad, J. Llobet, M. Molina-Ruiz, G. Garcia, M. Gerbolès, F. X. Alvarez, A. R. Goñi, F. J. Muñoz-Pascual, and J. Rodriguez-Viejo. *Nanotechnology*, 25:185402, 2014.
- S. Poran, M. Molina-Ruiz, A. Gerardin, A. Frydman, and O. Bourgeois. Specific heat measurement set-up for quench condensed thin superconducting films. *Review of Scientific Instruments*, 85:053903, 2014.

Under preparation:

- M. Molina-Ruiz, C. Rodriguez-Tinoco, I. Moder, J. Rodriguez-Viejo, and A. F. Lopeandia. Practical considerations in nanocalorimetry heat capacity derivation. *International Journal of Thermal Sciences*.
- A. F. Lopeandia, M. Molina-Ruiz, O. Bourgeois, Ll. Abad. Microsecond-pulsed heating nanocalorimetry: quasi-static method. *Nanoscale*.
- M. Molina-Ruiz, G. Garcia, J. Santiso, J. Labar, J. Rodriguez-Viejo, and A. F. Lopeandia. Effect of thermal treatments on the magnetic interaction of polycrystalline CoO. *Physical Review B*.

Glossary

* *Kinetic parameters are shown intentionally in italics.*

ADC, analogic-digital conversor

AFM, antiferromagnetic / antiferromagnetism

a-Si, amorphous silicon

BSE, backscattered electrons

β , heating rate

CC, calorimetric cell

CMRR, common-mode rejection ratio

CNM, National Center of Microelectronics (for its acronym in Spanish)

CoO, cobalt (II) oxide

Co₃O₄, cobalt (II,III) oxide

ΔH_f , enthalpy of formation

DAQ, data acquisition card

DBC, direct bonded copper

DM, digital multimeter

DSC, differential scanning calorimetry

D , effective diffusion coefficient

$D_{0,a-Si}$, remaining a-Si after Pd₂Si formation

EB-PVD, electron-beam physical vapor deposition

ED, electron diffraction

E_A , activation energy

E_I , Pd₂Si nucleation activation energy

E_D , Pd₂Si vertical growth activation energy

E_U , a-Si crystallization activation energy

FM, ferromagnetic / ferromagnetism
FPGA, field-programmable gate array
GeRT, germanium resistance thermometer
GPIB, general purpose interface bus
HCl, hydrochloric acid
HF, hydrofluoric acid
H₂O₂, hydrogen peroxide
LCP, thin films laboratory (for its acronym in Catalan)
I, nucleation rate
IMB, Institute of Microelectronics of Barcelona
IMS, insulated metal substrate
IPID, integral-proportional-integral-derivative
KOH, potassium hydroxide
LAC, Controlled Ambient Laboratory (for its acronym in Catalan)
L_T, Pd₂Si final film thickness
L₀, initial nuclei formed at the Pd₂Si interface
μ-PHnC, microsecond-pulsed heating nanocalorimetry
μ-XRD, micro-X-ray diffraction
PI, proportional-integral
PID, proportional-integral-derivative
Pd, palladium
PDF, powder diffraction file
PM, paramagnetic / paramagnetism
PTFE, polytetrafluoroethylene or Teflon
QAnC, quasi-adiabatic nanocalorimetry
r₀, initial nuclei radius
RT, room temperature
STnC, saw-tooth nanocalorimetry
SEM, scanning electron microscopy
Si, silicon
Si₃N₄, stoichiometric low-stress silicon nitride
SiO₂, silicon (II) oxide
SMU, source/measure unit
SNR, signal-to-noise ratio

7. GLOSSARY

SQUID, superconducting quantum interference device

TCR, temperature coefficient of resistance

TEM, transmission electron microscopy

T_N , Néel temperature

T_D , Debye temperature

UAB, Autonomous University of Barcelona (for its acronym in Catalan)

U_L , lateral growth rate

U_{x-Si} , x-Si growth rate front

x_L , fraction of formed phase

x_L^{ext} , extended fraction of formed phase

x_{x-Si} , fraction of formed x-Si

XRD, X-ray diffraction

XTEM, cross sectional transmission electron microscopy

x-Si, crystallized silicon

